

INFLAMED LEUKOCYTE-MIMETIC NANOPARTICLE AND ITS
APPLICATIONS IN QUANTITATIVE INFLAMMATION IMAGING

A Dissertation

Presented to the Faculty of the Graduate School

of Cornell University

In Partial Fulfillment of the Requirements for the Degree of

Doctor of Philosophy

by

Xiaoyue Chen

August 2012

© 2012 Xiaoyue Chen

INFLAMED LEUKOCYTE-MIMETIC NANOPARTICLE AND ITS APPLICATIONS IN QUANTITATIVE INFLAMMATION IMAGING

Xiaoyue Chen, Ph. D.

Cornell University 2012

Intense and prolonged inflammation correlates with the progression of various inflammatory diseases, ranging from cancer to sepsis. Sensitive detection and quantitative examination of the site of inflammation will, therefore, produce a wide-ranging impact on disease diagnosis and treatment. Studies presented in this dissertation first attempt to design one nanoparticle that mimics the molecular interactions occurring between inflamed leukocytes and endothelium. To incorporate inflammation-sensitive molecular interactions, super paramagnetic iron oxide (SPIO) nanoparticles were conjugated with integrin lymphocyte function-associated antigen (LFA)-1 I domain, engineered to mimic activated leukocytes in physiology. We speculated such nanoparticles may possess selectivity toward diverse host inflammatory responses, which were then confirmed by whole body optical and magnetic resonance imaging (MRI) *in vivo*, in that leukocyte-mimetic nanoparticles (LMN) localized preferentially to the inflamed vasculature marked by high level of ICAM-1 within and in the invasive front of the tumor, as well as to the subcutaneous site of acute inflammation.

The second part of the studies closely follow up with this finding, focusing on high resolution spatiotemporal imaging of inflammation in mice treated with systemic

injection of lipopolysaccharides (LPS) to mimic systemic inflammatory response or sepsis. Diagnosis of organ-level inflammation was achieved by MR imaging of LMN. Using a novel MRI quantitative susceptibility mapping (QSM) technique for non-invasive quantification of SPIO, we observed a greater accumulation of LMN in the liver, specific to ICAM-1 induction due to LPS-induced inflammation. Overall, the amounts of organic nanoparticles estimated by QSM were in good agreement with the values measured by radioactivity, presenting the idea that spatiotemporal mapping of LMN by QSM may provide a reliable, rapid, non-invasive method for identifying organ-specific inflammation not offered by existing diagnostic techniques.

Yeast surface display (YSD) has been a powerful tool in engineering the active I domain for LMN. The last part of this dissertation discusses utilizing YSD in generating new monoclonal antibody against ephrin-B2, one highly conserved antigen participating in tumor angiogenesis. Being independent investigations outside of our major focus on LMN and inflammation imaging, studies presented here demonstrate another example of molecular discoveries which are critical for future development of biomimetic nanomaterials and therapeutics.

BIOGRAPHICAL SKETCH

Xiaoyue Chen was born in Hangzhou, Zhejiang in China. As the only daughter of a mechanical engineer, she has developed an enthusiasm about science and technology since childhood. Xiaoyue received her B.S. at Peking University, from College of Life Sciences. She majored in Biological Sciences as an undergraduate, where she met her great friends and mentors who strongly influenced her to pursue a Ph.D. in biomedical engineering.

Advised by Professor Moonsoo Jin during her PhD studies, Xiaoyue had the opportunities to participate in a variety of research collaborations with other research labs, companies and medical schools. These interactions brought her useful materials and abundant inspiration for research. Her research was honored by a Graduate Research Award from the Biomedical Engineering Society in 2011 during the annual meeting. She also has published a number of papers, one first author, one equal contribution, five coauthor and two more in submission for publication. Xiaoyue is passionate about an entrepreneurial career in science and healthcare, where she aims to bring more discovery and better products to people.

To my father in heaven, and all the beloved

ACKNOWLEDGMENTS

First of all, I would like to thank Richard Feynman, my forever science icon, for your appraisal of Cornell in “Surely You're Joking, Mr. Feynman!”, I was driven to the same place once you worked, and for your prognosis in “There's Plenty of Room at the Bottom”, I have developed a love and vision for my current research.

I owe many thanks to my advisor, Professor Moonsoo Jin, for his support and guidance throughout my stay in Cornell for five years. The successful completion of this work and many others of my honor would not be possible without innumerable discussions with him. His wisdom in knowledge and his devotion to research have been my best incitation to conquer numerous failures. I am highly indebted to him for helping me grow academically during my career development.

I would also like to acknowledge Professor Warren Zipfel and John Parker for their role on my Special Committee. I am neither a great speaker nor a gifted student in their fields of specialty, however, their patience with my research talk and continuous input into my study have greatly helped my understanding from other aspects of my thesis topic.

Many thanks to my colleagues in the Jin research group, students and staff from Chris Schaffer lab, Claudia Fischbach lab, Yi Wang lab, Alexander Nikitin lab, Raza Zarnegar lab, Xiling Shen lab, David Putnam lab, Susan Daniel lab, Carl Batt lab, John Lis lab and Cornell core facilities, for all your support of my studies in my difficult times. I want to acknowledge the following people specially (in name order):

Ada Zhang: performing qPCR experiments (aka: repetitive work).

Alexander Nikitin: teaching me mice pathology, providing perfusion apparatus.

Andrea Flesken-Nikitin: helping me acquire the first set of dissection tools in my life.

Belinda Floyd: being an attentive Graduate Field Assistant.

Carl Batt: sharing his research on SPIO.

Carol Bayles: training me on the Confocal and Metamorph systems.

Chris Schaffer: providing surgery room, cryotome, helping me prepare AHA proposal.

Claudia Fischbach: providing centrifuge, tissue cassettes, liquid nitrogen and more.

David Kleiman: helping with MRI on live mice.

David Putnam: providing plate reader and nitrogen gas.

Dickson Kirui: providing me the very early inspiration of LMN.

Hsien-wei Meng: following up with SELEX project.

Hua Shi: teaching me filter-binding SELEX.

Jeerapond Leelawattanachai: helping out with my early animal experiments.

John Lis: providing me the portal to aptamer research.

Marina Ramirez: being a great lab manager.

Martin Prince: being my first teacher of MRI.

Michael Shuler: making Cornell BME possible.

Nikolai Rakhilin: producing Id.

Nozomi Nishimura: teaching me everything about mice handling not learned in class.

Pengcheng Bu: teaching me tips about western blot & immunofluorescence.

Peter Doerschuk: being an attentive Director of Graduate Studies.

Raza Zarnegar: enabling my animal experiments in Weill Medical School.

Rebecca Williams: technical advice on whole body fluorescence imaging.

Richard Wong: being a very helpful partner, teaching me QSM.

Rosin Owens: setting good examples of record keeping.

Spencer Park: teaching me SPR.

Sungkwon Kang: being a model student, providing Id constructs, & discussing science.

Susan Daniel: providing DLS.

Sylvia Allen: attending and taking good care of my research animals.

Taehyun Park: being a happy post-doc in the most difficult stage of research.

Thom Santisakultarm: teaching me retroorbital injection, sparing me practice animals.

Tian Liu: pilot scanning of MRI phantom.

Xiaoling Gu: teaching me protein refolding and immunohistology.

Xuebo Hu: teaching me many things about yeast surface display.

Yogindra Vedvyas: organizing Jin lab.

Yi Wang: teaching me a lot about MRI.

Lastly, I want to thank my funding sources, American Heart Association Scientist Development Grant and NIH R01 (GM090320), as well as the Cornell campus-to-campus bus system for supporting my research.

TABLE OF CONTENTS

BIOGRAPHICAL SKETCH.....	iii
DEDICATION	iv
ACKNOWLEDGMENTS	v
TABLE OF CONTENTS	viii
LIST OF FIGURES	xiii
LIST OF TABLES	xxii
LIST OF ABBREVIATIONS	xxiii
LIST OF SYMBOL.....	xxviii
CHAPTER 1 INTRODUCTION.....	1
1.1 Nanoparticle-based biologic mimetics.....	2
1.2 <i>In vivo</i> distribution of nanoparticles – size, composition and beyond.....	2
1.3 Biomimetics of leukocytes.....	4
1.4 Current applications of leukocyte mimetics in biomedical imaging	5
1.5 Engineering active LFA-1 integrin – a physiological ligand during leukocyte adhesion	6
1.6 Engineering iron oxide nanomicelles for facile coating of proteins – a platform for creating biomimetic nanoparticles in biomedical applications	8
1.7 Iron-sensing assays	10
1.7.1 Perls’ Prussian blue.....	10
1.7.2 Ferrozine assay.....	11
1.7.3 Atomic absorption spectroscopy	11
1.7.4 Quantitative susceptibility mapping (QSM)	11
1.8 Engineering molecules of interest using yeast surface display.....	12
1.9 Organization of the dissertation	13
REFERENCES	16
CHAPTER 2 INFLAMED LEUKOCYTE-MIMETIC NANOPARTICLES FOR MOLECULAR IMAGING OF INFLAMMATION	24
2.1 Abstract.....	24

2.2 Introduction.....	25
2.3 Materials and methods	26
2.3.1 Preparation and characterization of protein coated SPIO nanomicelles	26
2.3.2 Cell culture.....	27
2.3.3 Immunofluorescence flow cytometry	28
2.3.4 Microscopy visualization of cell labeling <i>in vitro</i>	28
2.3.5 Magnetic cell labeling and quantification.....	29
2.3.6 Subcutaneous tumor model.....	30
2.3.7 Acute LPS-inflammation model	30
2.3.8 Near-IR optical imaging of mice	30
2.3.9 MR imaging of mice with acute inflammation	30
2.3.10 Histology.....	31
2.3.11 Statistical analysis	32
2.4 Results.....	32
2.4.1 Synthesis and characterization of leukocyte-mimetic nanoparticles	32
2.4.2 Quantitative measurement of selective binding of LMN by MRI	37
2.4.3 <i>Ex vivo</i> detection of ICAM-1 induction in human tumor xenograft and in inflamed stroma.....	40
2.4.4 <i>In vivo</i> detection of ICAM-1 induction in human tumor xenograft and in inflamed stroma.....	42
2.4.5 <i>In vivo</i> detection of temporal dynamics of inflammation by optical imaging and MRI	48
2.5 Discussion.....	50
2.6 Conclusion	56
REFERENCES	58

CHAPTER 3 VISUALIZING AND QUANTIFYING ACUTE INFLAMMATION USING ICAM-1 SPECIFIC NANOPARTICLES AND MRI QUANTITATIVE SUSCEPTIBILITY MAPPING.....	63
3.1 Abstract.....	63
3.2 Introduction.....	64
3.3 Materials and methods	67

3.3.1 Preparation of ICAM-1 specific nanoparticles (Leukocyte-mimetic nanoparticles (LMN))	67
3.3.2 Animal model of acute inflammation	68
3.3.3 Near-IR optical and MR imaging of mice	68
3.3.4 Histological sections	69
3.3.5 Quantification of radiolabeled LMN.....	70
3.3.6 Surface plasmon resonance (SPR) analysis	70
3.3.7 Statistical analysis	70
3.4 Results.....	71
3.5 Discussion.....	81
REFERENCES	90

CHAPTER 4 NOVEL STRATEGY FOR SELECTION OF MONOCLONAL ANTIBODIES AGAINST HIGHLY CONSERVED ANTIGENS: PHAGE LIBRARY PANNING AGAINST EPHRIN-B2 DISPLAYED ON YEAST	95
4.1 Abstract.....	95
4.2 Introduction.....	96
4.3 Materials and methods	98
4.3.1 Selection and expression of ephrin-B2-specific scFvs	98
4.3.2 Expression of scFv	99
4.3.3 Cell culture.....	99
4.3.4 Immunofluorescence flow cytometry	100
4.3.5 Conversion of scFv into scFv-Fc	101
4.3.6 Conformation specificity and selectivity of EC8 against ephrin-B2	101
4.3.7 Competition assay	101
4.3.8 Immunoprecipitation of ephrin-B2 by mAb EC8	102
4.3.9 Immunofluorescence microscopy for ephrin-B2 labeling and internalization by EC8.....	102
4.3.10 RT-PCR.....	103
4.3.11 Immunohistology of tumor xenograft	103
4.3.12 Immunohistology of human tissue array.....	104
4.3.13 Statistical analysis	105

4.4 Results.....	105
4.4.1 Novel strategy of selecting antibodies against ephrin-B2.....	105
4.4.2 Characterization of single-chain antibody fused to Fc domain.....	107
4.4.3 mAb EC8 blocked ephrin-B2 interaction with EphB4 and was internalized by ephrin-B2 ligation	112
4.4.4 EC8 detection of ephrin-B2 expression in tumor tissues and tumor- associated vasculature	113
4.4.5 EC8 detection of the upregulation of ephrin-B2 in diverse human tumors of epithelial origin	115
4.5 Discussion.....	116
REFERENCES	120
CHAPTER 5 CONCLUSIONS AND FUTURE DIRECTIONS.....	124
5.1 Summary.....	124
5.2 LMN as a biomimetic: potential caveats and improvements.....	125
5.3 Application of LMN in cancer diagnosis: implications and challenges	131
5.4 Application of LMN in assessing cerebral inflammation and ischemic reperfusion injury post stroke	134
5.5 Developing theranostic LMN	137
REFERENCES	140
APPENDIX A YEAST SURFACE TWO-HYBRID FOR QUANTITATIVE IN VIVO DETECTION OF PROTEIN-PROTEIN INTERACTIONS VIA THE SECRETORY PATHWAY	149
A.1 Abstract	149
A.2 Introduction.....	150
A.3 Experimental procedures.....	153
A.3.1 YS2H vector design	153
A.3.2 Yeast transformation, magnetic affinity cell sorting, and library construction.....	153
A.3.3 Immunofluorescence flow cytometry	154
A.3.4 Protein expression	155

A.3.5 SPR analysis.....	156
A.4 Results.....	156
A.4.1 The design of the YS2H.....	156
A.4.2 The validation of the yeast surface two-hybrid system using coiled coil interaction.....	158
A.4.3 YS2H detects specific interactions of antibodies and antigens.....	162
A.4.4 Discovery of activating mutations in the LFA-1 I domain	164
A.4.5 Antibody discovery: VHH against Botulinum neurotoxin protease	166
A.5 Discussion	170
REFERENCES	176

APPENDIX B CELL SURFACE ASSEMBLY OF HIV GP41 SIX HELIX BUNDLES FOR FACILE, QUANTITATIVE MEASUREMENTS OF HETERO-OLIGOMERIC INTERACTIONS.....	180
B.1 Abstract	180
B.2 Research summary	181
B.3 Materials and methods	191
B.3.1 Generation of YS2H constructs.....	191
B.3.2 Growth of yeast cells with protein displayed on surface.....	191
B.3.3 Immunofluorescence flow cytometry.....	192
B.3.4 Measurement of 6HB kinetics on yeast surface	192
REFERENCES	194

LIST OF FIGURES

1.1 Diagram of the entire process of leukocyte-endothelium interaction under inflammation. Serial events involve: Tethering and rolling – transient binding between selectin ligands (or carbohydrate) on leukocyte binds to selectins on endothelium, blood flow causes weakly bound leukocytes to roll along endothelial surface; Firm adhesion - activation of β_2 integrin leads to tighter adhesion; Diapedesis - interaction with specific CAMs leads to extravasation. Image adapted from Figure 2-44 part 3 of 3 Immunology, 6/e (Garland Science 2005).....	4
1.2 (a) Conformational change of β_2 integrin from quiescent to active state. (b) Conversion of I domain from low-affinity conformation to high-affinity conformation that is ready for interaction with ICAM-1. Image adapted from Figure 1A in [38] and Figure 12B in [24].	7
1.3 Scheme of our conception of iron oxide nanomicelles for facile coating of proteins, which can later evolve into biomimetics for MRI-guided applications in biological systems.	9
2.1 A schematic diagram of iron oxide nanocrystals encapsulated into a micelle-like layer composed of amphiphilic phospholipid copolymers (stage I–II) and subsequent protein conjugation for molecular targeting (stage III).	34
2.2 Uniformly sized, monodispersed SPIO with 15 nm core revealed by TEM. A close up view on top demonstrates a dark halo corresponding to nickel ions (black arrow) chelated by NTA groups surrounding SPIO. On the bottom is the negative staining of protein-conjugated SPIO with proteins and PEG groups darkly stained (white arrow), in contrast to a brighter phospholipid layer.	35
2.3 (a) Flow cytometry measurements of HeLa cells stained with different I domains (10 $\mu\text{g}/\text{ml}$) labeled with AF488. Non-stained HeLa cells are shown in grey shaded histograms. In a competition assay, non-labeled I domains were used at 50 $\mu\text{g}/\text{ml}$. (b) Shown in green is immunofluorescence staining of ICAM-1 in HeLa cells using F265S/F292G labeled with AF488. Nuclei staining by DAPI is shown in blue.....	36
2.4 (a) Flow cytometry measurements of HeLa cells stained with nanoparticles (25 $\mu\text{g}/\text{ml}$ of SPIO and 10 $\mu\text{g}/\text{ml}$ of I domains) conjugated with different I domains. Non-labeled I domains as a competitor were used at 50 $\mu\text{g}/\text{ml}$. (b) ICAM-1 dependent internalization of SPIO into HeLa cells was confirmed with confocal fluorescence microscopy (nanoparticles labeled with AF488) and Perls' Prussian blue staining. ...	37
2.5 The amount of SPIO internalized into HeLa or 293T was measured by radioisotope measurement of ^3H -phospholipid incorporated into SPIO nanoparticles. SPIO nanoparticles were coated with either F265S/F292G (LMN) for ICAM-1 targeting or with D137A (NTN) as a control.	38

2.6 T2* and susceptibility images of agarose-embedded HeLa cells that were labeled with 200-0 µg/ml of LMN.	39
2.7 A comparison of iron mass estimated by QSM technique and radioisotope measurement. Shown are the measurements of agarose-embedded free LMN (closed circles) and LMN internalized into HeLa cells (closed circles).	39
2.8 Confocal fluorescence images of murine b.End3 cells before and after LPS treatment and HeLa cells stained with murine (top) and human (bottom) I domains (F265S/F292G) labeled with AF594. Nuclei staining by DAPI is shown in blue.	40
2.9 Immunofluorescence images of GFP-expressing HeLa xenograft tumor tissue costained with F265S/F292G-AF594 and anti-murine CD31 antibodies. Skin tissues from non-tumor bearing mice were used as control.	41
2.10 (a) The percentages of endothelium costained with CD31 and F265S/F292G within the tumor, in the periphery (300 µm from the tumor), and in the skin were determined from immunohistology (n = 6). (b) Vascularity within the tumor, in the periphery (300 µm from the tumor), and in the skin was quantified using Chalkley's method (25 random points per field of view) (n = 3; *p < 0.05, **p < 0.01).	42
2.11 <i>In vivo</i> near-IR imaging of mice at 50 h after intravenous injection of NTN vs. LMN. GFP indicates the growth of HeLa ('1') and 293T ('2') tumors.	43
2.12 <i>Ex vivo</i> near-IR imaging of mice at 50 h after intravenous injection of NTN vs. LMN. GFP indicates the growth of HeLa ('1') and 293T ('2') tumors. The distribution of nanoparticles into the major organs ('3'-'8') were also examined.	44
2.13 Near-IR fluorescence intensities of HeLa and 293T tumors at different time points after intravenous injection of LMN vs. NTN (n = 4; **P < 0.01, ***p < 0.001).	45
2.14 (a) Perls' Prussian blue staining of tumor sections collected at 50 h after the injection of LMN vs. NTN. Stained iron is marked with black arrows. (b) Percentage of cells stained in Prussian blue (top) and the intensity of Prussian blue in the field of view (bottom) within tumor sections (n = 3; ***p < 0.001 between LMN vs. NTN in HeLa tumor. †††p < 0.001 between HeLa and 293T tumor using LMN).	46
2.15 (a) Immunofluorescence imaging of tumors at 4 h post-injection of LMN. Tumor sections were also stained with anti-CD31 antibody for delineating vasculature. LMN localization into the tumor vasculatures was indicated with white arrows. (b) Fluorescence imaging of tumors at 4 h post-injection of NTN.	47
2.16 (a) <i>In vivo</i> near-IR whole body imaging of LMN vs. NTN distribution in mice 1 h after nanoparticle injection. Mice were exposed to LPS ('1') and PBS ('2') for 3, 12, 24, or 72 h at the time of nanoparticle delivery. (b) Fluorescence intensities of LMN at LPS vs. PBS injection sites were shown (n = 3; **p < 0.01, ***p < 0.001 between LPS and PBS site at specific time points; †p < 0.05 between 12 h and 72 h at LPS site).	

(c) T2* magnitude and susceptibility mapping images of nanoparticle distribution in mice at 4 h after nanoparticle injection. Mice were exposed to LPS/PBS for 12 h at the time of nanoparticle injection. Bright spot identified by susceptibility mapping as the accumulation of SPIO was indicated with crosshair.	49
2.17 (a) <i>In vivo</i> near-IR whole body imaging of LMN vs. NTN distribution in mice at 1, 8, 25 h post-injection of nanoparticles in mice exposed to systemic LPS for 12 h or control mice with no treatment. (b) LMN vs. NTN distributions into the liver were quantified by near-IR optical imaging (n = 3; *p < 0.05, ***p < 0.001 between LMN vs. NTN at specific time points).	51
2.18 (a) MR imaging of LMN vs. NTN distribution in mice at 1, 8, 25 h post-injection of nanoparticles in mice exposed to systemic LPS for 12 h or control mice with no treatment. (b) LMN vs. NTN distributions into the liver were quantified by QSM (n = 3; *p < 0.05, ***p < 0.001 between LMN vs. NTN at specific time points).	52
3.1 (a) Structural model of the complex of ICAM-1 domain 1 and LFA-1 I domain. White spheres depict allosteric activation sites along the peptide backbone. Metal ion and two oxygen atoms of water molecules are depicted as colored spheres. Residues that coordinate to the metal ion are shown as sticks. Mutations of Phe265→Ser (F265S), Phe292→Gly (F292G), and Asp137→Ala (D137A), and N and C termini are indicated. Figure adapted from Hu et al [44]. (b) SPR measurement of the binding kinetics of I domain variants F265S/F292G and D137A to immobilized murine ICAM-1. F265S/F292G exhibits high ICAM-1 binding affinity ($K_D = 2$ nM), while variant D137A indicates no (not determinable) binding affinity.	71
3.2 Schematic diagram of LMN and NTN. LMN (ICAM-1 specific) and NTN (non-ICAM-1 specific) differ only in surface-conjugated targeting moiety.	72
3.3 SPR measurement of the binding kinetics of LMN and NTN to varying concentrations of immobilized ICAM-1 (low, intermediate, and high correspond to approximately 200, 1000 and 3,250 molecules/ μm^2 , respectively). LMN binding was limited to the surface coating with higher than normal ICAM-1 site density, while LMN binding to the basal ICAM-1 surface was the same as the background levels seen with NTN.	73
3.4 Fluorescent heat maps (color) are superimposed over brightfield images (grey scale), indicating greater nanoparticle localization in the liver in LPS/LMN-treated mice compared to that of negative controls, with observable localization diminishing over time.	74
3.5 MRI-QSM reconstructions of the (a) liver and (b) spleen. QSM technique reveals greater nanoparticle localization in the liver of LMN/LPS-treated mice compared to that of negative controls, while greater nanoparticle localization is observed in the spleen in LPS-treated mice, regardless of injected nanoparticle. Portions of these results were previously described in Chen et al [31], and reproduced here.	

Representative QSM maps at each time point post-injection (p.i.) of nanoparticles are shown: organ-specific QSM heat maps (color) are superimposed over MRI T2* weighted EFGRE scans used for navigational reference (gray)..... 75

3.6 Fluorescence detected in the liver region of mice analyzed using near-IR optical imaging at 1, 8, and 25 hours post nanoparticle injection. 76

3.7 Measurement of nanoparticle accumulation in the liver, spleen, and kidneys from MRI-QSM analysis..... 77

3.8 Radioactivity measurement of ³H labeled nanoparticles from the liver, kidney, spleen, and blood 1 hour post-nanoparticle injection, normalized to the total counts of radioisotope decay per mouse. All modalities measured high liver-specific nanoparticle localization in LPS/LMN-treated mice 1 hour post nanoparticle injection over controls. QSM measured high spleen-specific nanoparticle localization in LPS-treated mice, regardless of nanoparticle injected. Trends persist through 25 hours post nanoparticle injection. Portions of these results were previously described in Chen et al [31], and reproduced here. One-way analysis of variance with Tukey HSD post-test at 95% confidence interval are summarized in each figure (*** p < 0.001, ** 0.001 < p < 0.01, * 0.01 < p < 0.05). 78

3.9 Measurements of nanoparticles in the spleen and liver obtained by radioisotope measurement and by QSM are linearly related. Error bars indicate 95% confidence interval. Dotted line indicates 95% confidence interval for linear regression fitting. n = 3 for each treatment and imaging regimen. 79

3.10 H&E stain of liver tissue sections show distinct dilation of liver tissue, characteristic of sepsis. 81

3.11 Prussian Blue staining of liver tissue sections shows SPIO accumulation primarily in the endothelial cells and Kupffer cells, with markedly more staining in LPS treated subjects with injected LMN..... 82

3.12 CD68 (brown) and Prussian Blue (blue) staining indicates primary localization of iron deposition in Kupffer cells. Examples of hepatocytes (arrow), endothelium (double headed arrow), and Kupffer cells (arrowhead) are marked. 83

4.1 (a) A schematic diagram of phage panning against antigens expressed in yeast display system [34]. (b) Immunofluorescence flow cytometry measurements of protein and phage binding to yeast cells. Surface-displayed ephrin-B2 was detected by the binding of anti-Myc antibody ('Myc') as well as recombinant human EphB4-Fc ('EphB4') to yeast cells (top panel). Progressive enrichment of phage clones from first three rounds of panning (denoted as '1 st', '2 nd' and '3 rd') was detected by antibody against His tag (bottom panel). Histograms drawn in shaded area and solid lines indicate antibody binding to uninduced and induced yeast cells, respectively. The percentage of phage clones with positive binding is indicated. 106

4.2 (a) SDS-PAGE of scFv-EB1 (lane '1') and scFv-EC8 (lane '2'). (b) Ephrin-B2 specific scFv binding to irrelevant yeast cells, yeast cells with expression of ephrin-B2 ectodomain, 293T cells, and 293T cells with transient expression of full-length ephrin-B2. Shown are the histograms of cells labeled with secondary antibody with (solid line) and without (shaded area) ephrin-B2 specific scFv as primary antibody.	107
4.3 Sequence alignment of scFv-EA6, scFv-EB1, and scFv-EC8. Complementarity determining regions (CDR), the beginning of immunoglobulin variable heavy (VH) and variable light (VL) chain domains, and the linker connecting VH and VL are noted. * indicates amino acids differ between scFvs.	108
4.4 SDS-PAGE images of EC8 resolved under reducing (R) and non-reducing (NR) conditions.	109
4.5 EC8 (solid line) binding to yeast cells, 293T with stable expression of ephrin-B2, and murine ovarian epithelium. The binding of isotype control is shown in shaded area.	110
4.6 Flow cytometry measurements of EC8 binding to 293T cells are shown in filled squares. First order Langmuir adsorption model was used to fit the data to estimate equilibrium dissociation constant (K_D).	111
4.7 (a) Conformation specificity of EC8 against ephrin-B2 was examined by flow cytometry with ('+') or without ('-') incubating cells either in 6 M guanidine hydrochloride ('GnHCl') for 20 min or in elevated temperature at 80°C ('Heat') for 10 min. (b) Western blot image of immunoprecipitated ephrin-B2 from 293T cells with ('+') or without ('-') EC8 antibody, detected by rabbit ephrin-B2 polyclonal antibody.	111
4.8 Flow cytometry measurements of EC8 binding to ephrin-B1 and ephrin-A5 displayed on yeast. Labeling of uninduced yeast cells is shown in shaded histograms.	112
4.9 Competition assay. Relative binding of EphB4 (100 nM) to yeast cells expressing ephrin-B2, preincubated with varying concentrations of EC8, was measured by flow cytometry. Affinity purified human IgG was included as isotype control. n = 3 independent measurements.	113
4.10 Confocal microscopic images of surface-bound EC8 and internalized ones before and after membrane permeabilization of 293T cells. Scale bar = 10 μ m.	114
4.11 (a) Flow cytometry measurements of EC8 binding to COLO205 and HCT116 cells (solid line) in comparison to the isotype control (shaded area). CHO cells with no ephrin-B2 expression were also included for comparison. (b) RT-PCR detection of ephrin-B2 expression in different cell lines.	114
4.12 Immunostaining of ephrin-B2 on human colon cancer xenografted in mice. Control denotes immunostaining without EC8 as a primary antibody. Tumor and	

stromal cells are indicated with arrowhead and arrow, respectively. Circle indicates murine endothelium stained with EC8. Scale bar = 20 μm	115
4.13 (a&b) Immunostaining of ephrin-B2 expression in human tumor tissue arrays using EC8. Control denotes immunostaining without EC8 as a primary antibody. Tumor and stromal cells are indicated with arrowhead and arrow, respectively. Scale bar = 20 μm . PAC = Papillary Adenocarcinoma; AC = Adenocarcinoma; BR = Bronchus; AL = Alveoli; SC = Squamous Cell Carcinoma; SAC = Serous Adenocarcinoma. IDC = Nonspecific Infiltrating Duct Carcinoma. (c) Immunofluorescence staining on human colon tumor tissue demonstrating that EC8 (red) detects ephrin-B2 expressions in both cancer cells and tumor-associated vasculature (green). Blown up views of the two areas indicated with a dashed box are shown in the right panel. Scale bar = 100 μm	117
5.1 Quantitative PCR of HMEC-1 cells on the mRNA level of inflammatory markers (ICAM-1 & VCAM-1), in comparison to housekeeping gene PECAM-1. Cells were treated with 50 $\mu\text{g}/\text{mL}$ nanoparticles (coated with no protein: mSPIO; coated with inactive I domain mutant D137A: NTN; coated with active I domain mutant F265S/F292G: LMN.) or 10 $\mu\text{g}/\text{mL}$ LPS at 37°C for 3 h. Inset shows the result when cells were incubated with 20 $\mu\text{g}/\text{mL}$ of I domain. Refer to Table 5.1 for specific versions of nanoparticles.....	127
5.2 (a) Exposure of PCDA vesicle to a UV lamp resulted in the relaxation of photoproduct which was initially blue to a purple polymer. (b) Exposure of LMN v1.0 and v2.0 to chloroform over time resulted in the disrapture of v1.0, but not v2.0.....	130
5.3 Two-photon laser scanning microscopy (TPLSM) imaging of ICAM-1 (FITC-labeled mAb) upregulation in mouse cortical vessels (Texas-red dextran) under systemic LPS-treatment (right panel), which mimics artificially induced acute neuroinflammation. Animal treated with the same volume of PBS (left) was shown as a negative control.	136
5.4 Absorbance spectrum of LMN loaded with (right) and without (left) celastrol. Wavelength where celastrol has maximal absorption is marked in black.....	138
5.5 Crystal violet staining of HeLa cells after incubation with different amounts of LMN-celastrol for 24 h at 37 °C. Dead cells would no longer attach to the surface of flask, thus not appear in the field of view. The concentration of LMN and the corresponding concentration of celastrol are labeled.	139
A.1 (a) A map of the YS2H vector is drawn with restriction enzyme sites and genes labeled. The bait protein is expressed as a fusion to Aga2 on cell surface, whereas the prey protein is expressed as a secretory form. (b) Schematic diagram of the expression cassette and protein-protein interactions (acid base coiled coils) via the secretory pathway is depicted. The prey bound to the bait is detected by antibody binding to the	

Myc tag. FLAG (DYKDDDDK) and Myc (EQKLISEEDL) epitope tags are fused to the C-terminal of the bait and prey proteins, respectively, and are used to measure the surface expression of the bait and the amount of the prey that is bound to the bait... 157

A.2 (a) Schematic diagram of the expression cassette and protein-protein interactions (acid base coiled coils) via the secretory pathway is depicted. The prey bound to the bait is detected by direct GFP readout from split GFP complementation. (b) The deletion of signal sequence for the prey and bait proteins leads to their expression in the cytosol..... 158

A.3 Detection of coiled coil interactions by epitope expression and GFP complementation. (a) A schematic diagram (adapted from De Crescenzo *et al.* [17]) of the acid (En)-base (Kn) coiled coils with n indicating the number of heptad repeats. (b-c) The detection of coiled coil interactions by antibody binding to Myc tag (b) or direct GFP readout (c) using flow cytometry. Antibody binding to the FLAG tag measures the level of the base coil expression on cell surface. (d) Shown are the plots of GFP complementation caused by the coiled coil interactions occurring inside the cells. The numbers in each plot (b-d) indicate the MFI of an entire population shown in filled histogram. The thin lines represent the histograms of uninduced clones. The pairs of bait and prey are denoted for each column as bait:prey. The labels K3 and E3 indicate that the other coil is deleted from the expression vector. 160

A.4 The correlation of the affinity measured by SPR [17] with the detection by epitope tag or direct readout of GFP complementation caused by coiled coil interactions occurring in the secretory pathway (a, b, & d) or in the cytosol (c). The data are from three independent experiments involving different clones (means \pm SE). The smooth solid lines are drawn by connecting data points. (d) The MFI of eGFP complementation from the coiled coil interactions is plotted as a function of their on-rate, measured by SPR [17]. The solid line represents a least square fit to the data points. 161

A.5 Detection of specific interactions between antibodies and antigens in YS2H. (a) Schematic diagram of the expression cassette used to study antigen (bait) and antibody (prey) interactions. (b-c) Shown are the histograms of the interactions of the wild-type and the high affinity (HA) I domains as baits and activation-insensitive antibody, TS1/22 (b) activation-specific antibody, AL-57 (c) as preys. Filled histograms are of antibody binding to Myc and FLAG tags to the induced clones. Thin black lines represent antibody binding to uninduced clones as controls. The numbers in each plot indicate the means \pm SE of the MFI of the filled histograms from three independent measurements. 162

A.6 (a) Cartoon diagrams of low (inactive) and high affinity (active) conformations of the LFA-1 I domains. The regions that are structurally conserved between two states are colored gray. The regions that differ structurally are colored in magenta and

yellow for the inactive and the active conformations, respectively. The metal ions in the metal ion-dependent adhesion site are shown as spheres. The N and C termini and $\alpha 7$ -helix are labeled. (b) The structure of the I domain is shown in complex with the first domain of ICAM-1 (D1). Gray spheres with a white center display the positions for the hot spots for allosteric activation found in our previous study [10]. The metal ion and three oxygen atoms of water molecules are depicted as spheres. The residues that coordinate to the metal ion are shown in stick models. The structures of the I domains and the complex of I domain with the ICAM-1 were modeled based on the crystal structures, as described previously [31]...... 163

A.7 (a) Myc expression of the I domain library before sort and after first and second sort are shown. The numbers indicate the percentage of the clones within the gated region. Antibody binding was measured with 10 mM MgCl₂ or no metal ions with 10 mM EDTA. (b) Two activating mutations from the second sort were of F265S and L295P. The numbers in each plot indicate means \pm SE of the MFI of the filled histograms from three independent measurements. (c-d) SPR measurements of L295P (c) and F265S (d) binding to scFv AL-57. I domains were injected over the scFv AL-57-coated chip as a series of 2-fold dilutions beginning at 500 nM..... 165

A.8 (a) Specific binding of the VHHs against A-LC and B-LC was confirmed in YS2H by Myc expression. (b) New VHHs against B-LC protease were isolated by YS2H. The numbers in each plot indicate means \pm SE of the MFI of the filled histograms from three independent measurements. 167

A.9 SPR measurements of B8 (a) and G6 (b) binding to BoNT/A-LC. A-LC was injected at a series of 2-fold dilutions beginning at 160 nM to the B8-coated and 400 nM to the G6-coated chip. 168

A.10 Sequence analysis of VHHs. Cysteines are highlighted in yellow for the pair that forms a conserved disulfide bond or in orange for the pair that forms extra disulfide bonds. The framework region (FR) and complementarity determining regions (CDR) are noted. 169

B.1 (a) Schematic view of gp41 elements. Residue numbers at boundaries of each element are shown. (b) Ribbon drawings of side and top views of 6HB are shown (PDB ID: 1AIK [3]). N- and C-termini of helices are labeled. Helical wheel diagram is shown on the right, viewed from C-terminal end of NHR. (c) Depicted are the events of HIV-1 membrane fusion and the mechanism of fusion inhibition by soluble N- or C- peptides. (d) Segments of NHR and CHR of gp41 are shown. ‘a’-‘g’ denote the positions of heptad repeats in a helical wheel. Interaction pairs are delineated with dashed lines. N and C peptides (orange) as well as single point mutations (green) used in this study are indicated. CP32M contains rationally designed mutations, shown in pink, some of which were made to introduce intramolecular salt bridges, shown in pink square brackets. FP = fusion peptide; NHR = N-terminal heptad repeat; CHR =

C-terminal haptad repeat; MPER = membrane-proximal external region; TM = transmembrane domain; CP = cytoplasmic domain..... 182

B.2 Assembly of 6HB on yeast surface. (a) A schematic view of 6HB displayed on yeast surface by YS2H is depicted. (b) In YS2H, bidirectional promoter Gal1/Gal10 drives the expression of surface-anchored ‘bait’ as a fusion to Aga2 and secretory ‘prey’, the level of which is measured by antibody binding to short epitope tag, Flag and Myc, fused to bait and prey, respectively. SS = signal sequence. (c&d) Immunofluorescence flow cytometry histograms of antibody binding to Flag and Myc tags and 6HB-specific antibodies (D50, D5). White and grey filled curves are histograms of uninduced and induced yeast cells, respectively. ‘*’ denotes Aga2-fused bait; ‘-’ denotes no peptide; wt: wild type. 185

B.3 Dissociation kinetics of C peptide inhibitors measured in YS2H. The loss of antibody binding to Myc (MFI_{Myc}) is plotted as a percentage after normalization to the level of antibody binding to Flag (MFI_{Flag}) (n = 5). A two phase kinetic model was used to fit the data, shown in solid or dotted lines. 190

LIST OF TABLES

3.1 Two-way analysis of variance of organ-specific nanoparticle accumulation resulting from the treatment of LPS, the type of nanoparticle administered, or due to the interaction between both factors, quantified by QSM technique.	80
5.1 Summary of LMN evolution of their property changes.	129
A.1 Comparison of equilibrium dissociation constants (K_D) predicted from YS2H <i>versus</i> directly measured using surface plasmon resonance.....	172
B.1 Quantification of the binding kinetics of C peptides to N peptides.....	187

LIST OF ABBREVIATIONS

3D	three-dimensional
5H	five helix
6HB	six helix bundle
AC	adenocarcinoma
AF	Alexa Fluor
AL	alveoli
ANOVA	analysis of variance
a.u.	arbitrary unit
BoNT	Botulinum neurotoxin
BR	bronchus
BSA	bovine serum albumin
CDR	complementarity determining region
CHO	Chinese hamster ovary
CHR	C-terminal heptad repeat
COSMOS	calculation of susceptibility through multiple orientation sampling
CP	cytoplasmic domain
d	day
DAPI	4',6-diamidino-2-phenylindole
DLS	dynamic light scattering
DMEM	Dulbecco's modified Eagle's medium
DOGS	dioleoyl-glycero-succinate
DOX	doxorubicin
DPPE	dipalmitoyl-glycero-phosphoethanolamine
EDTA	ethylenediaminetetraacetic acid
eGFP	enhanced green fluorescent protein
Eph	erythropoietin-producing hepatocellular
EPR	enhanced permeability and retention
FBS	fetal bovine serum
Fc	constant region (of IgG)
FGF	fibroblast growth factor

FP	fusion peptide
FR	framework region
g	gram
G-CSF	granulocyte-colony stimulating factor
GFP	green fluorescent protein
GnHCl	guanidine hydrochloride
h (hr)	hour
HA	high affinity
H&E	hematoxylin and eosin
HEK	human embryonic kidney
HRP	horseradish peroxidase
ICAM	intercellular adhesion molecule
ICU	intensive care unit
IDC	nonspecific infiltrating duct carcinoma
iFP	interstitial fluid pressure
IL	interleukin
IR	infrared
l	liter
LC	light chain
LFA	lymphocyte function-associated antigen
IgG	immunoglobulin G
IgSF	immunoglobulin superfamily
I/R	ischemia/reperfusion
JAM	junctional adhesion molecule
kDa	kilodalton
LAMA4	laminin α 4
LMN	leukocyte-mimetic nanoparticle
LPS	lipopolysaccharide
M	molar
mAb	monoclonal antibody
μ Ci	microcurie
MCP	monocyte chemotactic protein

MFI	mean fluorescence intensity
mg	milligram
μg	microgram
MIDAS	metal ion-dependent adhesion site
min	minute
ml	milliliter
μl	microliter
μm	micrometer
μM	micromolar
mm	millimeter
mM	millimolar
MMP	matrix metalloproteinase
MPER	membrane-proximal external region
MRI	magnetic resonance imaging
ms	millisecond
MUC	mucin
NA	not analyzed
nCi	nanocurie
ng	nanogram
NHR	N-terminal heptad repeat
NIR	near-infrared
nm	nanometer
nM	nanomolar
NO	nitric oxide
NR	non-reducing
NTA	nitrilotriacetic acid
NTN	non-targeted nanoparticle
OD	optical density
O/N	overnight
PAC	papillary adenocarcinoma
PAGE	polyacrylamide gel electrophoresis
PBS	phosphate-buffered saline

PCA	protein-fragment complementation assay
PCDA	10,12-pentacosadiynoic acid
PCR	polymerase chain reaction
PDGF	platelet-derived growth factor
PECAM	platelet endothelial cell adhesion molecule
PEG	polyethylene glycol
PET	positron emission tomography
p.i.	post-injection
pM	picomolar
PMN	polymorphonuclear leukocyte
ppm	parts per million
PTX	paclitaxel
QSM	quantitative susceptibility mapping
RES	reticuloendothelial system
ROI	regions of interest
rpm	revolutions per minute
R	reducing
RT	room temperature
RTK	receptor tyrosine kinase
RT-PCR	reverse transcriptase-polymerase chain reaction
SAC	serous adenocarcinoma
SC	squamous cell carcinoma
scFv	single chain variable fragment
SD	standard deviation
SDF	stromal cell-derived factor
SDS	sodium dodecyl sulfate
SE	standard error
SIRS	systemic inflammatory response syndrome
SPIO	super paramagnetic iron oxide
SPR	surface plasmon resonance
SS	signal sequence
TE	echo time

TEM	transmission electron microscopy
TGF	transforming growth factor
TM	transmembrane domain
TNF	tumor necrosis factor
tPA	tissue plasminogen activator
TPLSM	two-photon laser scanning microscopy
TR	repetition time
USPIO	ultrasmall particles of iron oxide
UV	ultraviolet
VCAM	vascular cell adhesion molecule
vdW	van der Waals
VEGF	vascular endothelial growth factor
VH	variable heavy
VHH	variable domain of heavy chain from heavy chain-only antibody
VL	variable light
v/v	volume per volume
wk	week
wt	wild-type
w/v	weight per volume
YS2H	yeast surface two-hybrid
YSD	yeast surface display

LIST OF SYMBOLS

Symbol	Variable or parameter	Dimensions
K_D	equilibrium dissociation constant	nM
k_{off}	dissociation rate	s^{-1}
k_{on}	association rate	$\text{M}^{-1}\text{s}^{-1}$

CHAPTER 1

INTRODUCTION

On the evening of 29 December 1959, in one of his best known talks, titled ‘There’s plenty of room at the bottom’, Richard Feynman probed into the exciting possibility of manipulating things at the molecular or even atomic level even before the existence of the buzz word ‘nanotechnology’. If we treat this paper as the blueprint for nanotechnology, many advances of nanobiotechnology today might have failed Mr. Feynman because they are still quite far from his original vision, unlike other important technological improvements such as the improved performance of electron microscopes and the miniaturization of computers. With our current tools, we are still limited in the small scale biological processes we can observe by simply ‘looking at the thing,’ not to mention tracking and controlling these processes in real time *in situ*. Since biological systems are exceedingly intricate and marvelous in the world of the small, we want to echo Mr. Feynman here by creating a biomimetic system at nanoscale that is also easy to maneuver. We endowed it with the traits of inflamed leukocytes, as they participate in almost every inflammatory response and inflammation is the key to a spectrum of human diseases. Through *in vitro* analysis of its cellular adherence followed by uptake as well as *in vivo* examination of its homing to artificially-induced inflammation, we want to provide a different approach for manipulating nanoscale machineries and propose a potential application of them in noninvasive quantitative diagnosis.

1.1 Nanoparticle-based biologic mimetics

Through interdisciplinary interactions between solid chemistry, biology and material science, bottom-up designs of biological mimics has been made possible. One particular example is metal nanoparticles (e.g., iron oxide [1], quantum dots [2] and gold [3]) conjugated to biologically relevant molecules (e.g., peptides, proteins and carbohydrates) with conformationally favorable orientations. Nanoparticles offer an easy way to present active parts of biomolecules as well as a large surface area for coupling multiple functional groups [4]. They can become stable and effective substitutes for current systems in applications such as drug delivery and biosensing, which typically require high spatial-temporal specificity at micron to nanometer scales. Even though the use of nanoparticles in biological systems has increased dramatically since the first water-soluble, ligand-capped nanoparticle developed almost 20 years ago [5]; we still have a long way to go towards true adaptation of them into ‘nanorobots’ functioning just like other biological units. While accurate mimicking of biologically important machineries under physiological conditions remains challenging, successful camouflaging of nanomaterials in order to bypass physiological barriers and evade immune surveillance takes a great amount of effort. Therefore, devising biologically ‘smart’ biomaterials which are benign and able to hold extensive surrogating from biological systems will create a significant impact.

1.2 In vivo distribution of nanoparticles – size, composition and beyond

While metal nanoparticles have generated substantial interest and their properties have been thoroughly studied, they raise biodistribution and potential toxicity concerns because they can be quickly sequestered by the reticuloendothelial system (RES) and can remain in organs, such as the liver and spleen, for prolonged periods of time [6]. Design considerations, such as size, shape, surface coating and dosing, can be manipulated to prolong blood circulation and enhance treatment efficacy; unfortunately nonspecific distribution has not been avoidable so far. Renal excretion of nanoparticles is size dependent (rapid excretion happens when the hydrodynamic diameter < 5.5 nm and can be prevented when the hydrodynamic diameter > 15 nm [7]). Studies on nanoparticles of 35 nm diameter showed 5–10% of retention in the blood stream even after 8 h of injection [8]. Nanoparticles greater than 200 nm will typically localize to liver, kidney, lung, spleen and to a lesser extent in bone marrow [9]. Most studies have reached a consensus that nanoparticles with a proper surface coating (such as pegylation) smaller than 100 nm have reduced plasma protein adsorption on their surface, reduced hepatic filtration, longer blood residence time and higher rate of extravasation into permeable tissues [10]. Surprisingly, the composition of nanomaterials, which strongly influences their physical properties, appears not to be the main determining factor for their behavior in biological environments [11]. So far, cytotoxicity effects have been more affirmed in certain materials such as cadmium-based quantum dots [12], compared with gold and iron oxide nanoparticles. Nevertheless, awareness should be paid to implicit toxicity, which largely comes from the interaction of particles with immune cells and their effect on the innate and adaptive immune response [13-14]. Even though still poorly

understood, such toxicity very likely depends on the size or surface state of the nanoparticles.

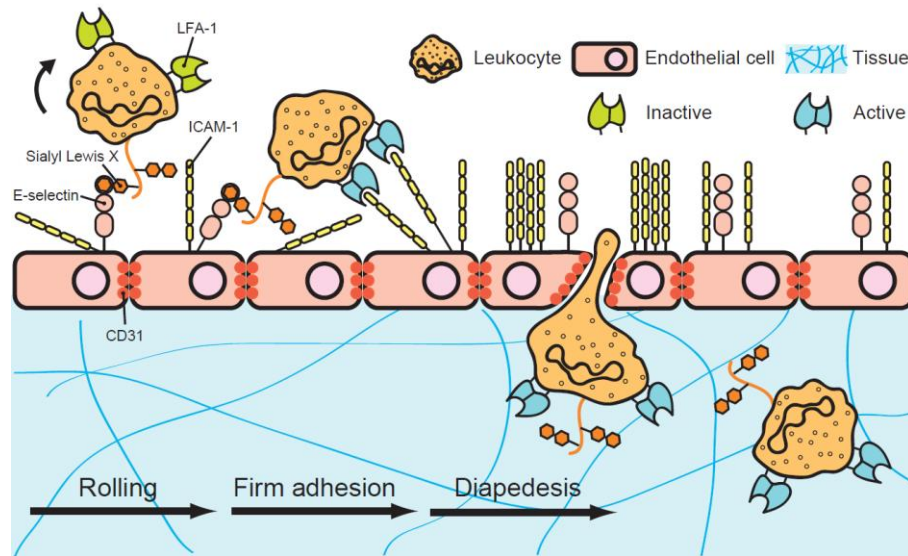


Figure 1.1: Diagram of the entire process of leukocyte-endothelium interaction under inflammation. Serial events involve: Tethering and rolling – transient binding between selectin ligands (or carbohydrate) on leukocyte binds to selectins on endothelium, blood flow causes weakly bound leukocytes to roll along endothelial surface; Firm adhesion - activation of β_2 integrin leads to tighter adhesion; Diapedesis - interaction with specific CAMs leads to extravasation. Image adapted from Figure 2-44 part 3 of 3 Immunology, 6/e (Garland Science 2005).

1.3 Biomimetics of leukocytes

Leukocyte-endothelium interaction is the hallmark event of inflammation. It involves sequential steps from rolling, firm adhesion to diapedesis (Figure 1.1). Cell adhesion molecules (CAMs) such as selectins (E-selectin [15] & P-selectin [16]), the

immunoglobulin superfamily (IgSF) (intercellular adhesion molecule (ICAM)-1 [17-18] & vascular cell adhesion molecule (VCAM)-1 [19]), as well as β_2 integrins (lymphocyte function-associated antigen (LFA)-1 ($\alpha_L\beta_2$) [20] & macrophage antigen (Mac)-1 ($\alpha_M\beta_2$) [21]), play crucial roles during this process through sophisticated orchestration including a prompt upregulation of expression level [22-23], a drastic conformational change [24] as well as a concerted synergistic effect [25-26].

These observations have led to a strong interest in the development of biological mimetics of leukocytes exploiting their strategies in achieving high selectivity towards disease tissue. Pioneering attempts include conjugating monoclonal antibodies (mAbs) against E-selectin, ICAM-1, VCAM-1, or selectin ligand sialyl-Lewis^x to polymer particles, which demonstrated that they could preferentially deliver payloads to trauma-induced endothelium *in vitro* [27-28]. Using flow chamber assays, beneficial interplay between functional molecules was also observed when two distinct receptor-ligand pairs were employed [29-30].

1.4 Current applications of leukocyte mimetics in biomedical imaging

Directly named after them or not, a large number of existing designs of nanoparticles adopt a similar molecular mechanism of leukocytes recruited to inflamed tissue for biomedical imaging. Successful systems which have been validated *in vivo* include: microbubbles conjugated with antibodies against P-selectin [31], ICAM-1 [32] or VCAM-1 [33] for ultrasound imaging; paramagnetic liposomes, microparticles of iron oxide or dextran coated ultrasmall particles of iron oxide (USPIO) conjugated with antibodies against ICAM-1 [34], VCAM-1 [35] or sialyl-

Lewis^x [36] for magnetic resonance imaging (MRI); ⁶⁴Cu-labeled polymer nanoparticles conjugated with antibodies against ICAM-1 [37] for positron emission tomography (PET); etc. Their diagnostic applications cover a plethora of inflammatory diseases, such as acute transplant rejection [32], autoimmune encephalomyelitis [33-34], renal tissue injury [31], acute brain inflammation [35] and hepatitis [36]. All of these studies helped to unravel important components we can utilize for engineering particles mimicking leukocytes in their strategy for specific adherence. Nevertheless, potential caveats exist with both antibody and carbohydrate ligands, as they are not able to present the physiological dynamics of adhesion molecules in regulating leukocyte-endothelium interaction. Therefore extensive tuning on the surface density of functional groups is necessary, especially when more than one type of ligand is coupled, and it can become a tedious process if chemical conjugation is involved. In addition, the incorporation of mAbs generated in rodents will raise issues like immunogenicity when applied to humans, even though the materials of the particles are actually benign.

1.5 Engineering active LFA-1 integrin – a physiological ligand during leukocyte adhesion

Aforementioned concerns draw us to a different scenario: instead of engaging exogenous antibodies to particles, why not use a native ligand of leukocytes, such as integrin? First of all, it will eliminate the potential risk of immune response against ‘foreign’ materials, because such particles directly tag them as ‘self’. What’s more, if we can somehow lock this ligand into its active state, it will reconstruct the same

allosterically inflamed leukocyte utilized for specific adherence, therein becoming truly biomimetic.

As the ligand of ICAM-1, β_2 integrin exists as two distinct conformations (Figure 1.2), which have been well studied structurally and functionally [38]. The

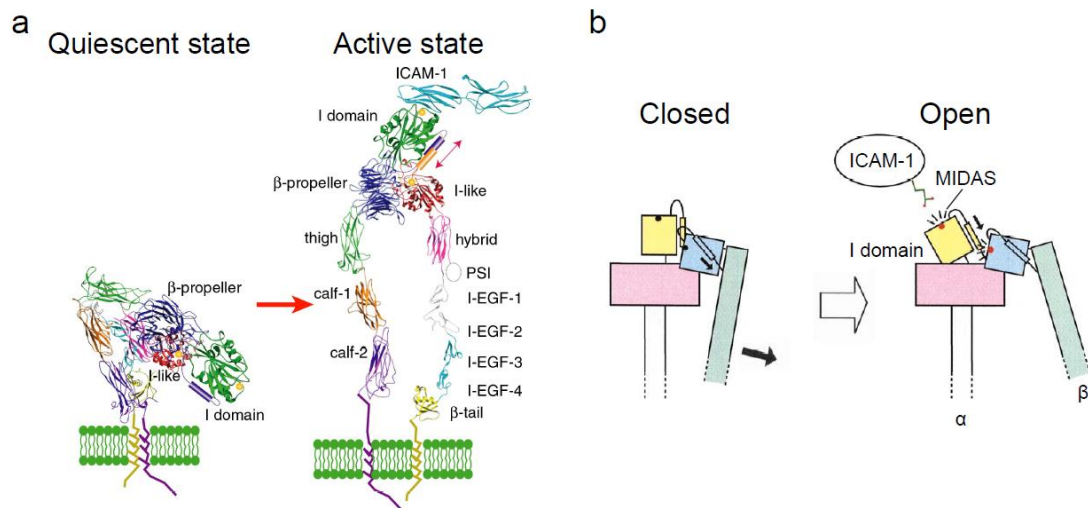


Figure 1.2: (a) Conformational change of β_2 integrin from quiescent to active state. (b) Conversion of I domain from low-affinity conformation to high-affinity conformation that is ready for interaction with ICAM-1. Image adapted from Figure 1A in [38] and Figure 12B in [24].

inserted domain (I domain), present in the α subunit of β_2 integrin, contains the ligand-binding site: metal ion-dependent adhesion site (MIDAS). Upon inflammatory signals, allosteric activation of β_2 integrin (Figure 1.2a) results in a switch of the I domain from a closed conformation having low affinity with ICAM-1, to an open conformation having high affinity (Figure 1.2b). In our recent studies, one allosteric mutant of $\alpha_1\beta_2$ I domain adopting the active conformation with a 200,000-fold increase in affinity was engineered through directed evolution using a yeast display

system [39]. Clone F265S/F292G contains two mutations (Phe-265 and Phe-292) both residing in a hot spot termed the ‘switch-allostery region’ previously speculated by expert inspection [40-41]. The switch-allostery region is tightly coupled to the active site MIDAS, and the twisting/shearing motion of their extensive interface plays critical roles in balancing open and closed conformations. Our data showed that this activating mutant has even 20-fold higher binding affinity than another high affinity mutant of $\alpha_M\beta_2$ I domain discovered earlier [42], likely due to a lower free energy of its I-domain-ICAM-1 complex.

1.6 Engineering iron oxide nanomicelles for facile coating of proteins – a platform for creating biomimetic nanoparticles in biomedical applications

Magnetite (Fe_3O_4) is a common magnetic iron oxide that offers attractive possibilities to biomedicine when it exists as nanocrystals [43]. Ever after the establishment of methodology 10 years ago [44], synthesis of magnetite nanoparticles in a size-controlled manner has been a routine practice in laboratories. Their dimensions are comparable to most biological molecules of interest, like a protein (5-50 nm) or a gene (10-100 nm long), thereby providing a small enough entity for biological modification. Since they are magnetic, they can be easily manipulated by an external magnetic field gradient, enabling actions like separation [45] and transport to desired locations [46]. They can also be used as hyperthermia agents because magnetic particles will heat up when a time-varying magnetic field is applied and energy is transferred from the exciting field [47]. Most importantly, sufficiently small magnetite nanoparticles are superparamagnetic. In the presence of external magnetic field, they

can effectively increase local magnetic inhomogeneity and alter environmental magnetic relaxation, making them an exceedingly good contrast agent for MRI [48].

In order to use iron oxide nanocrystals as a biolabel, their colloidal stability needs to be maintained under aqueous biological conditions. Studies on fluorescent semiconductor nanocrystals (quantum dots) showed that encapsulating them into phospholipid micelles mixed with a certain ratio of polyethylene glycol (PEG) polymer is able to generate water soluble nanoparticles, yet minimize nonspecific absorption and aggregation *in vivo* [49]. PEG-grafted lipids are poorly immunogenic and largely comparable to naturally occurring carriers such as lipoproteins, therefore have been used for drug delivery [50] and diagnostic imaging [51]. Due to high similarity between the surface topology of magnetite nanocrystals and quantum dots, we believe micelle encapsulation can benefit the biological stability of iron oxide nanoparticles in the same fashion. For ease of surface modification, it would also be

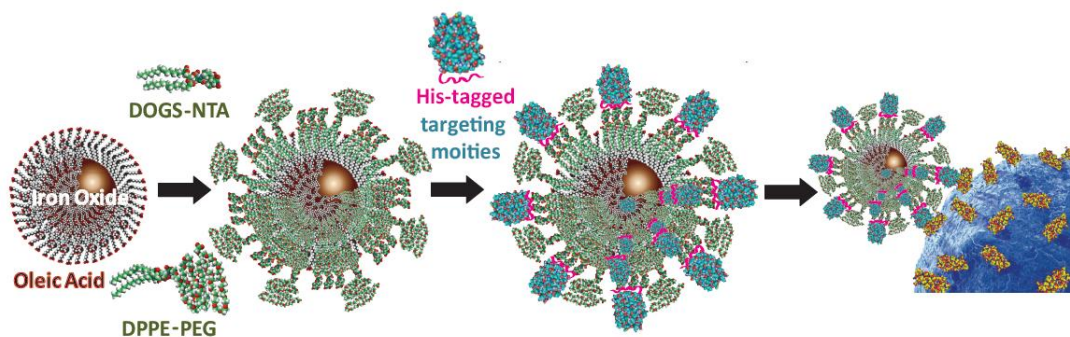


Figure 1.3: Scheme of our conception of iron oxide nanomicelles for facile coating of proteins, which can later evolve into biomimetics for MRI-guided applications in biological systems.

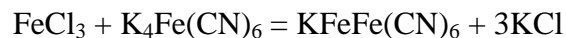
sensible to incorporate additional lipid components with functional head groups, so that potential perplexity involved in the chemical conjugation process of biological molecules (*e.g.* loss of function, aggregation) could be alleviated. In such a scenario, we introduced dioleoyl-glycero-succinyl-nitrilotriacetic acid (DOGS-NTA) (Figure 1.3). NTA nickel salt [52] has been widely used for the purification of proteins with His tag through high affinity ($K_D \sim 10^{-13}$ M) chelation. The presence of DOGS-NTA allows robust coupling of biological moieties to nanomicelles via non-covalent bonds, yet only requiring procedures as simple as mixing.

1.7 Iron-sensing assays

As a potential biosensor, magnetite nanomicelles are advantageous because the presence of their iron component can be detected by several methods including colorimetric assays, MRI and spectroscopy. We will briefly introduce them as follows:

1.7.1 Perls' Prussian blue

The original formula of Perls' Prussian blue staining technique was developed by German pathologist Max Perls (1843-1881). It is a chemical reaction between ferric iron and potassium ferrocyanide, which produces a highly water-insoluble and visible end product of ferric ferrocyanide (also known as Prussian blue). Ferrous iron does not produce a colored reaction product, thus is excluded from the visualization:



This assay utilizes hydrochloric acid to split off ferric irons from its biological complex with proteins, therefore it has been particularly useful in histological studies on conditions accompanied by varying degrees of iron excess [53] or hemosiderosis of

the bone marrow [54]. By the same token, it also becomes a routine method for demonstrating cellular or tissue retention of magnetite nanoparticles [55].

1.7.2 Ferrozine assay

Ferrozine is acknowledged as an effective chelator of ferrous iron and has been used for determination of iron in biological samples [56-57]. Ferrozine binds ferrous iron, but not ferric iron, into a water soluble complex that absorbs strongly at 550 nm. Because of this, ferrozine can also be used for colorimetric quantification of iron, unlike Perls' Prussian blue. An optimized ferrozine assay has been developed for total iron determination in cell samples, which involves releasement of iron content from biological entities using hydrochloric acid and KMnO_4 as well as reduction of ferric iron into ferrous iron using ascorbic acid, prior to the application of ferrozine [58]. As a fast, cheap and reliable test, it is widely applied in recent studies of iron oxide nanoparticles administered into biological systems [59].

1.7.3 Atomic absorption spectroscopy

Atomic absorption spectroscopy (AAS) is a spectroanalytical procedure for the quantitative determination of chemical elements employing the absorption of optical radiation (light) by free atoms in the gaseous state [60]. This technique is commonly used in analytical chemistry for determining the concentration of a particular element in the sample to be analyzed. AAS can determine over 70 different elements in solution or directly in solid samples with high sensitivity (>0.1 ppm). It has been used for quantifying iron oxide nanoparticles at an analytical level [61]. However, access to AAS is usually expensive, and therefore less available for some laboratories.

1.7.4 Quantitative susceptibility mapping (QSM)

In addition to intrinsic iron content, magnetite nanoparticles can also be characterized by their magnetic properties, such as susceptibility, which modify the local magnetic field experienced by spins. It has been of long-standing interest to quantify the susceptibility of superparamagnetic nanomaterials in clinical MRI. Quantitative susceptibility mapping (QSM) is a technique recently developed for estimating magnetic field shifts based on magnetic resonance phase images, allowing noninvasive quantification of magnetic materials *in vivo* [62]. From magnitude images of MRI, regions of constant magnetic properties are segmented and the magnetic field for each region with unit susceptibility is computed to form the system matrix. Pseudo inversion is then used to determine the susceptibility from the measured field maps. Besides exogenous magnetite nanoparticles [63], QSM has also been successfully applied for the quantitation of pathological brain deposition of iron [64-65].

1.8 Engineering molecules of interest using yeast surface display

The quality and controllability of biomimetics are tightly related with the design of functional molecules, namely how similar or superior they are compared to their physiological counterparts. This process can greatly benefit from protein engineering either through rational design or directed evolution. The yeast surface display (YSD) technique was first published by Dane Wittrup, where a protein of interest is displayed as a fusion to the Aga2p protein on the surface of yeast [66]. As such, high affinity protein ligands can be easily enriched through magnetic separation and quantified by flow cytometry. In addition to activating mutein of LFA-1 I domain [39], we have also discovered an activation-specific antibody against Mac-1 from

combinatorial libraries using YSD [67]. In most biological systems, regulation of one single response requires the coordination of multiple independent molecular interactions. Due to such complexity, it would be sensible to engineer more molecules specific to the allostery of interest, and equip biomimetics with more than one distinct receptor-ligand pair, so as to achieve higher specificity and efficacy of treatment.

1.9 Organization of the dissertation

The objective of the studies documented here is to establish a nanoparticle platform mimicking inflamed leukocytes using an engineered physiological ligand as the targeting moiety, translate it into clinical imaging modalities and provide quantitative diagnostic information about inflammatory diseases at the molecular level. An overview of the chapters and appendix are given below.

Chapter 1: Introduction. This chapter provides the background on current studies of nanoparticle-based biomimetics (particularly biomimetics of leukocytes), their applications in biomedical imaging, and present knowledge that informs our work (especially our preliminary studies on protein engineering, nanoparticle design and analysis tools for biodistribution), as well as an introduction to the overall content of this dissertation.

Chapter 2: Inflamed leukocyte-mimetic nanoparticles for molecular imaging of inflammation. In this chapter, we will first talk about the design of the inflamed leukocyte-mimetic nanoparticles (LMN). In order to incorporate inflammation-sensitive molecular interactions, super paramagnetic iron oxide (SPIO) nanocrystals are conjugated with integrin lymphocyte function-associated antigen (LFA)-1 I

domain, engineered to mimic activated leukocytes in physiology. Then we will characterize its physical properties (size, stability, functionality and specificity) through a series of *in vitro* assays, confirming its preferential binding to unregulated levels of ICAM-1. Aided with whole-body fluorescence imaging and MRI, we will demonstrate LMN detecting inflammatory response in a spatial-temporal manner *in vivo*, using three different models of inflammatory diseases (tumor xenograft, subcutaneous acute inflammation, and systemic acute inflammation).

Chapter 3: Visualizing and quantifying acute inflammation using ICAM-1 specific nanoparticles and MRI quantitative susceptibility mapping. In this chapter, we will explore the translation of LMN into molecular diagnosis of systemic inflammatory response syndrome (SIRS) using mouse models. Specifically, we will verify the validity and accuracy of LMN-aided MRI with prudent examination, including extensive comparison of the quantitation of organ-specific distributions of nanoparticles through quantitative susceptibility mapping (QSM) and radioactivity measurement.

Chapter 4: Novel strategy for selection of monoclonal antibodies against highly conserved antigens: phage library panning against ephrin-B2 displayed on yeast. In this chapter, we will discuss how we can combine yeast surface display and phage display, so as to successfully select monoclonal antibodies against ephrin-B2, one highly conserved human antigen that plays important roles during tumor angiogenesis.

Chapter 5: Conclusions and future directions. This chapter provides a summary for this thesis project. It also includes data and ideas supporting future work, such as

how we can improve LMN as a biomimetic; how we can extend it to diagnosing other inflammatory diseases such as strokes; how we can make LMN more versatile so that eventually it is able to target cancer where more implications besides inflammation exist.

Appendix A: Yeast surface two-hybrid for quantitative *in vivo* detection of protein-protein interactions via the secretory pathway. This part describes one co-author project in which we developed a yeast surface two-hybrid (YS2H) system based on the original YSD platform, enabling quantitative measurement of pairwise protein interactions via the secretory pathway by expressing one protein (bait) anchored to the cell wall and the other (prey) in soluble form.

Appendix B: Cell surface assembly of HIV gp41 six helix bundles for facile, quantitative measurements of hetero-oligomeric interactions. This part describes one co-author project in which we reconstituted the six helix bundle (6HB) complex of HIV gp41 on the yeast surface, quantitatively measured the equilibrium and kinetic constants of soluble 6HB, and delineated the residues influencing homo-oligomeric and hetero-oligomeric coiled-coil interactions.

REFERENCES

- [1] Gupta AK, Gupta M. Synthesis and surface engineering of iron oxide nanoparticles for biomedical applications. *Biomaterials*. 2005;26:3995-4021.
- [2] Alivisatos AP. Semiconductor clusters, nanocrystals, and quantum dots. *Science*. 1996;271:933-7.
- [3] Daniel MC, Astruc D. Gold nanoparticles: Assembly, supramolecular chemistry, quantum-size-related properties, and applications toward biology, catalysis, and nanotechnology. *Chemical Reviews*. 2004;104:293-346.
- [4] Cliffl DE, Turner BN, Huffman BJ. Nanoparticle-based biologic mimetics. *Wires Nanomed Nanobi*. 2009;1:47-59.
- [5] Brust M, Walker M, Bethell D, Schiffrin DJ, Whyman R. Synthesis of thiol-derivatized gold nanoparticles in a two-phase liquid-liquid system. *Chem Commun*. 1994;7:801-902.
- [6] Almeida JPM, Chen AL, Foster A, Drezek R. In vivo biodistribution of nanoparticles. *Nanomedicine-Uk*. 2011;6:815-35.
- [7] Choi HS, Liu W, Misra P, Tanaka E, Zimmer JP, Itty Ipe B, et al. Renal clearance of quantum dots. *Nat Biotechnol*. 2007;25:1165-70.
- [8] Gaur U, Sahoo SK, De TK, Ghosh PC, Maitra A, Ghosh PK. Biodistribution of fluoresceinated dextran using novel nanoparticles evading reticuloendothelial system. *Int J Pharm*. 2000;202:1-10.
- [9] Saha RN, Vasanthakumar S, Bende G, Snehalatha M. Nanoparticulate drug delivery systems for cancer chemotherapy. *Mol Membr Biol*. 2010;27:215-31.
- [10] Alexis F, Pridgen E, Molnar LK, Farokhzad OC. Factors affecting the clearance and biodistribution of polymeric nanoparticles. *Mol Pharm*. 2008;5:505-15.

- [11] Sperling RA, Casals E, Comenge J, Bastus NG, Puentes VF. Inorganic Engineered Nanoparticles and Their Impact on the Immune Response. *Curr Drug Metab.* 2009;10:895-904.
- [12] Chen N, He Y, Su YY, Li XM, Huang Q, Wang HF, et al. The cytotoxicity of cadmium-based quantum dots. *Biomaterials.* 2012;33:1238-44.
- [13] Soenen SJH, De Cuyper M. Assessing iron oxide nanoparticle toxicity in vitro: current status and future prospects. *Nanomedicine-Uk.* 2010;5:1261-75.
- [14] Khlebtsov N, Dykman L. Biodistribution and toxicity of engineered gold nanoparticles: a review of in vitro and in vivo studies. *Chem Soc Rev.* 2011;40:1647-71.
- [15] Bevilacqua MP, Pober JS, Mendrick DL, Cotran RS, Gimbrone MA, Jr. Identification of an inducible endothelial-leukocyte adhesion molecule. *Proc Natl Acad Sci U S A.* 1987;84:9238-42.
- [16] Geng JG, Bevilacqua MP, Moore KL, McIntyre TM, Prescott SM, Kim JM, et al. Rapid neutrophil adhesion to activated endothelium mediated by GMP-140. *Nature.* 1990;343:757-60.
- [17] Diamond MS, Staunton DE, de Fougerolles AR, Stacker SA, Garcia-Aguilar J, Hibbs ML, et al. ICAM-1 (CD54): a counter-receptor for Mac-1 (CD11b/CD18). *J Cell Biol.* 1990;111:3129-39.
- [18] Marlin SD, Springer TA. Purified intercellular adhesion molecule-1 (ICAM-1) is a ligand for lymphocyte function-associated antigen 1 (LFA-1). *Cell.* 1987;51:813-9.
- [19] Elices MJ, Osborn L, Takada Y, Crouse C, Luhowskyj S, Hemler ME, et al. VCAM-1 on activated endothelium interacts with the leukocyte integrin VLA-4 at a site distinct from the VLA-4/fibronectin binding site. *Cell.* 1990;60:577-84.

- [20] Dustin ML, Springer TA. T-Cell Receptor Cross-Linking Transiently Stimulates Adhesiveness through Lfa-1. *Nature*. 1989;341:619-24.
- [21] Springer T, Galfre G, Secher DS, Milstein C. Mac-1: a macrophage differentiation antigen identified by monoclonal antibody. *Eur J Immunol*. 1979;9:301-6.
- [22] Bevilacqua MP. Endothelial-leukocyte adhesion molecules. *Annu Rev Immunol*. 1993;11:767-804.
- [23] Stad RK, Buurman WA. Current Views on Structure and Function of Endothelial Adhesion Molecules. *Cell Adhes Commun*. 1994;2:261-8.
- [24] Takagi J, Springer TA. Integrin activation and structural rearrangement. *Immunol Rev*. 2002;186:141-63.
- [25] Steeber DA, Campbell MA, Basit A, Ley K, Tedder TF. Optimal selectin-mediated rolling of leukocytes during inflammation in vivo requires intercellular adhesion molecule-1 expression. *Proc Natl Acad Sci U S A*. 1998;95:7562-7.
- [26] Simon SI, Hu Y, Vestweber D, Smith CW. Neutrophil tethering on E-selectin activates beta(2) integrin binding to ICAM-1 through a mitogen-activated protein kinase signal transduction pathway. *J Immunol*. 2000;164:4348-58.
- [27] Sakhalkar HS, Dalal MK, Salem AK, Ansari R, Fu J, Kiani MF, et al. Leukocyte-inspired biodegradable particles that selectively and avidly adhere to inflamed endothelium in vitro and in vivo. *Proc Natl Acad Sci U S A*. 2003;100:15895-900.
- [28] Hammer DA, Robbins GP, Haun JB, Lin JJ, Qi W, Smith LA, et al. Leukopolymersomes. *Faraday Discuss*. 2008;139:129-41; discussion 213-28, 419-20.
- [29] Eniola AO, Willcox PJ, Hammer DA. Interplay between rolling and firm adhesion elucidated with a cell-free system engineered with two distinct receptor-ligand pairs. *Biophys J*. 2003;85:2720-31.

- [30] Omolola Eniola A, Hammer DA. In vitro characterization of leukocyte mimetic for targeting therapeutics to the endothelium using two receptors. *Biomaterials*. 2005;26:7136-44.
- [31] Lindner JR, Song J, Christiansen J, Klibanov AL, Xu F, Ley K. Ultrasound assessment of inflammation and renal tissue injury with microbubbles targeted to P-selectin. *Circulation*. 2001;104:2107-12.
- [32] Weller GER, Lu E, Csikari MM, Klibanov AL, Fischer D, Wagner WR, et al. Ultrasound Imaging of acute cardiac transplant rejection with microbubbles targeted to intercellular adhesion molecule-1. *Circulation*. 2003;108:218-24.
- [33] Reinhardt M, Hauff P, Linker RA, Briel A, Gold R, Rieckmann P, et al. Ultrasound derived imaging and quantification of cell adhesion molecules in experimental autoimmune encephalomyelitis (EAE) by Sensitive Particle Acoustic Quantification (SPAQ). *Neuroimage*. 2005;27:267-78.
- [34] Sipkins DA, Gijbels K, Tropper FD, Bednarski M, Li KCP, Steinman L. ICAM-1 expression in autoimmune encephalitis visualized using magnetic resonance imaging. *Journal of Neuroimmunology*. 2000;104:1-9.
- [35] McAteer MA, Sibson NR, von zur Muhlen C, Schneider JE, Lowe AS, Warrick N, et al. In vivo magnetic resonance imaging of acute brain inflammation using microparticles of iron oxide. *Nat Med*. 2007;13:1253-8.
- [36] Boutry S, Laurent S, Elst LV, Muller RN. Specific E-selectin targeting with a superparamagnetic MRI contrast agent. *Contrast Media Mol Imaging*. 2006;1:15-22.
- [37] Rossin R, Muro S, Welch MJ, Muzykantov VR, Schuster DP. In vivo imaging of ⁶⁴Cu-labeled polymer nanoparticles targeted to the lung endothelium. *J Nucl Med*. 2008;49:103-11.
- [38] Carman CV, Springer TA. Integrin avidity regulation: are changes in affinity and conformation underemphasized? *Curr Opin Cell Biol*. 2003;15:547-56.

- [39] Jin M, Song G, Carman CV, Kim YS, Astrof NS, Shimaoka M, et al. Directed evolution to probe protein allostery and integrin I domains of 200,000-fold higher affinity. *Proc Natl Acad Sci U S A*. 2006;103:5758-63.
- [40] Li R, Rieu P, Griffith DL, Scott D, Arnaout MA. Two functional states of the CD11b A-domain: correlations with key features of two Mn²⁺-complexed crystal structures. *J Cell Biol*. 1998;143:1523-34.
- [41] Shimaoka M, Lu C, Palframan RT, von Andrian UH, McCormack A, Takagi J, et al. Reversibly locking a protein fold in an active conformation with a disulfide bond: integrin alphaL I domains with high affinity and antagonist activity in vivo. *Proc Natl Acad Sci U S A*. 2001;98:6009-14.
- [42] McCleverty CJ, Liddington RC. Engineered allosteric mutants of the integrin alphaMbeta2 I domain: structural and functional studies. *Biochem J*. 2003;372:121-7.
- [43] Pankhurst QA, Connolly J, Jones SK, Dobson J. Applications of magnetic nanoparticles in biomedicine. *J Phys D Appl Phys*. 2003;36:R167-R81.
- [44] Sun S, Zeng H. Size-controlled synthesis of magnetite nanoparticles. *J Am Chem Soc*. 2002;124:8204-5.
- [45] Molday RS, Mackenzie D. Immunospecific Ferromagnetic Iron-Dextran Reagents for the Labeling and Magnetic Separation of Cells. *J Immunol Methods*. 1982;52:353-67.
- [46] Senyei A, Widder K, Czerlinski G. Magnetic Guidance of Drug-Carrying Microspheres. *J Appl Phys*. 1978;49:3578-83.
- [47] Rand RW, Mosso JA. Ferromagnetic silicone vascular occlusion in a superconducting magnetic field. Preliminary report. *Bull Los Angeles Neurol Soc*. 1972;37:67-74.

- [48] Weissleder R, Elizondo G, Wittenberg J, Rabito CA, Bengele HH, Josephson L. Ultrasmall superparamagnetic iron oxide: characterization of a new class of contrast agents for MR imaging. *Radiology*. 1990;175:489-93.
- [49] Dubertret B, Skourides P, Norris DJ, Noireaux V, Brivanlou AH, Libchaber A. In vivo imaging of quantum dots encapsulated in phospholipid micelles. *Science*. 2002;298:1759-62.
- [50] Johnsson M, Hansson P, Edwards K. Spherical micelles and other self-assembled structures in dilute aqueous mixtures of poly(ethylene glycol) lipids. *Journal of Physical Chemistry B*. 2001;105:8420-30.
- [51] Torchilin VP. PEG-based micelles as carriers of contrast agents for different imaging modalities. *Adv Drug Deliver Rev*. 2002;54:235-52.
- [52] Schmitt J, Hess H, Stunnenberg HG. Affinity purification of histidine-tagged proteins. *Mol Biol Rep*. 1993;18:223-30.
- [53] Scheuer PJ, Williams R, Muir AR. Hepatic pathology in relatives of patients with haemochromatosis. *J Pathol Bacteriol*. 1962;84:53-64.
- [54] Astaldi G, Meardi G, Lisino T. The iron content of jejunal mucosa obtained by Crosby's biopsy in hemochromatosis and hemosiderosis. *Blood*. 1966;28:70-82.
- [55] Lacava LM, Garcia VAP, Kuckelhaus S, Azevedo RB, Sadeghiani N, Buske N, et al. Long-term retention of dextran-coated magnetite nanoparticles in the liver and spleen. *J Magn Magn Mater*. 2004;272:2434-5.
- [56] Ceriotti F, Ceriotti G. Improved Direct Specific Determination of Serum Iron and Total Iron-Binding-Capacity. *Clin Chem*. 1980;26:327-31.
- [57] Fish WW. Rapid Colorimetric Micromethod for the Quantitation of Complexed Iron in Biological Samples. *Method Enzymol*. 1988;158:357-64.

- [58] Riemer J, Hoepken HH, Czerwinska H, Robinson SR, Dringen R. Colorimetric ferrozine-based assay for the quantitation of iron in cultured cells. *Anal Biochem.* 2004;331:370-5.
- [59] Muller K, Skepper JN, Posfai M, Trivedi R, Howarth S, Corot C, et al. Effect of ultrasmall superparamagnetic iron oxide nanoparticles (Ferumoxtran-10) on human monocyte-macrophages in vitro. *Biomaterials.* 2007;28:1629-42.
- [60] Slavin W. Atomic absorption spectrometry. *Methods Enzymol.* 1988;158:117-45.
- [61] Jain TK, Morales MA, Sahoo SK, Leslie-Pelecky DL, Labhasetwar V. Iron oxide nanoparticles for sustained delivery of anticancer agents. *Mol Pharmaceut.* 2005;2:194-205.
- [62] de Rochefort L, Brown R, Prince MR, Wang Y. Quantitative MR susceptibility mapping using piece-wise constant regularized inversion of the magnetic field. *Magn Reson Med.* 2008;60:1003-9.
- [63] Liu TA, Spincemaille P, de Rochefort L, Wong R, Prince M, Wang Y. Unambiguous identification of superparamagnetic iron oxide particles through quantitative susceptibility mapping of the nonlinear response to magnetic fields. *Magn Reson Imaging.* 2010;28:1383-9.
- [64] Schweser F, Deistung A, Lehr BW, Reichenbach JR. Differentiation between diamagnetic and paramagnetic cerebral lesions based on magnetic susceptibility mapping. *Med Phys.* 2010;37:5165-78.
- [65] Bilgic B, Pfefferbaum A, Rohlfing T, Sullivan EV, Adalsteinsson E. MRI estimates of brain iron concentration in normal aging using quantitative susceptibility mapping. *Neuroimage.* 2012;59:2625-35.
- [66] Boder ET, Wittrup KD. Yeast surface display for screening combinatorial polypeptide libraries. *Nat Biotechnol.* 1997;15:553-7.

[67] Hu X, Kang S, Lefort C, Kim M, Jin MM. Combinatorial libraries against libraries for selecting neoepitope activation-specific antibodies. Proc Natl Acad Sci U S A. 2010;107:6252-7.

CHAPTER 2

INFLAMED LEUKOCYTE-MIMETIC NANOPARTICLES FOR MOLECULAR IMAGING OF INFLAMMATION

Published in *Biomaterials*¹

2.1 Abstract

Dysregulated host inflammatory response causes many diseases, including cardiovascular and neurodegenerative diseases, cancer, and sepsis. Sensitive detection of the site of inflammation will, therefore, produce a wide-ranging impact on disease diagnosis and treatment. We hypothesized that nanoprobe designed to mimic the molecular interactions occurring between inflamed leukocytes and endothelium may possess selectivity toward diverse host inflammatory responses. To incorporate inflammation-sensitive molecular interactions, super paramagnetic iron oxide nanoparticles were conjugated with integrin lymphocyte function-associated antigen (LFA)-1 I domain, engineered to mimic activated leukocytes in physiology. Whole body optical and magnetic resonance imaging *in vivo* revealed that leukocyte-mimetic nanoparticles localized preferentially to the vasculature within and in the invasive front of the tumor, as well as to the site of acute inflammation. This study explored *in vivo* detection of tumor-associated vasculature with systemically injected

¹ This chapter is modified with the permission of the publisher from Chen X, Wong R, Khalidov I, Wang AY, Leelawattanachai J, Wang Y, and Jin M. Inflamed leukocyte-mimetic nanoparticles for molecule imaging of inflammation. *Biomaterials* 2011;32(30):7651–7661. Xiaoyue Chen designed the study, conducted the experiments, analyzed the data and wrote the paper.

inflammation-specific nanoparticles, presenting a possibility of tumor detection by inflamed tumor microenvironment.

2.2 Introduction

Dysregulated inflammatory responses of the host are implicated in the pathogenesis of many human diseases [1]. Acute inflammation from infection can cause sepsis [2], while chronic inflammation, and continual coexistence between acute and chronic inflammation are associated with various neurodegenerative [3] and cardiovascular diseases [4], metabolic disorders [5], and cancer [6, 7]. Accordingly, sensitive and early detection of inflammation and site-specific delivery of anti-inflammatory agents will have a wide-ranging impact on the treatment of various inflammation-related diseases. Upon induction of inflammation, a set of adhesion molecules are upregulated in endothelium, with which immune cells interact using counter adhesion molecules such as integrins to adhere to endothelium and to initiate diapedesis. Many existing studies have investigated targeted nanoparticles for the detection and treatment of inflammation employing antibodies or peptides specific to adhesion molecules such as intercellular adhesion molecule (ICAM)-1 [8-10], vascular cell adhesion molecule (VCAM)-1 [11-13], selectins [14], and collagen [15], all of which display distinct spatiotemporal responses to inflammation. Among these molecules, ICAM-1 has caught a particular interest because of its highly inducible and localized expression upon inflammatory signals, serving as a marker for inflammation despite its constitutive low level expression [16, 17].

In this study, we developed nanomicelle encapsulating superparamagnetic iron oxide (SPIO) nanoparticles, designed for facile and robust conjugation with targeting moieties and *in vivo* detection by optical imaging and magnetic resonance imaging (MRI). In order to design nanoparticles to mimic the behavior of inflamed leukocytes in their ability to locate to the inflamed site, SPIO nanoparticle was coated with an optimum number of high affinity inserted (I) domain of integrin called lymphocyte function-associated antigen (LFA)-1 [18], a physiological receptor for ICAM-1. Leukocyte-mimetic nanoparticles were examined for detection of ICAM-1 overexpression in tumor cells, tumor vascular microenvironment, and acute inflammation *in vivo*. With our recently developed MRI technique for quantitative mapping of contrast agent [19, 20], we explored the possibility of quantitative spatiotemporal mapping of iron oxide distribution *in vivo* using a mouse model of acute inflammation.

2.3 Materials and methods

2.3.1 Preparation and characterization of protein coated SPIO nanomicelles

Oleic acid-capped super paramagnetic iron oxide (SPIO) nanocrystals (Ocean Nanotech, LLC) in 5 mg were suspended in 1 ml chloroform with 12 mg 1,2-dipalmitoyl-sn-glycero-3-phosphoethanolamine-N-[methoxy(polyethylene glycol)-2000] (DPPE-PEG) and 3 mg 1,2-dioleoyl-sn-glycero-3-[(N-(5-amino-1-carboxypentyl)-iminodiacetic acid)succinyl] nickel salt (DOGS-NTA) (Avanti Polar Lipids, Inc.). For radiolabeled nanoparticles, 60 μCi of L- α -Dipalmitoyl-Phosphatidylcholine, [Choline-Methyl- ^3H] (Perkin Elmer) was also added at this step.

After 10 min sonication and overnight desiccation, 1 ml of water was added to the residue to form a micelle layer on SPIO. After another 10 min sonication and filtration through 0.22 μm filters (Millipore), optically clear suspension containing SPIO micelles were obtained. Empty micelles without SPIO in the core were removed by ultracentrifugation. SPIO nanoparticles were purified and resuspended in pH 7.4 phosphate-buffered saline (PBS) by size exclusion S200 column (GE Healthcare). The wild-type (wt), D137A, and F265S/F292G mutants of LFA-1 I domains fused to His tag (6 histidine residues) at the N-terminal were produced as previously described [17]. Conjugation of SPIO with His tagged I domains was obtained by incubation at 4 $^{\circ}\text{C}$ overnight. Free proteins were removed by size exclusion. All fluorescently labeled SPIO nanoparticles were prepared by covalently conjugating Alexa Fluor (AF) succinimidyl esters (Invitrogen) to the I domains. Conjugation of fluorescence dyes to the proteins rather than to phospholipid was chosen due to significant fluorescence quenching between iron oxide and AF-phospholipids. The coating density of proteins on SPIO was determined from the ratio of SPIO amount ($\text{OD}_{600\text{nm}} 1 = 0.42 \text{ mg/ml}$) and the concentration of the proteins bound to SPIO (by Lowry's method). Specific activities of radiolabeled SPIO were measured by scintillation counter (Beckman Coulter LS6500). Dynamic light scattering (DLS, Malvern Instruments) was used to measure the average hydrodynamic size of SPIO after assembly and protein conjugation. Transmission electron microscopy (TEM; FEI Tecnai) images of SPIO were also taken before and after protein conjugation. 1% uranyl acetate was used for protein staining.

2.3.2 Cell culture

All mammalian cells used in this study were cultured in Advanced Dulbecco's modified Eagle's medium containing 10% (v/v) fetal bovine serum and 2 mM L-glutamine (Invitrogen) at 37 °C in a 5% CO₂ humidified incubator. For induction of inflammation, bEnd.3 (ATCC) cells were treated with 1 µg/ml of LPS (*Escherichia coli* 026:B6, Sigma) for 12 h. HeLa and 293T cells stably expressing GFP were established using pSMPUW-miR-GFP/Puro Lentiviral Expression Vector system (Cell Biolabs).

2.3.3 Immunofluorescence flow cytometry

Cells were trypsinized and washed once with the ice-chilled labeling buffer (pH 7.4 PBS, 1% (w/v) BSA, 1 mM MgCl₂). 100,000 cells were incubated in 100 µl of the labeling buffer for 30 min on ice with 10 µg/ml of Alexa Fluor labeled proteins or SPIO conjugated with the same amount of proteins. For competition assay, 50 µg/ml of unlabeled proteins were included in the labeling buffer during incubation. Cells were washed twice and resuspended in 300 µl of the labeling buffer and subjected to flow cytometer (Beckman Coulter EPICS XL-MC).

2.3.4 Microscopy visualization of cell labeling in vitro

For immunofluorescence microscopy detection of protein labeling, cells were plated, washed in pH 7.4 PBS, and fixed with 4% paraformaldehyde for 15 min. After washing three times, cells were incubated with 10 µg/ml of Alexa Fluor labeled proteins in PBS/Triton (pH 7.4 PBS, 0.3% (v/v) Triton X-100, 1 mM MgCl₂) at room temperature for 1 h. Cells were rinsed once with pH 7.4 PBS and twice with high salt PBS (pH 7.4 PBS, 0.4 M NaCl, 1 mM MgCl₂). 300 nM DAPI (4',6-diamidino-2-phenylindole, Invitrogen) in PBS was then added and incubated for 10 min for nucleus

staining. Stained cells were washed and imaged with a confocal microscope (Zeiss LSM710). For detection of SPIO labeling, HeLa cells were plated and incubated with 50 µg/ml of SPIO coated with Alexa Fluor 488 conjugated proteins in culture media for 2 h at 37 °C. Cells were washed in pH 7.4 PBS, incubated for 1 h in serum-free medium for chasing, and imaged using confocal microscopy (Leica TCS SP2). After fluorescence imaging, cells were then prepared for Perls' Prussian blue staining for iron detection. Labeled cells were fixed with 4% paraformaldehyde, followed by incubation in a freshly prepared solution of 2% potassium ferrocyanide in 2% HCl for 20 min and counterstaining with 1% neutral red.

2.3.5 Magnetic cell labeling and quantification

Trypsinized cells were incubated for 4 h at 37 °C in the labeling buffer (PBS, 1mM MgCl₂) under constant rotating with different concentrations of radiolabeled SPIO, washed and then fixed in 4% paraformaldehyde. Cells were divided into two conditions, half of which were used for radioactivity measurement using scintillation counter (Beckman Coulter LS6500), while the remaining half for MRI scanning and QSM measurement after imbedding in 100 µl 2% agarose block. MR imaging of the magnetically labeled cells were performed on a 3T MRI scanner (Signa, GE, Milwaukee, WI). A 3D multi-echo gradient sequence was used to sample multiple TEs in one TR. Imaging parameters were as follows: TEs 3.696 ms, 4.196 ms, 5.696 ms, 11.696 ms, 35.696 ms; TR 40 ms; flip angle 30 °; matrix size 256×64×64; voxel size 500 µm³ isotropic. A 3D Fourier transform was applied to the raw k-space data to reconstruct T2* weighted images. QSM was obtained through Multiple Orientation Sampling (COSMOS) technique, as previously described [19].

2.3.6 Subcutaneous tumor model

3×10^6 human cervical cancer HeLa cells and human embryonic kidney 293T cells stably expressing GFP mixed in Matrigel (BD) were injected bilaterally into the front lower flank areas of 8-wk-old female nude mice. Mice were used for experiments 16-20 days after injection when tumor size reached about 300 mm^3 . All animal experiments were conducted in compliance with the regulations defined by the Institutional Laboratory Animal Use and Care Committee of Cornell University.

2.3.7 Acute LPS-inflammation model

For subcutaneous LPS, 1 mg/ml LPS in 100 μl PBS and 100 ml PBS were injected bilaterally into the lower flank areas of 8-wk-old female BALB/c mice. For systemic LPS, 1 mg/ml LPS in 100 μl PBS were injected into 8-wk-old female BALB/c mice. Prior to imaging hair was removed to reduce background fluorescence.

2.3.8 Near-IR optical imaging of mice

Animals were anesthetized with isoflurane mixed with oxygen at 5% and maintained at 2% isoflurane during whole body imaging (Olympus, OV100). Mice were administered with SPIO coated with AF750-conjugated proteins in 150 μl PBS via retro-orbital injection. 500 and 100 μg of SPIO were used for tumor imaging and acute inflammation models, respectively. Near-IR images were taken at different time points post-injection of SPIO. Tumor growth was detected by imaging green fluorescence. Image analysis was performed with Matlab R2007a (MathWorks).

2.3.9 MR imaging of mice with acute inflammation

For subcutaneous LPS model, prior to nanoparticle injection mice were exposed to LPS/PBS for 12 h. At 4 h after injection of SPIO in 150 μl PBS, mice were

ethanized by intraperitoneal injection of 2.5% tribromoethanol (20 $\mu\text{l/g}$), transcardially perfused with PBS, and fixed in paraformaldehyde. Prepared mice were scanned on a 7T scanner (Bruker BioSpin, Biospec 70/30 USR) with 3D FLASH sequence. Imaging parameters were as follows: TEs (echo time) 5 ms, 6 ms, 30 ms, 35 ms; TR (repetition time) 35 ms; excitation pulse angle 15 $^{\circ}$; matrix size 150 \times 150 \times 100; voxel size 200 μm^3 isotropic; NEX 1. A 3D Fourier transform was applied to the raw k-space data to reconstruct the images [19]. For systemic LPS model, prior to nanoparticle injection mice were exposed to LPS for 12 h. At 1, 8, and 25 h post-injection of SPIO coated with proteins in 150 μl PBS, mice were euthanized likewise. Prepared mice were scanned on a 3T scanner (GE Signa Excite) with 3D multi-echo EFGRE sequence [19]. Imaging parameters were as follows: TEs 3.696 ms, 4.196 ms, 5.696 ms, 11.696 ms, 35.696 ms; TR 40 ms; flip angle 30 $^{\circ}$; matrix size 256 \times 64 \times 64; voxel size 500 μm^3 isotropic. QSMs were reconstructed using the COSMOS technique, as previously described.

2.3.10 Histology

Tumor and normal tissues were collected from tumor bearing mice before or at the end of *in vivo* imaging experiments. 10 μm frozen tissue sections were sliced, fixed in paraformaldehyde, and stained with hematoxylin and eosin (H&E) or in Perls' Prussian blue. Images of the tissue sections were acquired by scanscope (Aperio). For immunofluorescence, antibodies used include rat anti-mouse CD31 (BD, MEC13.3) and goat anti-rat IgG labeled with AF350 (Invitrogen). Six different fields of view containing CD31 staining for each sample were counted using 25 Chalkley's random point method over an area of 0.16 mm^2 for vascularity analysis (Figure 2.10b). To

quantify the level of staining, three different regions of interest (ROI) with 0.50 mm² area were sampled for each condition in immunofluorescence staining (Figure 2.10a) and four ROI with 0.04 mm² area in each Prussian blue staining (Figure 2.14). Specific colors (blue for endothelium and Prussian blue, red for F265S/F292G) were extracted and intensities were measured using Image-Pro Plus 6.0 (Media Cybernetics) and ImageJ 1.41 (NIH).

2.3.11 Statistical analysis

Data were expressed as mean ± standard deviation of no smaller than triplicates, and analyzed for statistical significance using GraphPad Prism 5 (Graphpad Software). Linear regression was used to examine the correlation between SPIO measurements by radioactivity and QSM (Figure 2.7). One-way ANOVA was used to compare the staining and vascularity levels between different tissues, followed by Tukey's post-hoc test to determine statistical significance (Figure 2.10). Two-way ANOVA was used to compare the mean responses of different nanoparticles to different time points or to different tumors, followed by Bonferroni post-hoc test to determine statistical significance (Figure 2.13, 2.14, 2.16, 2.17 & 2.18).

2.4 Results

2.4.1 Synthesis and characterization of leukocyte-mimetic nanoparticles

Selective binding of SPIO nanoparticles to overexpressed ICAM-1 was conferred by surface coating at an optimal density (~100 molecular/particle) with the I domain of LFA-1 integrin, engineered for high affinity by mutations of F265S/F292G (denoted as F265S/F292G, $K_D = 6$ nM) [18]. Among physiological ligands for LFA-1

such as ICAMs and junctional adhesion molecule (JAM)-1 [21], ICAM-1 is most important in the setting of leukocyte adhesion to inflamed endothelium due to its highest affinity to LFA-1 [22], being highly inducible over basal low level expression, and localized expression upon inflammatory signals [16, 23]. In order to fine-tune coating density of F265S/F292G and present targeting moiety in a most functional orientation, oleic acid capped SPIO nanocrystals (Ocean Nanotech) were encapsulated with a layer of phospholipid consisting of 80% n-poly(ethylene glycol) phosphatidylethanolamine (DPPE-PEG) and 20% dioleoyl-glycero-succinyl-nitrilotriacetic acid (DOGS-NTA) (Figure 2.1). DOGS-NTA was used for non-covalent conjugation of targeting moieties with His tag in a robust and reproducible manner via high affinity binding to nickel ions chelated by NTA (Ni-NTA) [17, 24]. DPPE-PEG was included to maintain solubility, stability, and for its low immunogenicity and non-specific binding to cells and tissues *in vivo* [25]. Transmission electron microscope (TEM) images revealed monodispersed SPIO nanocrystals with an outer layer of micelle-like structure (Figure 2.2; dark ring density corresponds to uniformly distributed nickel ions (the black arrow in top right) and diffuse dark density to His-tagged proteins attached to Ni-NTA (the white arrow in bottom right)). Hydrodynamic size of SPIO with or without protein conjugation was measured to be 60 ± 10 nm by dynamic light scattering (DLS), an increase from 15 nm diameter SPIO core mainly due to the addition of phospholipid and PEG.

Prior to detecting ICAM-1 with nanoparticles, we first examined by immunofluorescence flow cytometry and fluorescence microscopy (Figure 2.3) soluble I domain (labeled with Alexa Fluor 488 (AF488), Invitrogen) binding to

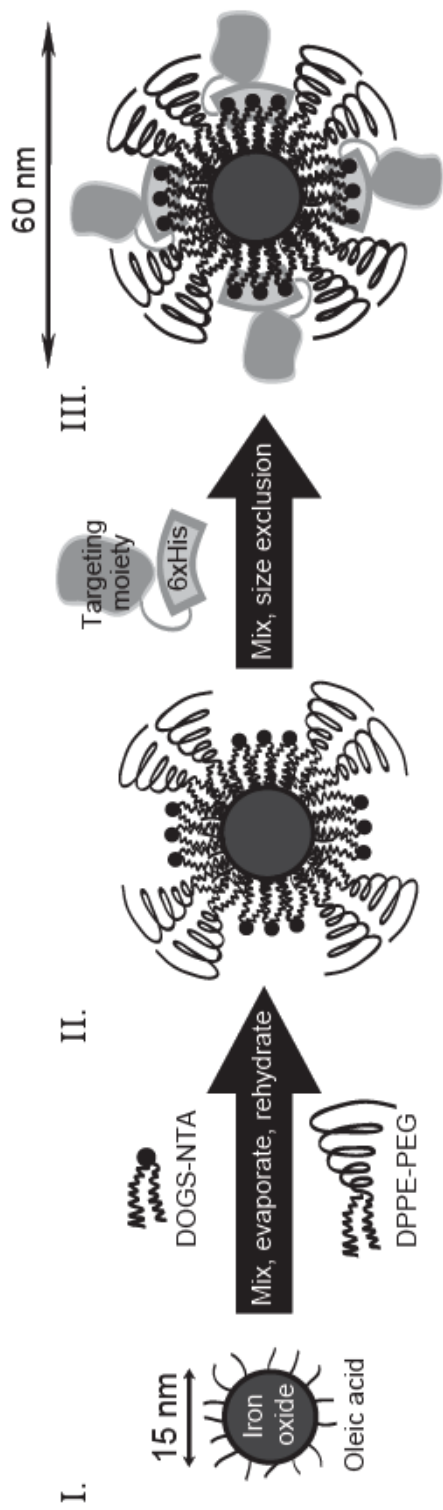


Figure 2.1: A schematic diagram of iron oxide nanocrystals encapsulated into a micelle-like layer composed of amphiphilic phospholipid copolymers (stage I–II) and subsequent protein conjugation for molecular targeting (stage III).

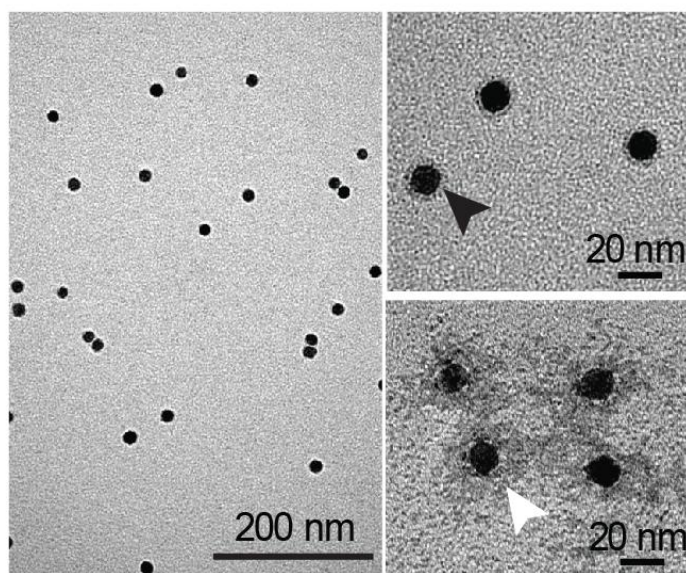


Figure 2.2: Uniformly sized, monodispersed SPIO with 15 nm core revealed by TEM. A close up view on top demonstrates a dark halo corresponding to nickel ions (black arrow) chelated by NTA groups surrounding SPIO. On the bottom is the negative staining of protein-conjugated SPIO with proteins and PEG groups darkly stained (white arrow), in contrast to a brighter phospholipid layer.

ICAM-1 expressed in monolayer culture of cervical cancer cells (HeLa). Specific binding to ICAM-1 was detected with the F265S/F292G, which was inhibited by unlabeled F265S/F292G. In contrast, no significant binding was observed with the wt I domain ($K_D = 1.7$ mM) [22] and the I domain containing a mutation of D137A [17], which disrupts the metal-ion dependent adhesion site (MIDAS) and abolishes ICAM-1 binding. The level of nanoparticle binding coated with the I domain variants was overall in good agreement with the soluble I domain binding, which varied in order from highest to lowest, F265S/F292G, wt, and D137A (Figure 2.4a). Markedly,

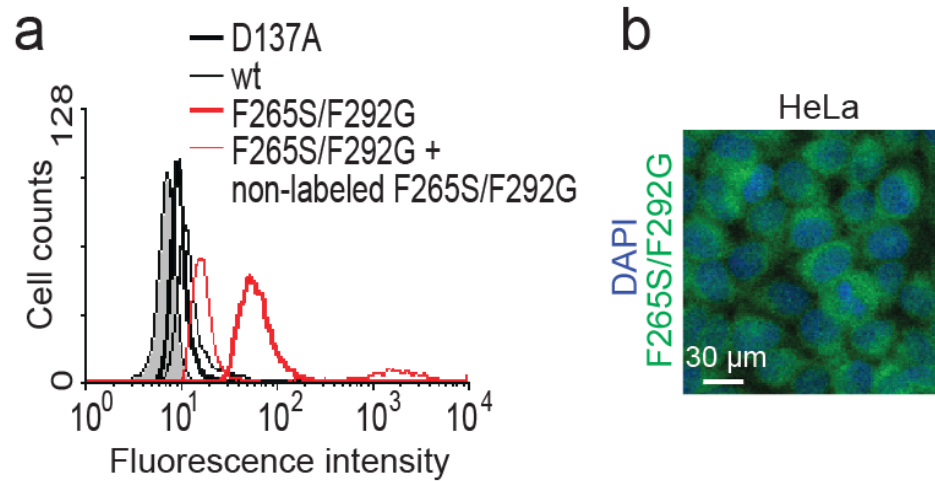


Figure 2.3: (a) Flow cytometry measurements of HeLa cells stained with different I domains (10 $\mu\text{g}/\text{ml}$) labeled with AF488. Non-stained HeLa cells are shown in grey shaded histograms. In a competition assay, non-labeled I domains were used at 50 $\mu\text{g}/\text{ml}$. (b) Shown in green is immunofluorescence staining of ICAM-1 in HeLa cells using F265S/F292G labeled with AF488. Nuclei staining by DAPI is shown in blue.

specific binding of SPIO conjugated with F265S/F292G (abbreviated as Leukocyte-Mimetic Nanoparticle or ‘LMN’) was not inhibited by competition with soluble I domain, presumably due to multivalent interaction between nanoparticles and HeLa cells. Enhanced binding due to avidity effect was also observed in the binding of nanoparticle coated with the wt I domain to HeLa, which resulted in greater binding than with the free wt I domain. ICAM-1-mediated binding of LMN but not with the nanoparticles coated with D137A (abbreviated as Non-Targeted Nanoparticle or ‘NTN’) led to significant cell surface labeling and internalization into the cells, evidenced by fluorescence microscopy and Perls’ Prussian blue staining (Figure 2.4b).

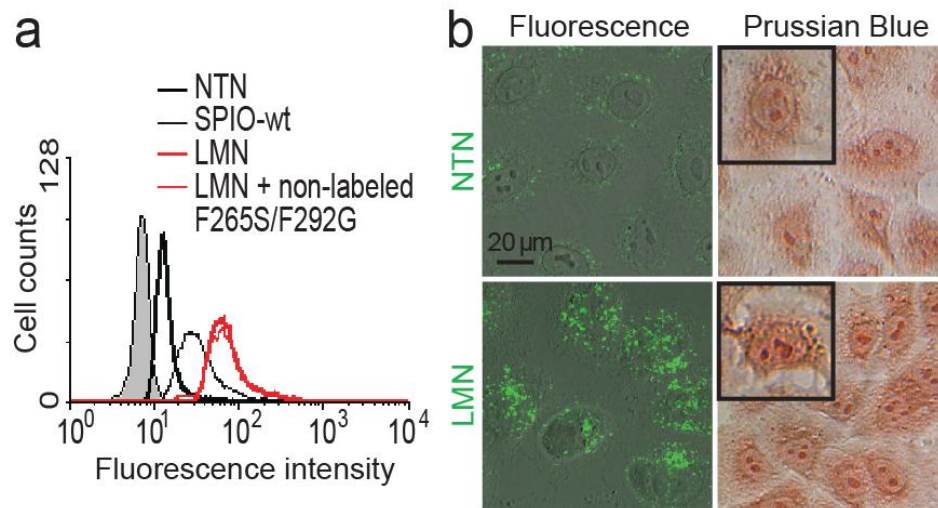


Figure 2.4: (a) Flow cytometry measurements of HeLa cells stained with nanoparticles (25 μ g/ml of SPIO and 10 μ g/ml of I domains) conjugated with different I domains. Non-labeled I domains as a competitor were used at 50 μ g/ml. (b) ICAM-1 dependent internalization of SPIO into HeLa cells was confirmed with confocal fluorescence microscopy (nanoparticles labeled with AF488) and Perls' Prussian blue staining.

2.4.2 Quantitative measurement of selective binding of LMN by MRI

SPIO nanoparticles are being used in clinics as T2* negative contrast agent for MRI. In order to validate SPIO as MRI contrast agent as well as to test the accuracy of our MRI technique for quantitative mapping of SPIO [19], 3 H-labeled phospholipid was additionally incorporated into the outer phospholipid layer of SPIO. When HeLa cells were incubated with LMN for 4 h at 37 $^{\circ}$ C, an increase in concentration led to an increase in cellular uptake of nanoparticles, reaching a plateau at 450 ng/ 10^6 cells (Figure 2.5). LMN delivery was specific to ICAM-1 expression, evidenced by little accumulation into HeLa with NTN and much lower delivery with LMN into 293T, a

cell line with no or little expression of ICAM-1. HeLa cells with known amount of internalized LMN by ^3H -radioisotope decay were then embedded into agarose and scanned with a MRI scanner. As expected, $T2^*$ showed a decrease in magnitudes with an increase in the amount of SPIO (Figure 2.6). With quantitative susceptibility mapping (QSM) algorithm was observed a close agreement with $\sim 30\%$ standard deviation from direct radioactivity measurements of free or intracellular SPIO, highlighting the ability of QSM in detecting as low as $1\ \mu\text{g}$ accumulation into $100\ \mu\text{l}$ in volume (Figure 2.7).

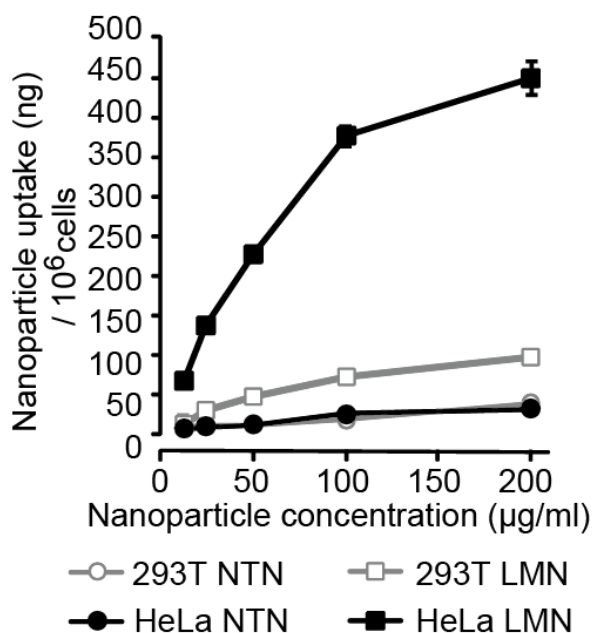


Figure 2.5: The amount of SPIO internalized into HeLa or 293T was measured by radioisotope measurement of ^3H -phospholipid incorporated into SPIO nanoparticles. SPIO nanoparticles were coated with either F265S/F292G (LMN) for ICAM-1 targeting or with D137A (NTN) as a control.

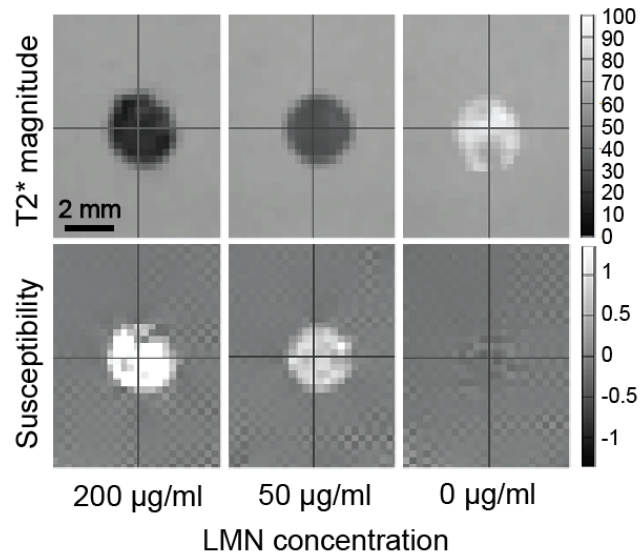


Figure 2.6: T2* and susceptibility images of agarose-embedded HeLa cells that were labeled with 200-0 $\mu\text{g/ml}$ of LMN.

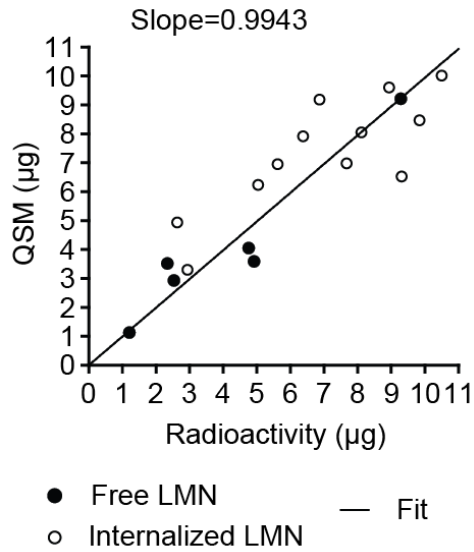


Figure 2.7: A comparison of iron mass estimated by QSM technique and radioisotope measurement. Shown are the measurements of agarose-embedded free LMN (closed circles) and LMN internalized into HeLa cells (closed circles).

2.4.3 *Ex vivo* detection of ICAM-1 induction in human tumor xenograft and in inflamed stroma

Not only is ICAM-1 upregulated in several carcinomas compared to respective normal epithelium, implicating active involvement of ICAM-1 in cancer development, its induction has also been observed in tumor vasculature caused by an inflamed network encompassing tumor and tumor microenvironment [26-28]. Previously, we have found that human LFA-1 I domain cross-reacted with murine ICAM-1 [17], which was recapitulated by the staining of ICAM-1 induced in murine brain endothelium (b.End3) after lipopolysaccharide (LPS) treatment (Figure 2.8). When

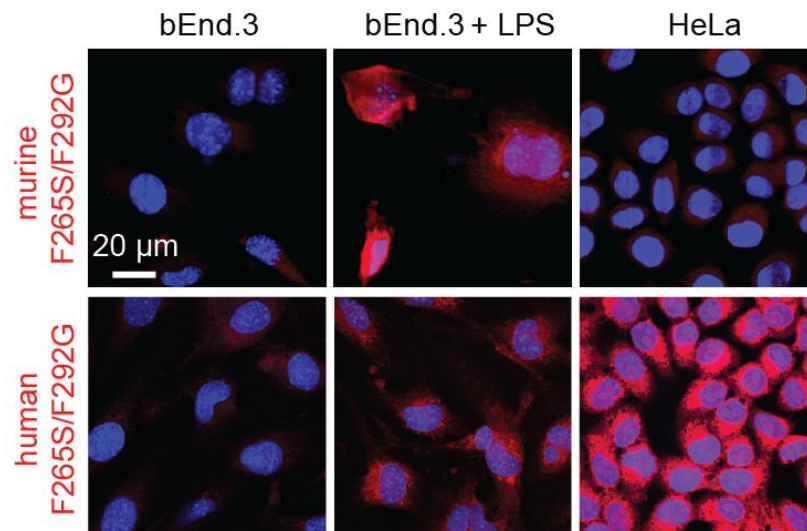


Figure 2.8: Confocal fluorescence images of murine b.End3 cells before and after LPS treatment and HeLa cells stained with murine (top) and human (bottom) I domains (F265S/F292G) labeled with AF594. Nuclei staining by DAPI is shown in blue.

tissue sections of GFP-expressing HeLa xenograft were analyzed for ICAM-1 detection by soluble F265S/F292G labeled with AF594 (Invitrogen), most of the GFP signal was overlapped with red fluorescence (Figure 2.9). Notably, we found that the

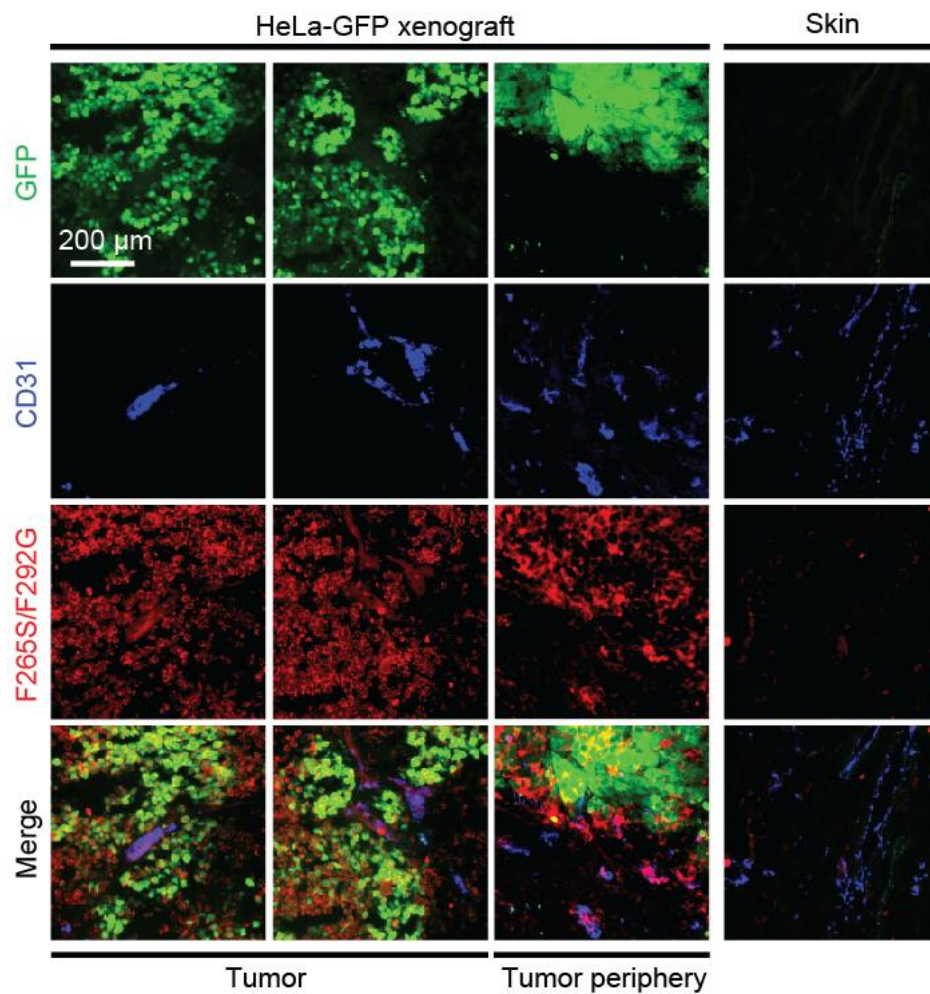


Figure 2.9: Immunofluorescence images of GFP-expressing HeLa xenograft tumor tissue costained with F265S/F292G-AF594 and anti-murine CD31 antibodies. Skin tissues from non-tumor bearing mice were used as control.

majority of endothelial cells (PECAM-1 (CD31) positive) within the tumor were also stained by F265S/F292G. In contrast, the level of ICAM-1 induction and colocalization with CD31 staining in the vasculature away from the tumor, such as those in the skin, was far lower, amounting to ~15% compared to 70% and 35% of the vasculature within the tumor and its periphery (defined as a region within 300 μm distance from the edge of tumor), respectively (Figure 2.9 & 2.10).

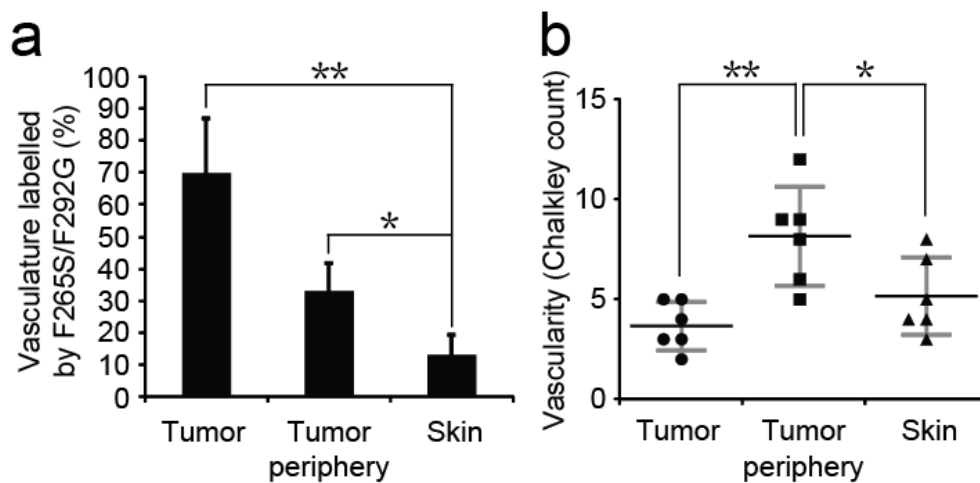


Figure 2.10: (a) The percentages of endothelium costained with CD31 and F265S/F292G within the tumor, in the periphery (300 μm from the tumor), and in the skin were determined from immunohistology (n = 6). (b) Vascularity within the tumor, in the periphery (300 μm from the tumor), and in the skin was quantified using Chalkley's method (25 random points per field of view) (n = 3; *p < 0.05, **p < 0.01).

2.4.4 In vivo detection of ICAM-1 induction in human tumor xenograft and in inflamed stroma

After confirming specific detection of ICAM-1 in *ex vivo* tumor slice by free F265S/F292G, we then examined if systemically delivered nanoparticles would accumulate to the tumor and inflamed stroma by ICAM-1 targeting. To validate that nanoparticle localization is ICAM-1 specific and not due to an increased permeability of the tumor vasculature, NTN and ICAM-1 negative 293T cell xenograft were used as controls. The growth of HeLa and 293T xenograft in mice was confirmed by whole body imaging of GFP (Figure 2.11a). At 50 h after intravenous injection of

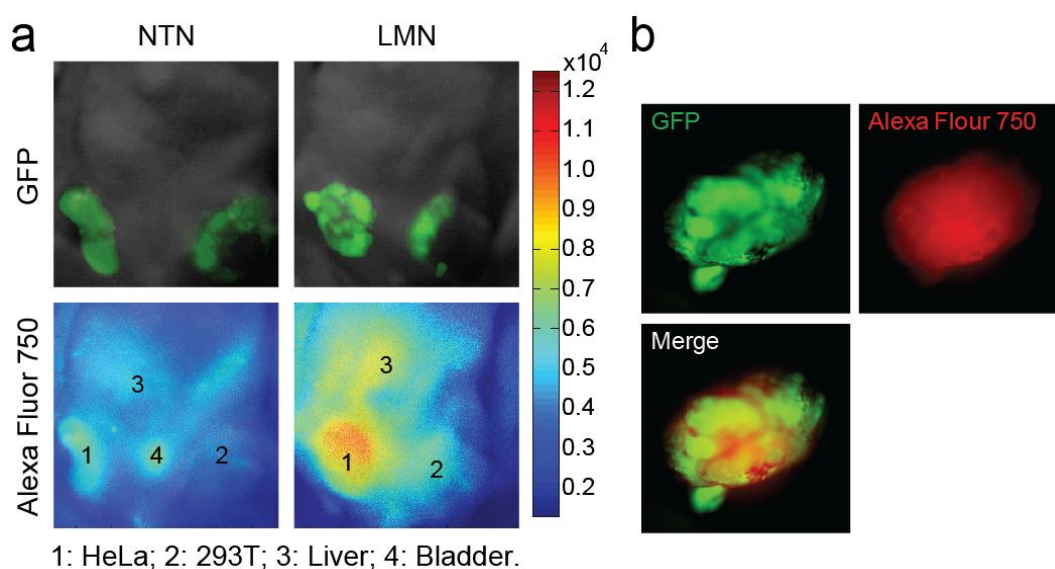


Figure 2.11: *In vivo* near-IR imaging of mice at 50 h after intravenous injection of NTN vs. LMN. GFP indicates the growth of HeLa ('1') and 293T ('2') tumors.

nanoparticles, whole body imaging of near-infrared (near-IR) fluorescence (AF750 attached to the I domains) indicated accumulation of LMN into HeLa but much less into 293T xenograft (Figure 2.11). Subsequent *ex vivo* imaging of the tumor and the

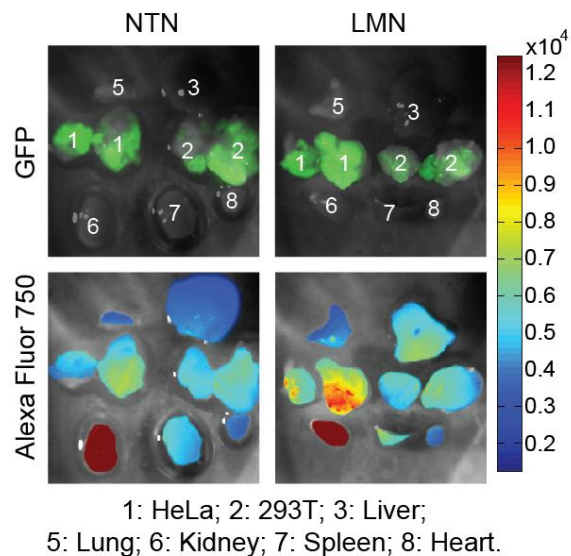


Figure 2.12: *Ex vivo* near-IR imaging of mice at 50 h after intravenous injection of NTN vs. LMN. GFP indicates the growth of HeLa ('1') and 293T ('2') tumors. The distribution of nanoparticles into the major organs ('3'-'8') were also examined.

major organs harvested from the mice further confirmed a greater level of delivery into HeLa xenograft with LMN (Figure 2.12). The signal from the kidney was by far greater than those from other organs both for LMN and NTN, indicating ICAM-1 independent clearance through the kidney (Figure 2.12). Interestingly, higher fluorescence was also detected in the liver with LMN, presumably caused by persistent, low-level inflammation in the liver. Whole body imaging of nanoparticles localized to HeLa and 293T xenograft over the time course of 30 min to 50 h post-injection showed that the peak accumulation occurred at 1-3 h post-injection, followed by a gradual decrease over 3 days and a complete clearance by 7 days (Figure 2.13). The presence of LMN into HeLa was also confirmed by direct staining of iron with

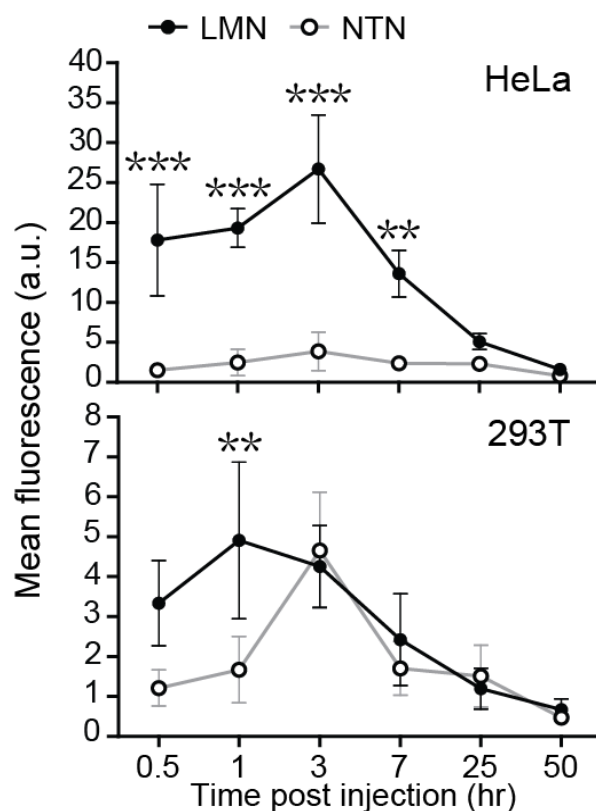


Figure 2.13: Near-IR fluorescence intensities of HeLa and 293T tumors at different time points after intravenous injection of LMN vs. NTN (n = 4; **P < 0.01, ***p < 0.001).

Prussian blue (Figure 2.14). To map the distribution of LMN by fluorescence microscopy, SPIO nanoparticles conjugated with AF594-labeled I domains were intravenously injected into the mice with HeLa/293T xenograft. When the xenograft tissue was examined 4 h after nanoparticle injection, specific accumulation of LMN into HeLa tumor was observed, judging from colocalization between GFP expression in HeLa and AF594 fluorescence (Figure 2.15). Importantly, consistent with the detection of ICAM-1 in the tumor vasculature by direct staining of the tissue (Figure

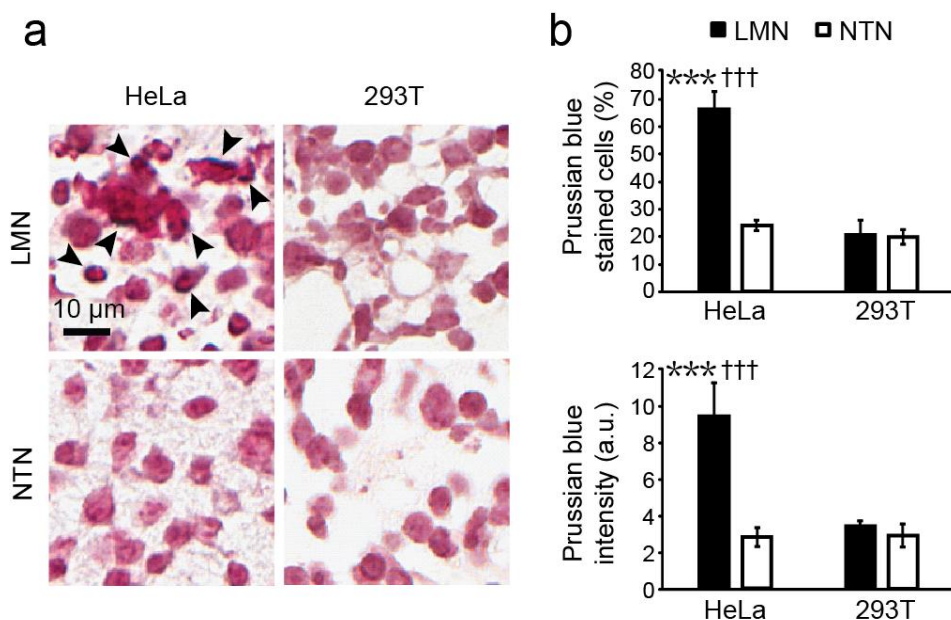


Figure 2.14: (a) Perls' Prussian blue staining of tumor sections collected at 50 h after the injection of LMN vs. NTN. Stained iron is marked with black arrows. (b) Percentage of cells stained in Prussian blue (top) and the intensity of Prussian blue in the field of view (bottom) within tumor sections (n = 3; ***p < 0.001 between LMN vs. NTN in HeLa tumor. †††p < 0.001 between HeLa and 293T tumor using LMN).

2.9), a high percentage of CD31 positive cells in HeLa as well as in 293T xenografts were also targeted by LMN. The localization of ICAM-1 specific nanoparticles within the tumor-associated vasculature, therefore, was likely responsible for higher signals detected within 293T xenograft at earlier time points (Figure 2.13), despite the fact that 293T itself exhibited almost no binding of LMN (Figure 2.14). This finding highlights a potential use of LMN for detection of tumor growth by their accumulation into inflamed tumor vasculature, irrespective of the type of tumor surface antigen.

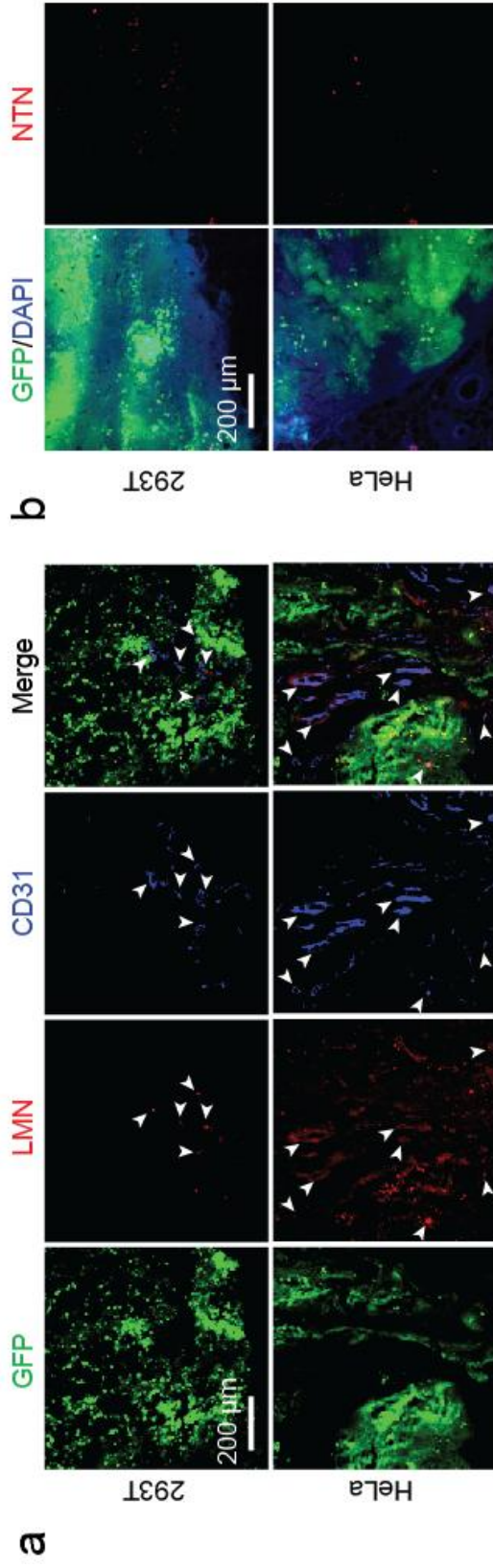


Figure 2.15: (a) Immunofluorescence imaging of tumors at 4 h post-injection of LMN. Tumor sections were also stained with anti-CD31 antibody for delineating vasculature. LMN localization into the tumor vasculature was indicated with white arrows. (b) Fluorescence imaging of tumors at 4 h post-injection of NTN.

2.4.5 In vivo detection of temporal dynamics of inflammation by optical imaging and MRI

In order to further confirm that our leukocyte-mimetic nanoparticles sensitively detect the induction of ICAM-1 not only due to an inflammatory milieu in the tumor but also by acutely induced inflammation, we imaged mice after subcutaneous (Figure 2.16) or intravenous injection of LPS (Figure 2.17 & 2.18). Temporal mapping of nanoparticle distribution demonstrated a greater localization of LMN into the LPS injection site over PBS injection site as a control, peaking at 12 h post-injection of LPS and gradually decaying over 72 h (Figure 2.16a & 2.16b). Higher accumulation into the liver was also observed with LMN, attributed to the inflammatory response induced by the leakage of locally injected LPS into circulation. We also observed a rapid increase in fluorescence in the bladder, irrespective of targeting moieties, attributed to renal clearance of some fraction of proteins dissociated from nanoparticles. Interestingly, NTN accumulated more into the LPS site than into the PBS site, presumably due to non-specific phagocytosis of nanoparticles by immune cells. Selected mice treated with systemic delivery of 100 μg LMN were then subjected to MRI after whole body optical imaging to demonstrate that our nanoparticles could be used for quantitative detection of inflammation by a clinically relevant imaging technique (Figure 2.16c). T2* magnitude images identified the presence of LMN in the LPS injection site as darkness, which could be confused with other dark regions. QSM revealed the accumulation of ~ 0.3 μg of iron oxide (corresponding to detection of less than 1% of injected dose) into the LPS injection site, colocalized with the site identified by near-IR imaging (Figure 2.17a).

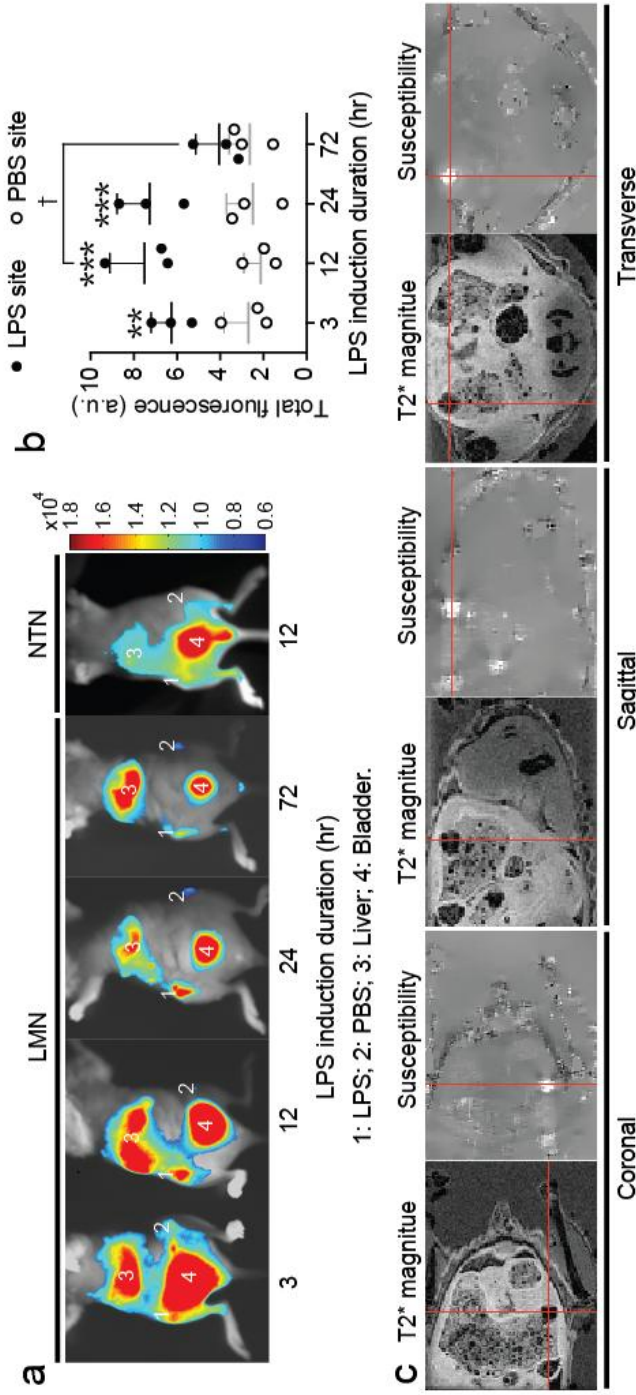


Figure 2.16: (a) *In vivo* near-IR whole body imaging of LMN vs. NTN distribution in mice 1 h after nanoparticle injection. Mice were exposed to LPS ('1') and PBS ('2') for 3, 12, 24, or 72 h at the time of nanoparticle delivery. (b) Fluorescence intensities of LMN at LPS vs. PBS injection sites were shown (n = 3; **p < 0.01, ***p < 0.001 between LPS and PBS site at specific time points; †p < 0.05 between 12 h and 72 h at LPS site). (c) T2* magnitude and susceptibility mapping images of nanoparticle distribution in mice at 4 h after nanoparticle injection. Mice were exposed to LPS/PBS for 12 h at the time of nanoparticle injection. Bright spot identified by susceptibility mapping as the accumulation of SPIO was indicated with crosshair.

In response to systemic inflammation caused by intravenous injection of LPS for 12 h prior to nanoparticle (~200 µg) injection, optical mapping of nanoparticle distribution demonstrated greater localization of LMN in the liver compared to that of NTN in mice (Figure 2.17), peaking at 1 h post-injection of nanoparticles and subsequently diminishing at later time points. The level of delivery overall was higher with LPS even with NTN, indicating some of nanoparticles accumulated into the liver was caused by ICAM-1 independent phagocytosis. After optical imaging, mice were transcardially perfused with PBS for MRI, which would have removed nanoparticles retained in the blood pool in the liver. Temporal mapping of SPIO distribution using MRI QSM measured about 20% of the total dose of LMN was specifically uptaken by the liver 1 h post injection due to LPS-induced inflammation (Figure 2.18). QSM quantification also demonstrated a similarly greater localization of LMN into the liver under acute inflammation at different time points, exhibiting qualitative agreement with the temporal mapping using optical imaging (Figure 2.18). Discrepancy between optical intensity and QSM was unavoidable as MRI was performed after perfusion of the mice as well as due to the different kinetics of degradation for fluorescence dye (AF750) and SPIO.

2.5 Discussion

Sensitive detection of inflammation will be of high significance for diagnosis of diseases caused directly by host inflammatory response such as sepsis, allograft rejection, lupus, as well as those that are influenced by inflammation such as

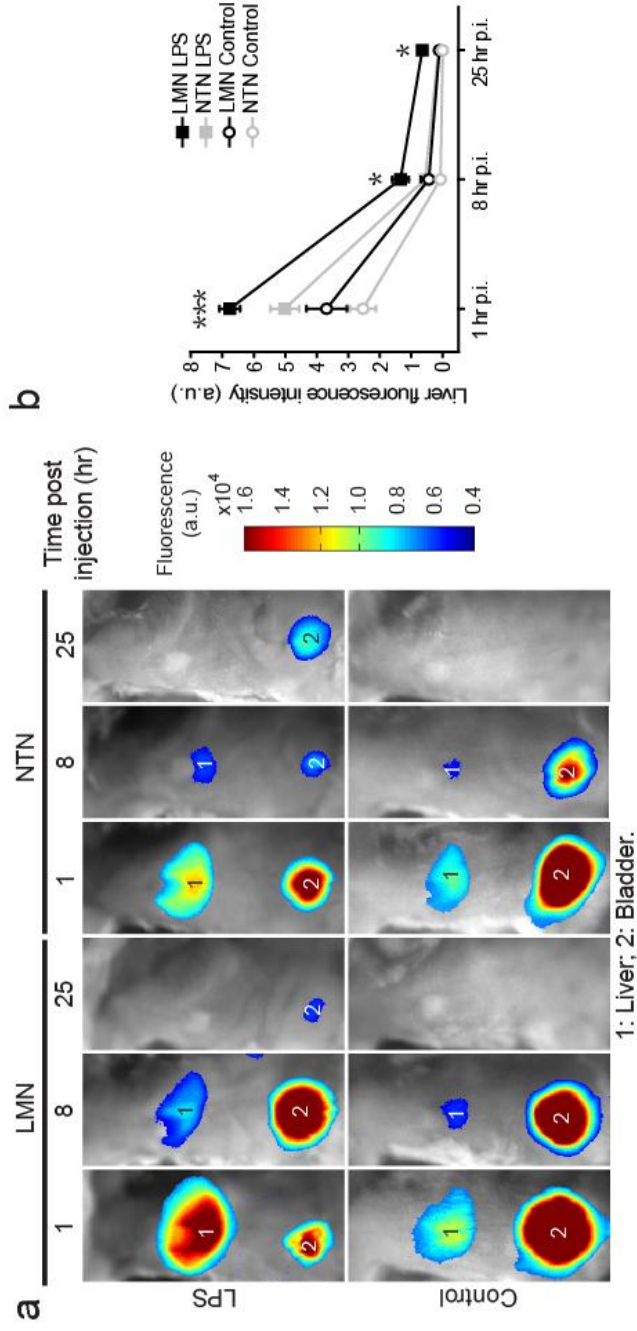


Figure 2.17: (a) *In vivo* near-IR whole body imaging of LMN vs. NTN distribution in mice at 1, 8, 25 h post-injection of nanoparticles in mice exposed to systemic LPS for 12 h or control mice with no treatment. (b) LMN vs. NTN distributions into the liver were quantified by near-IR optical imaging (n = 3; **p < 0.05, ***p < 0.001 between LMN vs. NTN at specific time points).

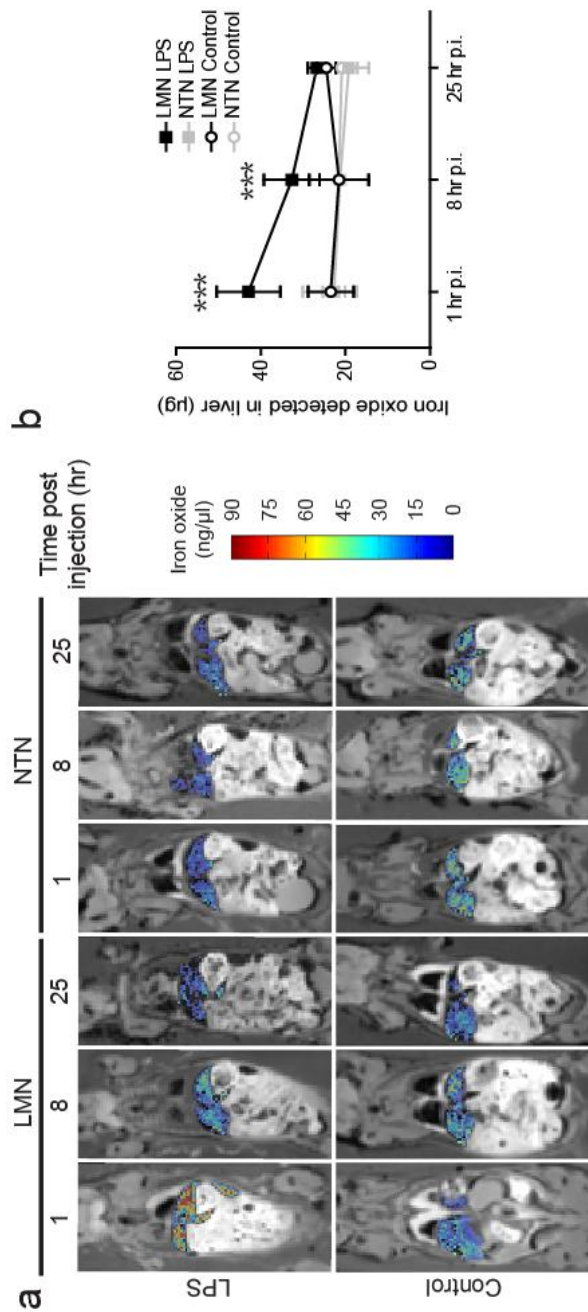


Figure 2.18: (a) MR imaging of LMN vs. NTN distribution in mice at 1, 8, 25 h post-injection of nanoparticles in mice exposed to systemic LPS for 12 h or control mice with no treatment. (b) LMN vs. NTN distributions into the liver were quantified by QSM (n = 3; *p < 0.05, ***p < 0.001 between LMN vs. NTN at specific time points).

cardiovascular disease and cancer. In this study, we designed MRI-compatible SPIO nanoparticles, and demonstrated a successful detection of constitutive expression of ICAM-1 in tumor, as well as ICAM-1 induction in tumor-associated vasculature, where tumor growth and angiogenesis are active. Prior approaches to inflammation detection have been largely based on antibodies that are against cell adhesion molecules such as ICAM-1 and VCAM-1 [8-13, 29], lacking in the ability to fine tune affinity and avidity of targeting moieties on nanoparticles that are critical to inflammation-specific targeting. From our previous *in vitro* studies [17, 24], we have demonstrated specific localization into inflamed but not to resting endothelium and immune cells of nanoparticle (50-100 nm in diameter) coated with integrin LFA-1 I domain engineered for high affinity to ICAM-1. Furthermore, combining recently developed quantitative susceptibility mapping technique, we quantified sub-microgram quantity of iron oxide accumulated in both ICAM-1-expressing cell phantom *in vitro* and acute inflammation induced by LPS *in vivo*, corresponding to less than 1% of injected dose.

Despite the fact that ICAM-1 is basally expressed in all endothelium [16, 23] and therefore the notion that ICAM-1 may not be a suitable target for inflammation, our studies emphasize selective delivery by targeting molecules that are induced greatly under inflammation [30, 31]. Nanoparticles of ~100 nm will experience hydrodynamic force generated by the blood flow [32, 33], such that there should be sufficient simultaneous molecular interactions with the cells for nanoparticles to remain on cell surface. The number of minimum molecular interactions required for stable adhesion of nanoparticles will also depend on the adhesion strength of each

interaction. Therefore, specificity toward high ICAM-1 site will be influenced by the affinity of molecular interaction and the valency between nanoparticles and target cells, where the design of nanoparticles to permit tunable affinity and avidity of physiological interaction is of significant advantage. Our nanoparticles to a great extent mimic the behavior of activated leukocytes, which would adhere much better to inflamed endothelium.

Increasing number of studies have begun to focus on the crosstalk between the immune activation of vascular niche, angiogenesis, and tumor progression [34, 35]. Upregulated levels of ICAM-1 in tumor have been linked to two different contexts, one serving as a marker for the recruitment of effector immune cells and tumor killing [36], while it was also observed in malignant and metastatic tumors with poor prognosis [37]. Seemingly contradicting roles of ICAM-1 may be due to the complexity of inflammation in various phases of tumor development, which can be better examined by *in vivo* imaging tools. Our nanoparticles did indeed show the localization into the tumor vasculature, while their localization into the vasculature elsewhere was non-detectable. With human tumor xenograft model, we observed that the majority of tumor mass was comprised of tumor cells with poor vascularity present therein. Higher vascularity was found in the periphery of the tumor, often called the invasive tumor front, where ICAM-1 overexpression associated with higher immune activity has also been reported in many carcinoma cases [27, 38-41]. Notably, we have demonstrated that intravenously injected nanoparticles targeting ICAM-1 specifically localized into the vasculature associated with the tumor progression. With further improvement of detection sensitivity in addition to more native tumor models

containing not only tumor cells themselves but also fully-developed vasculatures and other stroma cells such as macrophages, our nanoparticles may provide a universal tumor imaging strategy not by tumor surface markers limited to specific cancer types but by the inflamed microenvironment which is associated with almost all cancer development.

Besides sensitive detection of chronic inflammation implicated in cancer, prompt and accurate detection of acute inflammation induced by bacterial or viral infection such as sepsis is also of clinical importance. Acute inflammation dramatically induces ICAM-1 induction not only in endothelium but also in immune cells, such that both cellular components become the targets by I domain-coated nanoparticle. Using LPS-induced acute inflammation model, we demonstrated optical imaging of the temporal dynamics of inflammation. Specific localization of LMN was also confirmed by QSM technique using MRI. The degree of localization of ICAM-1 targeting nanoparticles into an inflamed site will closely reflect different phases of inflammation, from the onset of inflammation to resolution phase. Therefore, quantitative prediction of spatiotemporal distribution of nanoparticles may provide critical information on diagnosis and the choice of therapy regimen in clinics.

In summary, our ICAM-1 targeting strategy by mimicking the behavior of leukocytes in their ability to localize to the inflamed endothelium was able to detect ICAM-1 overexpression in tumor cells, tumor vascular microenvironment, and acute inflammation. In the design of ICAM-1 targeting nanoparticles by conjugation with LFA-1 I domain, we employed His-tag binding to nickel-NTA, which we previously found [17] to be critical in order to fine-tune the coating density of targeting moieties

to be specific to ICAM-1 overexpression but not to basally present ICAM-1. The idea of optimizing molecular interactions by tuning the avidity between ligands and receptors could provide a useful strategy to molecular targeting of some important targets that are basally expressed elsewhere. Inflammation-targeting nanoparticles with the lipid layer shell can also be used to carry small, hydrophobic drugs, achieving simultaneous imaging and targeted drug delivery.

2.6 Conclusion

This study presents physiology-inspired design of SPIO nanoparticles for *in vivo* detection by optical imaging and MRI, mimicking activated leukocyte in its ability to recognize inflamed endothelium. Nanoparticles *in vivo* will experience hydrodynamic force induced by the blood flow, requiring simultaneous molecular interactions with sufficient adhesion strength with the cells for nanoparticles to remain on cell surface. Therefore, the design of nanoparticles with tunable affinity and avidity of physiological interactions would be critical to selectivity and efficiency of leukocyte-mimetic nanoparticles in targeting inflammation. Notably, we observed specific accumulation of systemically-delivered nanoparticles into the vasculature within the tumor and invasive tumor front where the tumor growth and angiogenesis were active, while their localization into the vasculature elsewhere was much lower. The use of two different nanoparticles differed only by the type of I domains (active vs. inactive) as targeting moieties against ICAM-1 enabled us to discriminate inflammation-driven accumulation into the tumor microenvironment from passive distribution, which may result from the leakiness of the vasculature within the tumor.

Inflammation-targeting nanoparticles such as SPIO with the layer of phospholipid are also suitable for carrying small molecule drugs, achieving simultaneous imaging and targeted drug delivery.

REFERENCES

- [1] Nathan C, Ding A. Nonresolving inflammation. *Cell*. 2010;140:871-82.
- [2] Cohen J. The immunopathogenesis of sepsis. *Nature*. 2002;420:885-91.
- [3] Glass CK, Saijo K, Winner B, Marchetto MC, Gage FH. Mechanisms underlying inflammation in neurodegeneration. *Cell*. 2010;140:918-34.
- [4] Libby P. Inflammation in atherosclerosis. *Nature*. 2002;420:868-74.
- [5] Hotamisligil GS. Inflammation and metabolic disorders. *Nature*. 2006;444:860-7.
- [6] Coussens LM, Werb Z. Inflammation and cancer. *Nature*. 2002;420:860-7.
- [7] Mantovani A, Allavena P, Sica A, Balkwill F. Cancer-related inflammation. *Nature*. 2008;454:436-44.
- [8] Sipkins DA, Gijbels K, Tropper FD, Bednarski M, Li KC, Steinman L. ICAM-1 expression in autoimmune encephalitis visualized using magnetic resonance imaging. *J Neuroimmunol*. 2000;104:1-9.
- [9] Weller GE, Lu E, Csikari MM, Klibanov AL, Fischer D, Wagner WR, et al. Ultrasound imaging of acute cardiac transplant rejection with microbubbles targeted to intercellular adhesion molecule-1. *Circulation*. 2003;108:218-24.
- [10] Zhang N, Chittasupho C, Duangrat C, Siahaan TJ, Berkland C. PLGA nanoparticle-peptide conjugate effectively targets intercellular cell-adhesion molecule-1. *Bioconjug Chem*. 2008;19:145-52.
- [11] Kelly KA, Allport JR, Tsourkas A, Shinde-Patil VR, Josephson L, Weissleder R. Detection of vascular adhesion molecule-1 expression using a novel multimodal nanoparticle. *Circ Res*. 2005;96:327-36.

- [12] Voinea M, Manduteanu I, Dragomir E, Capraru M, Simionescu M. Immunoliposomes directed toward VCAM-1 interact specifically with activated endothelial cells--a potential tool for specific drug delivery. *Pharm Res.* 2005;22:1906-17.
- [13] Nahrendorf M, Keliher E, Panizzi P, Zhang H, Hembrador S, Figueiredo JL, et al. 18F-4V for PET-CT imaging of VCAM-1 expression in atherosclerosis. *JACC Cardiovasc Imaging.* 2009;2:1213-22.
- [14] Ehrhardt C, Kneuer C, Bakowsky U. Selectins-an emerging target for drug delivery. *Adv Drug Deliv Rev.* 2004;56:527-49.
- [15] Chan JM, Zhang L, Tong R, Ghosh D, Gao W, Liao G, et al. Spatiotemporal controlled delivery of nanoparticles to injured vasculature. *Proc Natl Acad Sci U S A.* 2010;107:2213-8.
- [16] Dustin ML, Rothlein R, Bhan AK, Dinarello CA, Springer TA. Induction by IL 1 and interferon-gamma: tissue distribution, biochemistry, and function of a natural adherence molecule (ICAM-1). *J Immunol.* 1986;137:245-54.
- [17] Kang S, Park T, Chen X, Dickens G, Lee B, Lu K, et al. Tunable physiologic interactions of adhesion molecules for inflamed cell-selective drug delivery. *Biomaterials.* 2011;32:3487-3498.
- [18] Jin M, Song G, Carman CV, Kim YS, Astrof NS, Shimaoka M, et al. Directed evolution to probe protein allostery and integrin I domains of 200,000-fold higher affinity. *Proc Natl Acad Sci U S A.* 2006;103:5758-63.
- [19] Liu T, Spincemaille P, de Rochefort L, Kressler B, Wang Y. Calculation of susceptibility through multiple orientation sampling (COSMOS): a method for conditioning the inverse problem from measured magnetic field map to susceptibility source image in MRI. *Magn Reson Med.* 2009;61:196-204.

- [20] Wharton S, Schafer A, Bowtell R. Susceptibility mapping in the human brain using threshold-based k-space division. *Magn Reson Med.* 2010;63:1292-304.
- [21] Weber C, Fraemohs L, Dejana E. The role of junctional adhesion molecules in vascular inflammation. *Nat Rev Immunol.* 2007;7:467-77.
- [22] Shimaoka M, Lu C, Palframan RT, von Andrian UH, McCormack A, Takagi J, et al. Reversibly locking a protein fold in an active conformation with a disulfide bond: integrin alphaL I domains with high affinity and antagonist activity in vivo. *Proc Natl Acad Sci U S A.* 2001;98:6009-14.
- [23] Marlin SD, Springer TA. Purified intercellular adhesion molecule-1 (ICAM-1) is a ligand for lymphocyte function-associated antigen 1 (LFA-1). *Cell.* 1987;51:813-9.
- [24] Park S, Kang S, Veach AJ, Vedvyas Y, Zarnegar R, Kim JY, et al. Self-assembled nanoplatform for targeted delivery of chemotherapy agents via affinity-regulated molecular interactions. *Biomaterials.* 2010;31:7766-75.
- [25] Dubertret B, Skourides P, Norris DJ, Noireaux V, Brivanlou AH, Libchaber A. In vivo imaging of quantum dots encapsulated in phospholipid micelles. *Science.* 2002;298:1759-62.
- [26] Kelly CP, O'Keane JC, Orellana J, Schroy PC, 3rd, Yang S, LaMont JT, et al. Human colon cancer cells express ICAM-1 in vivo and support LFA-1-dependent lymphocyte adhesion in vitro. *Am J Physiol.* 1992;263:G864-70.
- [27] Maurer CA, Friess H, Kretschmann B, Wildi S, Muller C, Graber H, et al. Overexpression of ICAM-1, VCAM-1 and ELAM-1 might influence tumor progression in colorectal cancer. *Int J Cancer.* 1998;79:76-81.
- [28] Hayes SH, Seigel GM. Immunoreactivity of ICAM-1 in human tumors, metastases and normal tissues. *Int J Clin Exp Pathol.* 2009;2:553-60.

- [29] Reinhardt M, Hauff P, Linker RA, Briel A, Gold R, Rieckmann P, et al. Ultrasound derived imaging and quantification of cell adhesion molecules in experimental autoimmune encephalomyelitis (EAE) by Sensitive Particle Acoustic Quantification (SPAQ). *Neuroimage*. 2005;27:267-78.
- [30] Osborn L. Leukocyte adhesion to endothelium in inflammation. *Cell*. 1990;62:3-6.
- [31] Springer TA. Adhesion receptors of the immune system. *Nature*. 1990;346:425-34.
- [32] Shi W, Wang J, Fan X, Gao H. Size and shape effects on diffusion and absorption of colloidal particles near a partially absorbing sphere: implications for uptake of nanoparticles in animal cells. *Phys Rev E Stat Nonlin Soft Matter Phys*. 2008;78:061914.
- [33] Mailander V, Landfester K. Interaction of nanoparticles with cells. *Biomacromolecules*. 2009;10:2379-400.
- [34] Rajashekhar G, Willuweit A, Patterson CE, Sun P, Hilbig A, Breier G, et al. Continuous endothelial cell activation increases angiogenesis: evidence for the direct role of endothelium linking angiogenesis and inflammation. *J Vasc Res*. 2006;43:193-204.
- [35] Franses JW, Baker AB, Chitalia VC, Edelman ER. Stromal endothelial cells directly influence cancer progression. *Sci Transl Med*. 2011;3:66ra5.
- [36] Pandolfi F, Trentin L, Boyle LA, Stamenkovic I, Byers HR, Colvin RB, et al. Expression of cell adhesion molecules in human melanoma cell lines and their role in cytotoxicity mediated by tumor-infiltrating lymphocytes. *Cancer*. 1992;69:1165-73.
- [37] Kobayashi H, Boelte KC, Lin PC. Endothelial cell adhesion molecules and cancer progression. *Curr Med Chem*. 2007;14:377-86.

- [38] Nelson H, Ramsey PS, Donohue JH, Wold LE. Cell adhesion molecule expression within the microvasculature of human colorectal malignancies. *Clin Immunol Immunopathol.* 1994;72:129-36.
- [39] Fox SB, Turner GD, Leek RD, Whitehouse RM, Gatter KC, Harris AL. The prognostic value of quantitative angiogenesis in breast cancer and role of adhesion molecule expression in tumor endothelium. *Breast Cancer Res Treat.* 1995;36:219-26.
- [40] Suzuki Y, Ohtani H, Mizoi T, Takeha S, Shiiba K, Matsuno S, et al. Cell adhesion molecule expression by vascular endothelial cells as an immune/inflammatory reaction in human colon carcinoma. *Jpn J Cancer Res.* 1995;86:585-93.
- [41] Cianchi F, Cuzzocrea S, Vinci MC, Messerini L, Comin CE, Navarra G, et al. Heterogeneous expression of cyclooxygenase-2 and inducible nitric oxide synthase within colorectal tumors: correlation with tumor angiogenesis. *Dig Liver Dis.* 2010;42:20-7.

CHAPTER 3

VISUALIZING AND QUANTIFYING ACUTE INFLAMMATION USING ICAM-1 SPECIFIC NANOPARTICLES AND MRI QUANTITATIVE SUSCEPTIBILITY MAPPING

Published in *Annals of Biomedical Engineering*²

3.1 Abstract

As intense and prolonged inflammation correlates with the progression of various inflammatory diseases, locating specific regions of the body with dysregulated levels of inflammation could provide crucial information for effective medical diagnosis and treatment. In this study, we demonstrate high resolution spatiotemporal imaging of inflammation in mice treated with systemic injection of lipopolysaccharides (LPS) to mimic systemic inflammatory response or sepsis. Diagnosis of organ-level inflammation was achieved by magnetic resonance imaging (MRI) of inflammation-sensitive superparamagnetic iron oxide (SPIO)-based nanomicelle termed leukocyte-mimetic nanoparticle (LMN), designed to preferentially localize to cells with inflammation-induced overexpression of intercellular adhesion molecule (ICAM)-1. Using a novel MRI quantitative susceptibility mapping (QSM) technique for non-invasive quantification of SPIO nanoparticles, we observed greater

² This chapter is modified with the permission of the publisher from Wong R, Chen X, Wang Y, Hu X, Jin MM. Visualizing and Quantifying Acute Inflammation Using ICAM-1 Specific Nanoparticles and MRI Quantitative Susceptibility Mapping. *Annals of Biomedical Engineering*. 2011. Xiaoyue Chen designed the study, conducted the experiments, analyzed the data and wrote the paper with regard to the following figures: 3.2, 3.3, 3.4, 3.6, 3.8, 3.10, 3.11 & 3.12.

accumulation of LMN in the liver, specific to ICAM-1 induction due to LPS-induced inflammation. However, the accumulation of nanoparticles into the spleen appeared to be due to an ICAM-1 independent, phagocytic activity, resulting in higher levels of both LMN and control nanoparticles in the spleen of LPS-treated than untreated mice. Overall, the amounts of nanoparticles in liver and spleen estimated by QSM were in a good agreement with the values directly measured by radioactivity, presenting an idea that spatiotemporal mapping of LMN by MRI QSM may provide a reliable, rapid, non-invasive method for identifying organ-specific inflammation not offered by existing diagnostic techniques.

3.2 Introduction

Nonresolving inflammation contributes significantly to the pathogenesis of a variety of human diseases and represents one of the most significant factors of medical burden worldwide [1]. While inflammation is typically initiated in response to harmful stimuli, dysregulation of the inflammation pathways can result in prolonged and excessive inflammation, leading to host damage that can surpass the harm inflicted by the original pathogen [2]. Indeed, unresolving chronic inflammation has been linked to atherosclerosis [3], obesity [4], and cancer [5], prolonged acute inflammation has been closely associated with sepsis [6] and local infections [7], and the cyclic coexistence of acute and chronic inflammation has been implicated in rheumatoid arthritis [8], asthma [9], multiple sclerosis, Crohn's disease, and ulcerative colitis [1]. Of particular concern of inflammatory dysregulation is the intense localized recruitment of macrophages, lymphocytes, and neutrophils to otherwise healthy tissue, resulting in

necrosis of vital tissues and organs, contributing greatly to increased patient morbidity and mortality [10]. Thus, identifying localized inflammation in the context of broader inflammation-driven diseases can aid in isolating regions at risk of host-response necrosis and can provide a valuable insight into the progression and severity of the condition.

Current approaches to inflammation detection employ various markers as targets for biospecificity, including soluble extracellular molecules, such as fibrinogen [11], factor XIII [12], and collagen [13], as well as cell surface molecules such as tissue factor [14], chondroitin sulfate proteoglycans [15], vascular adhesion molecule (VCAM-1) [16], and ICAM-1 [17-19]. Of particular interest is ICAM-1, a transmembrane molecule that displays a distinct spatiotemporal response to inflammation. While basally expressed at low levels throughout the body under normal conditions, ICAM-1 is highly inducible under inflammatory stimuli [20] and exhibits highly localized cell surface expression on immune and non-immune cells, such as endothelial cells, fibroblasts, lymphocytes, and myeloid cells [21]. Furthermore, cell surface ICAM-1 overexpression has been linked to various diseases and conditions, and correlates well with inflammation-related tissue and organ damage resulting from hepatic ischemia [22-23], intestinal and colon ischemias [24], hepatitis, cirrhosis, Wilson's disease, transplantation rejection [25], pancreatitis [26], type 1 diabetes [27], and multiple organ dysfunction syndrome in sepsis [6]. To target cell surface ICAM-1, we previously employed a high affinity variant of the domain called inserted (I) domain [28], present in the α subunit of the integrin lymphocyte function-

associated antigen (LFA)-1 and solely responsible for LFA-1 interaction with ICAM-1 [29].

One potential application for specific inflammation imaging is for the detection of sepsis. Sepsis is the leading cause of death in critically ill patients admitted to the medical intensive care unit (ICU) in the United States [30], defined as a systemic inflammatory response to infection manifested by two or more systemic inflammatory response syndrome (SIRS) criteria (such as changes in body temperature, tachycardia, and changes in the number and/or immaturity of white blood cells) [6]. Under sepsis, the endothelium experiences sustained and generalized activation, resulting in procoagulant phenotype, increased endothelial cell apoptosis, increased expression of adhesion molecules, and ultimately organ-specific coagulation and dysfunction [6]. As ICAM-1 plays a significant role in mediating leukocyte adhesion as a part of inflammatory response and has been linked to organ-specific inflammation-driven necrosis, identifying sites of high ICAM-1 expression may offer detection or even additional insight into the progression of sepsis or other systemic inflammatory response not offered by existing diagnostic techniques.

In this study, we demonstrate that high resolution spatiotemporal imaging of LPS-induced systemic inflammation through the use of inflammation-specific nanoparticles termed leukocyte-mimetic nanoparticles (LMN) [31], a fluorescently tagged ICAM-1 specific nanomicelle encapsulating superparamagnetic iron oxide nanoparticle as a targeted bimodal near-infrared (NIR) optical/magnetic resonance imaging (MRI) contrast agent. Using optical imaging and a novel MRI quantitative susceptibility mapping (QSM) technique [32], and directly corroborated by

radiolabeled isotope measurement, we utilize LMN to quantitatively observe the degree of localized acute inflammation as an indicator of sepsis progression. By tracking the biodistribution of nanoparticles using whole body imaging techniques, we have found greater accumulation of LMN than that of non-ICAM-1 specific controls in the liver of septic mice, while this difference in accumulation was absent in the liver of non-septic mice. In contrast, greater accumulation of nanoparticles irrespective of ICAM-1 targeting was observed in the spleen of septic mice than that of non-septic control, suggesting that localization into the spleen was mainly a result of ICAM-1 independent phagocytic activity. Our study demonstrates the utility of quantitative MRI-based detection of ICAM-1 specific nanoparticles in the major organs including the liver and spleen, organs closely associated with systemic inflammatory response, as a diagnosis method for systemic inflammation through the imaging and quantification of localized inflammation.

3.3 Materials and methods

3.3.1 Preparation of ICAM-1 specific nanoparticles (Leukocyte-mimetic nanoparticles (LMN))

Details in the synthesis of LMN were described previously [31] . Briefly, oleic acid-capped superparamagnetic iron oxide (SPIO) nanocrystals (15 nm in diameter, Ocean Nanotech, LLC) were additionally coated with an outer layer of phospholipid, consisting of 1,2-dipalmitoyl-snglycero-3-phosphoethanolamine-N-[methoxy(polyethylene glycol)-2000] (DPPE-PEG) and 1,2-dioleoyl-sn-glycero-3-[(N-(5-amino-1-carboxypentyl)iminodiacetic acid)succinyl] nickel salt (DOGS-NTA)

(Avanti Polar Lipids, Inc.). Radiolabeled lipid-coated SPIO nanoparticles were synthesized by addition of ^3H -DPPC (L- α -Dipalmitoyl-Phosphatidylcholine) (Perkin Elmer) at less than 5% of the total phospholipid to the mixture of DPPE-PEG and DOGS-NTA. The lipid layer on SPIO nanoparticles was formed by hydration of the mixture of lipid-film and SPIO, and lipid-coated SPIO were then purified by density centrifugation, followed by a gel filtration technique. LFA-1 I domains containing mutations of Asp137 \rightarrow Ala (D137A; non-ICAM-1 specific) and Phe265 \rightarrow Ser/Phe292 \rightarrow Gly (F265S/F292G; ICAM-1 specific) fused to His tag (6 histidine residues) at the N-terminal were produced as previously described [31]. Conjugation of lipid-SPIO with His-tagged I domains was obtained by incubation of nanoparticles with I domains at 4 °C overnight, forming LMN (with F265S/F292G) and non-targeting nanoparticle (NTN) (with D137A). All fluorescently labeled nanoparticles were prepared by covalently conjugating Alexa Fluor 750 (AF750) (succinimidyl esters (Invitrogen) to the I domains.

3.3.2 Animal model of acute inflammation

All animal experiments were conducted in compliance with the regulations defined by the Institutional Laboratory Animal Use and Care Committee of Cornell University. 1 mg/ml LPS in 100 μl PBS were injected intravenously through retroorbital vein into 8-wk-old female BALB/c mice 12 h before nanoparticle administration. Prior to imaging hair was removed to reduce background fluorescence. Mice with no treatment were used as negative control. Three mice per group were used for each treatment and imaging regimen.

3.3.3 Near-IR optical and MR imaging of mice

Animals were anesthetized with isoflurane mixed with oxygen at 5% and maintained at 2% isoflurane during whole body imaging (Olympus, OV100). After 12 hour treatment with LPS or no-treatment control, mice were administered with 100 μg of nanoparticles coated with AF750-conjugated I domains in 150 μl pH 7.4 PBS via retro-orbital injection. Near-IR images of the same mice were taken three times at 1, 8, and 25 hours after nanoparticle injection. Image analysis was performed with Matlab R2007a (MathWorks). Mice were euthanized at 1, 8, or 25 hours after injection of nanoparticles for MRI by intraperitoneal injection of 2.5% tribromoethanol (20 $\mu\text{l/g}$), transcardially perfused with pH 7.4 PBS, and fixed in 4% paraformaldehyde. Prepared mice were scanned on a 3T scanner (GE Signa Excite) with 3D multi-echo enhanced fast gradient echo (EFGRE) sequence. Imaging parameters were as follows: TEs 3.696 ms, 4.196 ms, 5.696 ms, 11.696 ms, 35.696 ms; TR 40 ms; flip angle 30 $^{\circ}$; matrix size 256 \times 64 \times 64; voxel size 500 μm isotropic. A 3D Fourier transform was applied to the raw k-space data to reconstruct the images. QSMs were reconstructed using the COSMOS technique, as previously described [31]. Regions of interest were segmented for the liver, spleen, and kidneys, and SPIO localization was estimated using QSM, normalized to a calibration standard.

3.3.4 Histological sections

At 1 hour post nanoparticle injections, mice were euthanized and perfused with PBS transcardially. Liver tissues were then collected from animals. Part of the tissues were fixed in 4% paraformaldehyde, embedded in paraffin, sliced into 4 μm slides, and stained with hematoxylin and eosin (H&E) or with Perls' Prussian blue. The rest of the tissues were frozen in OCT compounds (Sakura Finetek), sectioned to 10 μm

slides, and immunostained with rat anti-mouse CD68 (BioLegend) for detection of macrophages.

3.3.5 Quantification of radiolabeled LMN

Animals were anesthetized with isoflurane and each was administered with 100 µg ³H-labeled SPIO (600 nCi per mouse) in 100 µl PBS via retro-orbital injection. At 1 hour post injection, blood samples were first collected and mice were perfused with PBS and sacrificed. Major organs were harvested, homogenized, lysed in tissue solubilizer (Fisher), and then mixed with scintillation counter fluid for radioactivity measurement (Beckman Coulter). Percent distribution into the major organs was obtained after normalization to the total counts of radioisotope decay per animal.

3.3.6 Surface plasmon resonance (SPR) analysis

The affinity of human LFA-1 I domains, F265S/F292G and D137A, to murine ICAM-1 was determined by SPR using BIAcore (BIA2000), as previously described [28]. In brief, a CM5 sensor chip was prepared using an amine coupling kit (BIAcore) to immobilize recombinant murine ICAM-1 fusion with human IgG1 Fc (R&D Systems). Then F265S/F292G and D137A were injected over the chip in injection buffer (20 mM Tris HCl, pH 8.0, 150 mM NaCl, 10 mM MgCl₂) at a flow rate of 10 µl/min at RT. In order to examine the specificity of nanoparticle to the level of ICAM-1 expression, CM5 sensor chip was immobilized with three different concentrations of ICAM-1, representing basal to highly induced cell surface density (200, 1000 and 3,250 molecules/µm²) [33]. Nanoparticles were then flowed over the chip at a flow rate of 15 µl/min to approximate the shear force on nanoparticles *in vivo*.

3.3.7 Statistical analysis

Statistical analysis was performed using two-way analysis of variance and one-way analysis of variance with Tukey's HSD post-hoc test at 95% confidence interval (GraphPad Prism).

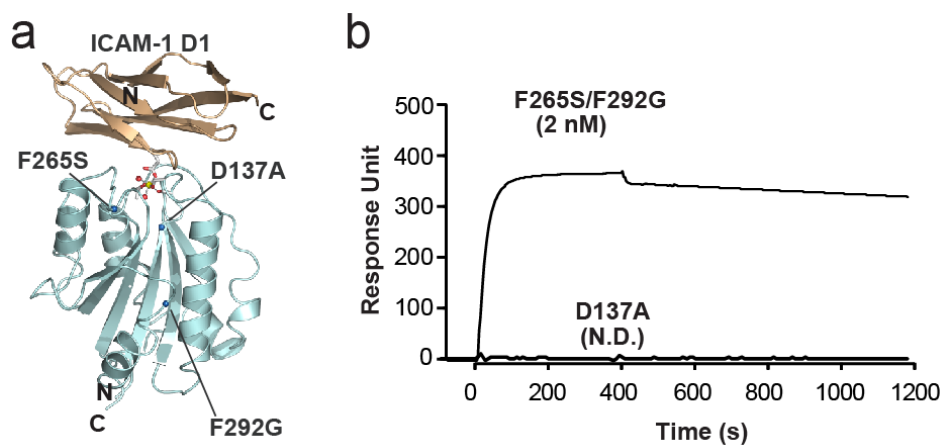


Figure 3.1: (a) Structural model of the complex of ICAM-1 domain 1 and LFA-1 I domain. White spheres depict allosteric activation sites along the peptide backbone. Metal ion and two oxygen atoms of water molecules are depicted as colored spheres. Residues that coordinate to the metal ion are shown as sticks. Mutations of Phe265→Ser (F265S), Phe292→Gly (F292G), and Asp137→Ala (D137A), and N and C termini are indicated. Figure adapted from Hu et al [44]. (b) SPR measurement of the binding kinetics of I domain variants F265S/F292G and D137A to immobilized murine ICAM-1. F265S/F292G exhibits high ICAM-1 binding affinity ($K_D = 2$ nM), while variant D137A indicates no (not determinable) binding affinity.

3.4 Results

Previously, we validated the suitability of I domain as a targeting moiety for selective binding of nanoparticles to ICAM-1 overexpression [17, 19, 31]. In order to

design control nanoparticles, termed non-targeted nanoparticle (NTN), we used the same LFA-1 I domain but containing a mutation of D137A, which abolished a ligand-binding site called a metal-ion adhesion site (MIDAS) and subsequently its binding to ICAM-1 (Figure 3.1a). SPR measurement confirmed our previous observation with cell staining [31] that human I domain cross-reacted with murine ICAM-1 with comparable affinity to human ICAM-1 ($K_D = 2$ nM to murine ICAM-1 vs. 6 nM to human ICAM-1 [28]; Figure 3.1b). Subsequent conjugation of F265S/F292G and D137A to prepared lipid-coated SPIO nanoparticles produced LMN and NTN, respectively, through spontaneous assembly from binding of His tag (6 histidine residues) to Nickel-NTA (Figure 3.2).

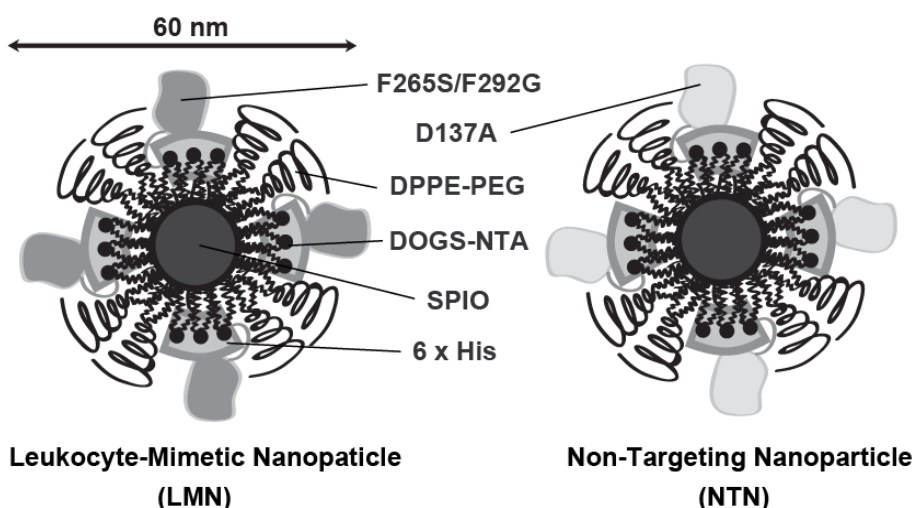


Figure 3.2: Schematic diagram of LMN and NTN. LMN (ICAM-1 specific) and NTN (non-ICAM-1 specific) differ only in surface-conjugated targeting moiety.

Prior studies demonstrated that the number of targeting moieties on nanoparticles affected selectivity and targeting efficiency of nanoparticles in binding

to cells [31, 34]. In order to preferentially target ICAM-1 induced under inflammation but not basally expressed ICAM-1, an optimal ratio of I domain to nanoparticle was empirically determined (~100 molecules per nanoparticle [17]). When an SPR chip was prepared with varying ICAM-1 densities representing basal to high levels of ICAM-1 expression (200, 1000 and 3,250 molecules/ μm^2), LMN binding was limited to the surface coating with higher than normal ICAM-1 site density, while LMN binding to the basal ICAM-1 surface was the same as the background levels seen with NTN (Figure 3.3).

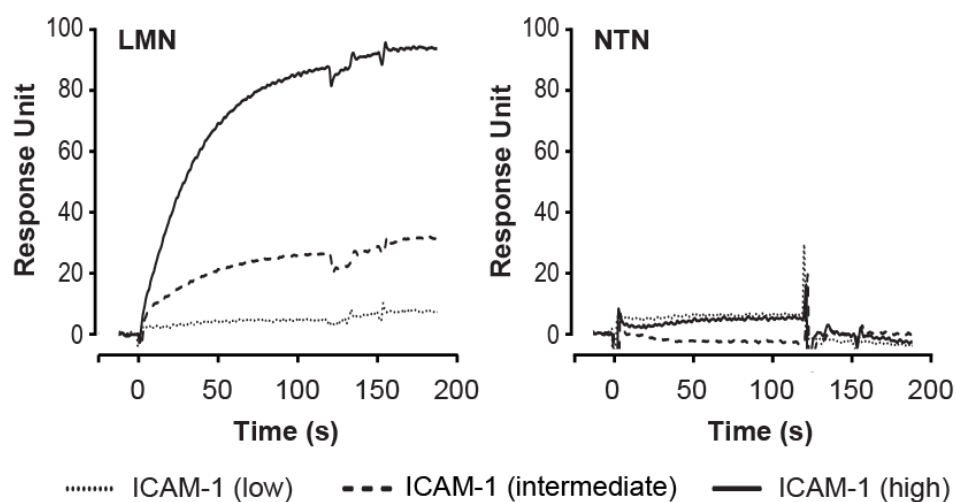


Figure 3.3: SPR measurement of the binding kinetics of LMN and NTN to varying concentrations of immobilized ICAM-1 (low, intermediate, and high correspond to approximately 200, 1000 and 3,250 molecules/ μm^2 , respectively). LMN binding was limited to the surface coating with higher than normal ICAM-1 site density, while LMN binding to the basal ICAM-1 surface was the same as the background levels seen with NTN.

To obtain qualitative assessment of nanoparticle biodistribution, we first imaged each mouse using near-IR optical fluorescence camera. Near-IR optical temporal mapping of the nanoparticle distribution demonstrated greater localization of LMN into the liver in mice treated with LPS (Figure 3.4 & 3.6). Control nanoparticles (NTN) also exhibited slightly higher accumulation into the liver of LPS-treated mice, which might be attributed to increased ICAM-1 independent phagocytic activity of immune cells or increased blood pool retention due to the inflammation in the liver. Higher fluorescence in the bladder was found to be due to some degree of shedding of

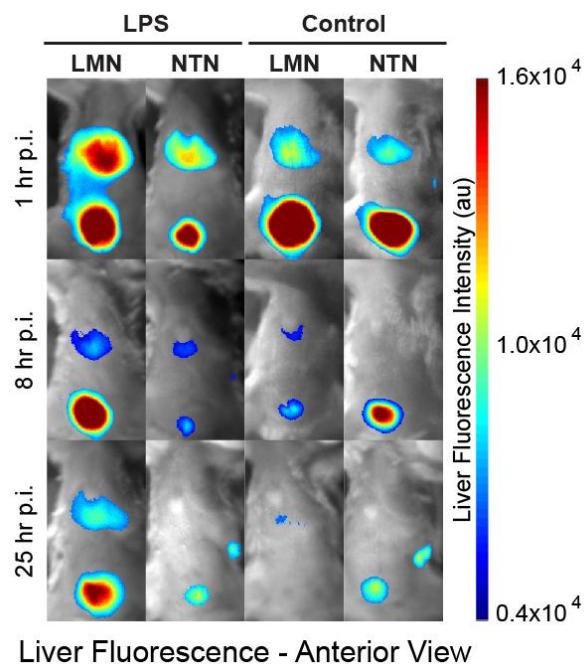


Figure 3.4: Fluorescent heat maps (color) are superimposed over brightfield images (grey scale), indicating greater nanoparticle localization in the liver in LPS/LMN-treated mice compared to that of negative controls, with observable localization diminishing over time.

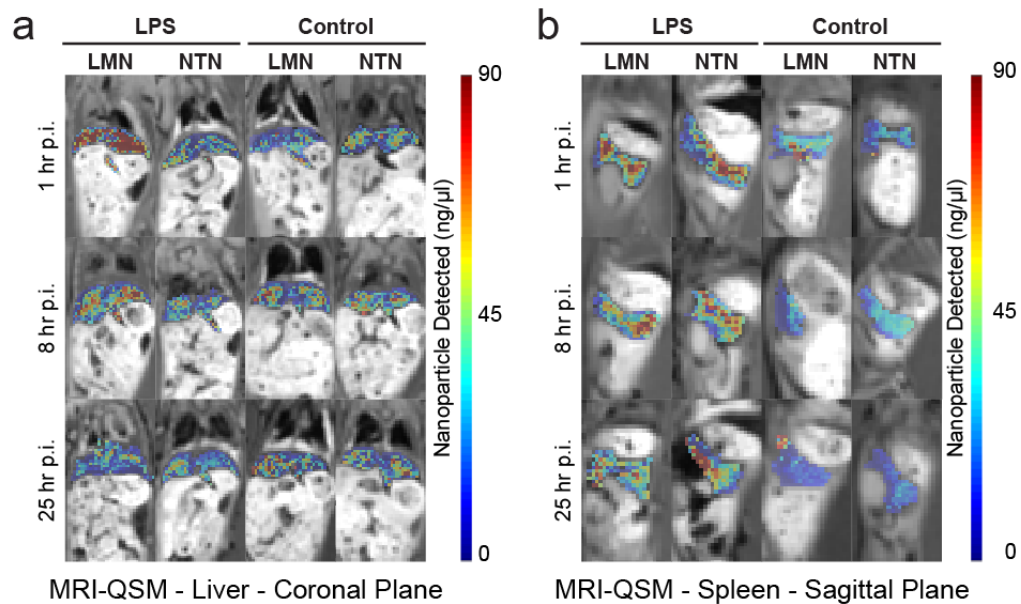


Figure 3.5: MRI-QSM reconstructions of the (a) liver and (b) spleen. QSM technique reveals greater nanoparticle localization in the liver of LMN/LPS-treated mice compared to that of negative controls, while greater nanoparticle localization is observed in the spleen in LPS-treated mice, regardless of injected nanoparticle. Portions of these results were previously described in Chen et al [31], and reproduced here. Representative QSM maps at each time point post-injection (p.i.) of nanoparticles are shown: organ-specific QSM heat maps (color) are superimposed over MRI T2* weighted EFGRE scans used for navigational reference (gray).

the I domains from the nanoparticles, which would be small enough to pass through glomerular capillaries in the kidney and collected into the bladder. After optical imaging, mice were sacrificed, transcardially perfused with PBS to remove nanoparticles in the blood, and subjected to MRI to quantitatively map nanoparticle distribution by QSM. Full body temporal mapping of the SPIO distribution was

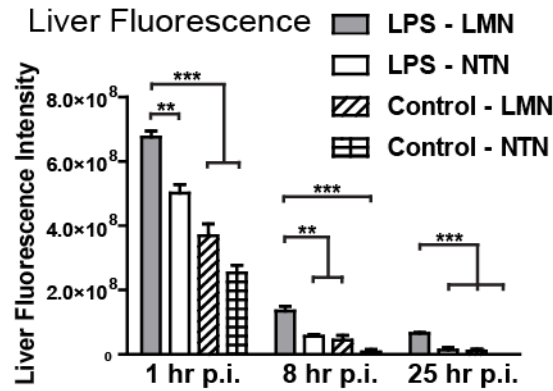


Figure 3.6: Fluorescence detected in the liver region of mice analyzed using near-IR optical imaging at 1, 8, and 25 hours post nanoparticle injection.

conducted and individual organs were segmented for analysis (Figure 3.5). Specific SPIO quantification of each organ revealed a greater localization of LMN in the liver compared to that of NTN in mice with LPS treatments (Figure 3.5a), peaking at one hour and progressively diminishing at each subsequent time point. In contrast to higher accumulation of NTN by optical imaging in the liver of LPS-treated mice (Figure 3.4), QSM quantification (Figure 3.5a & 3.7) and radioisotope measurement (Figure 3.8) performed after perfusion revealed that NTN accumulation in the liver was not augmented by LPS treatment, indicating that the higher fluorescence with LPS treatment is due to the increase in the blood pool retention of NTN. While the presence of LPS or the type of nanoparticles administered each independently influenced the magnitude of observable nanoparticle accumulation in the liver, the simultaneous interaction of LMN and LPS had a statistically significant effect in all measured time points (Table 3.1). In the spleen, higher amounts of nanoparticle accumulation were detected for LPS treated mice versus untreated controls, regardless

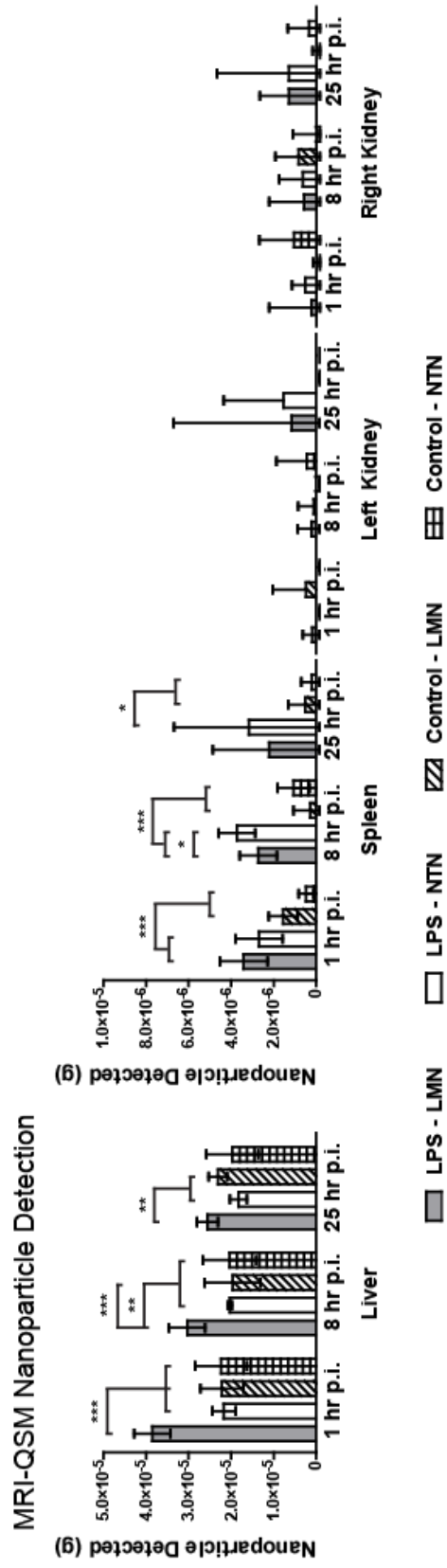


Figure 3.7: Measurement of nanoparticle accumulation in the liver, spleen, and kidneys from MRI-QSM analysis.

of the type of nanoparticles used (Figure 3.5b & 3.7). Therefore, LPS treatment was the predominant differentiating factor in observable nanoparticle accumulation in the spleen, independent of the targeting moiety or the interaction between LPS treatment and type of nanoparticle injected (Table 3.1). Negligible amounts of SPIO were detected in the kidneys, supporting the speculation that nanoparticles of ~ 60 nm in size [31] would be too large for renal filtration.

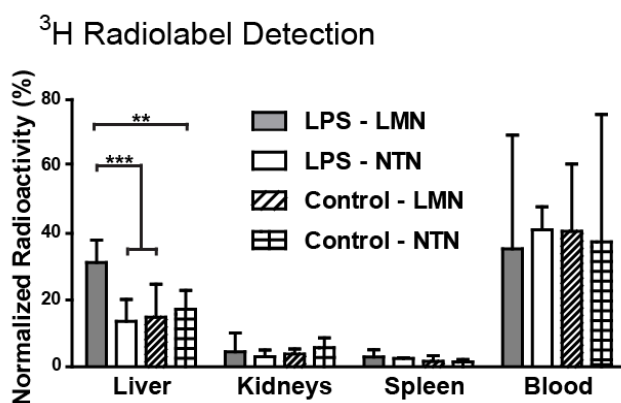


Figure 3.8: Radioactivity measurement of ^3H labeled nanoparticles from the liver, kidney, spleen, and blood 1 hour post-nanoparticle injection, normalized to the total counts of radioisotope decay per mouse. All modalities measured high liver-specific nanoparticle localization in LPS/LMN-treated mice 1 hour post nanoparticle injection over controls. QSM measured high spleen-specific nanoparticle localization in LPS-treated mice, regardless of nanoparticle injected. Trends persist through 25 hours post nanoparticle injection. Portions of these results were previously described in Chen et al [31], and reproduced here. One-way analysis of variance with Tukey HSD post-test at 95% confidence interval are summarized in each figure (*** $p < 0.001$, ** $0.001 < p < 0.01$, * $0.01 < p < 0.05$).

To further validate MRI quantification of nanoparticles, the values obtained with QSM technique were directly compared to those quantified by measuring

radioisotope decay of ^3H -labeled nanoparticles. Mice were treated with LPS for 12 hours and subsequently injected with ^3H -labeled LMN or NTN. At 1 hour post nanoparticle injection, blood was collected and after perfusion and sacrifice of the mice, organs were harvested. Radioactivities of the blood and major organs such as liver, kidney, and spleen were measured and normalized to the total radioactivity of each mouse in order to quantify percent nanoparticle biodistribution in the major organs (Figure 3.8). Highest radioactivity, irrespective of LMN vs. NTN and LPS vs. no treatment, was observed in the blood with a mean radioactivity of $\sim 40\%$, followed by the levels in the liver with significantly higher radioactivity detected in LPS/LMN-treated mice ($31.3 \pm 6.7\%$) than those in non-LPS/LMN-treated ($14.8 \pm 9.9\%$),

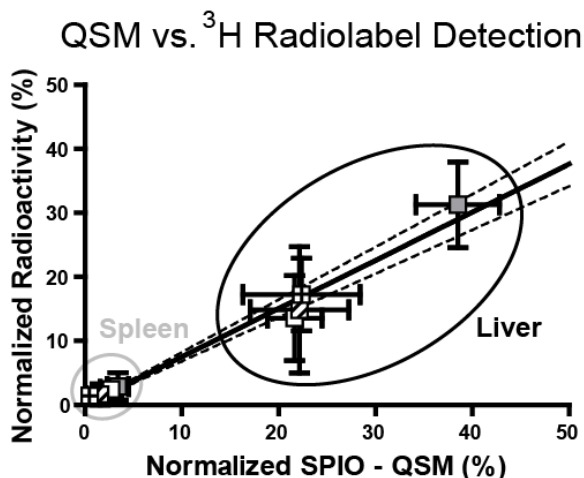


Figure 3.9: Measurements of nanoparticles in the spleen and liver obtained from by radioisotope measurement and by QSM are linearly related. Error bars indicate 95% confidence interval. Dotted line indicates 95% confidence interval for linear regression fitting. $n = 3$ for each treatment and imaging regimen.

Table 3.1: Two-way analysis of variance of organ-specific nanoparticle accumulation resulting from the treatment of LPS, the type of nanoparticle administered, or due to the interaction between both factors, quantified by QSM technique.

Factors	Liver			Spleen			Right Kidney			Left Kidney		
	1 hr	8 hr	25 hr	1 hr	8 hr	25 hr	1 hr	8 hr	25 hr	1 hr	8 hr	25 hr
LPS	***	**	ns	***	***	**	ns	ns	*	ns	ns	*
Nanoparticle	***	**	***	**	**	ns	ns	ns	ns	*	*	ns
Interaction	***	**	*	ns	ns	ns	ns	ns	ns	ns	*	ns

*** $p < 0.001$, ** $0.001 < p < 0.01$, * $0.01 < p < 0.05$, n.s. no significance.

LPS/NTN-treated ($13.6 \pm 6.6\%$), or non-LPS/NTN-treated controls ($17.2 \pm 5.7\%$). Significantly lower amounts (less than 10% of the total) were detected in the lung, kidney, and spleen (Figure 3.8 and not shown). Consistent with the QSM measurement of nanoparticle distribution in the spleen, slightly higher amounts of radioactivity were observed in the spleen of LPS-treated ($2.7 \pm 0.7\%$) than non-treated ($1.5 \pm 0.5\%$) mice. Values obtained by radioisotope measurement and by QSM showed overall an excellent linear relationship ($s_{y,x} = 1.60\%$), with QSM overestimating radioisotope measurements by approximately 25% (Figure 3.9).

In order to examine cellular basis for the increase in LMN accumulation into the liver in LPS-treated mice, selected liver tissues were stained for identification of different types of cells (hepatocyte, endothelium, and Kupffer cells) and localization of nanoparticles (Figure 3.10, 3.11 & 3.12). Vasculature dilatation was apparent in LPS-treated liver tissue (Figure 3.10) with LMN deposited primarily on endothelial cells and Kupffer cells (Figure 3.11). Simultaneous detection of Kupffer cells (CD68)

and nanoparticles by Prussian Blue staining revealed that most large deposits of LMN were accumulated into Kupffer cells (Figure 3.12), implying that higher accumulation of LMN over NTN in the liver of LPS-treated mice is mainly due to ICAM-1 induction and uptake by Kupffer cells.

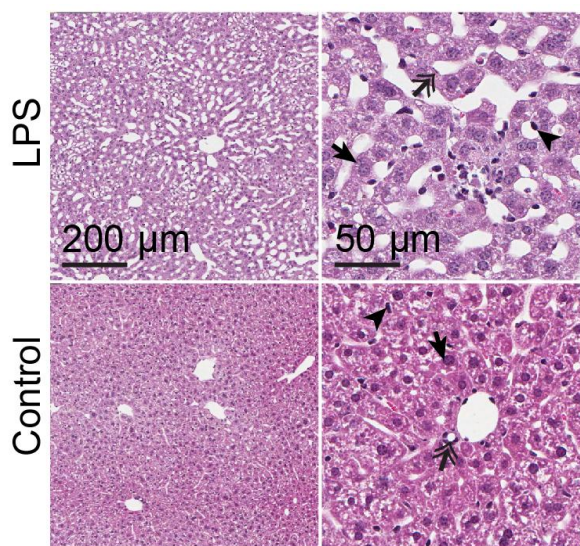


Figure 3.10: H&E stain of liver tissue sections show distinct dilation of liver tissue, characteristic of sepsis.

3.5 Discussion

With developments in quantitative MRI techniques, this study presents a clinically adaptable method for organ-level mapping of inflammation by quantifying the susceptibility of SPIO-based contrast agents, a measure directly proportional to SPIO concentration. While existing methods for detecting inflammation exist in the context of sepsis diagnosis, such detection methods typically rely on bulk measurements of the presence of pathogens, blood-borne cytokines, and other

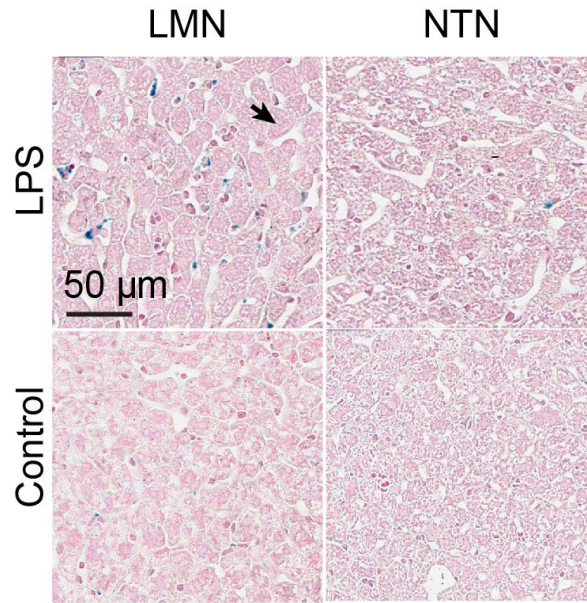


Figure 3.11: Prussian Blue staining of liver tissue sections shows SPIO accumulation primarily in the endothelial cells and Kupffer cells, with markedly more staining in LPS treated subjects with injected LMN.

inflammatory markers, lacking in the spatiotemporal progression and detection of inflammation locally in the body. Central to inflammation is the adhesion of leukocytes to vascular endothelium, a process mediated by molecular interactions between cell adhesion molecules such as integrins and ICAM-1. Toward a sensitive molecular imaging of inflammation, we designed nanoparticles to mimic the ability of leukocyte to preferentially adhere to inflamed vasculature, which was achieved by attaching the high affinity I domain of LFA-1 to nanoparticles. Despite the fact that ICAM-1 is basally expressed in many different types of cells including endothelium and immune cells, our nanoparticles were shown to be selective to vasculature under inflammation with upregulated ICAM-1 expression [31]. Capable of *in vivo* detection

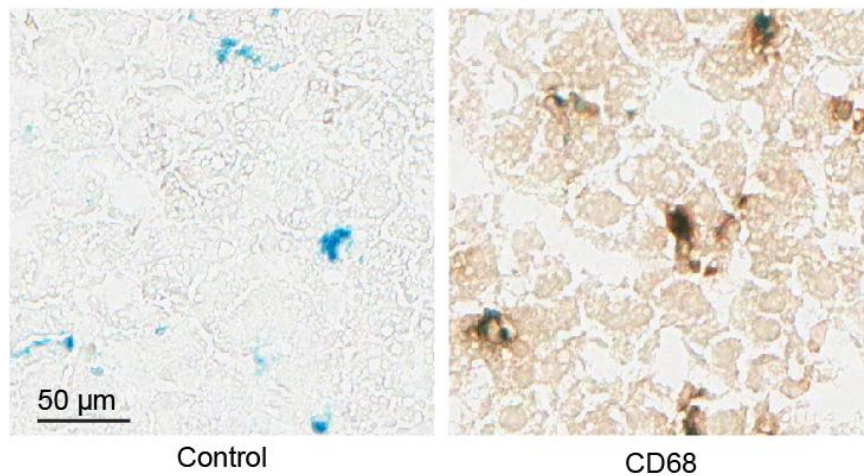


Figure 3.12: CD68 (brown) and Prussian Blue (blue) staining indicates primary localization of iron deposition in Kupffer cells. Examples of hepatocytes (arrow), endothelium (double headed arrow), and Kupffer cells (arrowhead) are marked.

by optical imaging and MRI techniques, leukocyte-mimetic nanoparticle has previously been shown to specifically localize to the areas of acutely induced local inflammation and to the vasculature within and in the vicinity of the tumor growth, providing spatial and temporal insight into various inflammation-related diseases and conditions. In this study, we demonstrated the potential use of LMN as a bimodal diagnostic agent for the early detection of sepsis or systemic inflammatory response using quantitative MRI techniques.

Previously, we have described a tunable approach to creating nanoparticles that mimic an intrinsic behavior of leukocytes that bind selectively to inflammatory sites [17]. By modulating the affinity and avidity of surface-bound I domains for targeting inflammation, we were able to construct nanoparticles that can resist thermal diffusion and detachment forces exerted by fluid-induced shear stress, while allowing little

binding to cells with only basal levels of ICAM-1 expression. Approximately 100 I domains were conjugated to the surface of each LMN, roughly comparable to that of a surface density-optimized approach to ICAM-1 specific nanoparticle design [17, 34]. While prior approaches have demonstrated the appeal of employing both selectin ligands and anti-ICAM-1 antibodies to more accurately mimic the rolling and adhesion characteristics of leukocytes [35-36], we chose to utilize as the targeting moiety for LMN the I domain of LFA-1 integrin, which has been engineered to engage with ICAM-1 with high affinity without prior dependence on interaction with selectins. We found that a targeting moiety derived from physiological molecules, optimized for affinity and avidity, gave superior selectivity and targeting efficiency to inflamed cells in *in vitro* and *in vivo* settings [17, 31].

In treating mice with ICAM-1-specific LMN, we were able to readily differentiate between mice, either pre-treated with LPS or left untreated, by quantitatively measuring nanoparticle localization in various abdominal organs in each of the subjects. This differential effect is most apparent when measuring nanoparticle localization in the liver; a temporal mapping of nanoparticle distribution through MRI QSM demonstrated significantly greater localization of LMN into the liver of sepsis-induced mice compared to that of non-septic subjects, or of those treated with ICAM-1 independent NTN. The observed differences by QSM, corroborated qualitatively by near-IR optometry, were most pronounced one hour after the treatment of nanoparticles, gradually decaying over time while persisting through at least 24 hours after nanoparticle injection. While particles of ~100 nm in diameter in systemic circulation may accumulate in the liver regardless of targeting moiety due to

phagocytic activity of immune cells within the liver, the ICAM-1 specificity conferred by the surface conjugation of high affinity I domain (F265S/F292G) of LFA-1 on LMN led to a close to a 2-fold increase in the accumulation in the liver to enable quantitative differentiation. NTN nanoparticles, conjugated with the same LFA-1 I domain but with an inactivating mutation, D137A, did not exhibit higher accumulation into the inflamed liver. This observation was corroborated through histology using iron staining of tissue sections of the liver, revealing a greater degree of nanoparticle accumulation in LPS-treated LMN cases with specific staining observed in both endothelial cells and Kupffer cells with the most significant nanoparticle accumulations co-localized in the Kupffer cells. Thus, while ICAM-1 is basally expressed in all endothelium and utilizing it as a molecular target for inflammation and sepsis imaging techniques may lead to a background signal, it was found that this background binding was negligible, judging from no difference between LMN and NTN accumulations into the liver by radioactivity measurement and QSM. The relationship between LMN biodistribution independent of ICAM-1 expression can be further characterized through the use of ICAM-1 knockout mice or through the use of blocking antibodies to systemically eliminate available ICAM-1 binding sites.

A high degree of nanoparticle localization was also observed in the spleen of LPS-treated mice through optical imaging and QSM. However, unlike the observations in the liver, increases in nanoparticle accumulations to the spleen were observed in all LPS-treated subjects, regardless of the targeting moiety employed, suggesting that localization is a result of phagocytic activity rather than ICAM-1 biospecificity. Severe and pervasive inflammation, such as that prompted by LPS-

induced systemic endotoxic shock, may result in increased phagocytic uptake of nanoparticles in areas in the immediate proximity of major monocyte sources in the spleen, an organ that functions as a major reservoir for undifferentiated monocytes before inflammation-initiated recruitment [37], and is responsible for the release of splenic lymphokines necessary for the increase of phagocytic activity of macrophages cells in response to inflammatory stimuli [38-40]. While studies have indicated high ICAM-1 expression in the epithelial cells of the lungs due to endotoxin-induced inflammation [41-42], MRI-based techniques such as QSM cannot quantitatively differentiate between signal voids resulting from SPIO-based spin dephasing and signal voids created by air. This difficulty with reliably differentiating QSM-based quantification of SPIO deposits and air may be overcome by multiple data acquisition at differing magnetic field strengths [43].

Using radiolabeled SPIO nanoparticles, we were able to provide a quantitative mapping of nanoparticle distribution by the measurement of radioactivity and at the same time clinically relevant QSM technique based on MRI. At one hour post nanoparticle injection, QSM determined that ~39% of injected nanoparticles were localized into the liver of LPS/LMN mice, a value 70% greater than that of negative controls. In comparison, radioisotope quantification found ~31% of the total body radioactivity was located in the liver of LPS/LMN treated mice, a value 81% greater than that of negative controls. However, some difference in QSM quantification vs. radioactivity measurement of nanoparticles was unavoidable as it was found that the lipid layer outside of SPIO was subject to some degree of shedding during circulation. This may explain, in the course of optical imaging, varying degrees of fluorescence

(conjugated to the I domains) observed in the bladder of each subject, regardless of the nanoparticle targeting moiety. The decoupling of the fluorescence or protein from nanoparticles was found to be caused by shedding of the phospholipid lipid layer from SPIO or lipid degradation by phospholipase activity in the plasma, but not due to dissociation between His tag and Ni-NTA, judging from a dramatic decrease in decoupling when crosslinkable fatty acids were used to cage SPIO (data not shown).

Sepsis represents a continuum in clinical-pathologic severity with definable phases that characterize patients at risk for increased mortality. Current diagnosis techniques have limited windows of detection and may rely on transient biology and physiological conditions that may not persist across all phases of sepsis progression. Moreover, the onset of sepsis can be linked to a widely heterogeneous set of initial risk factors, further complicating diagnosis and delaying treatment. In particular, the endothelium is crucial in regulating a local balance between pro-inflammatory and anti-inflammatory mediators; under sepsis, endothelium undergoes excessive, sustained, and generalized activation, resulting in unregulated expression of inflammation-associated products. Among these, adhesion molecule ICAM-1 has been implicated as a highly localized biomarker for inflammation induced under organ damage [23-25], one of the most significant mortality risks in septic patients [6]. By specifically targeting ICAM-1 using bimodal LMN, we were able to readily differentiate septic and non-septic mice using optical imaging and quantitative MRI techniques, both non-invasive modalities. Most significantly, the observed differences were pronounced as soon as one hour after the treatment of the nanoparticle, and persist through at least 25 hours after injection. In this study, our temporal mapping of

inflammation was focused on following nanoparticle distribution over 25 hours in mice exposed to LPS for 12 hours. However, as surface-expressed ICAM-1 is induced rapidly under inflammation, with some studies observing peak expression as quickly as 1-2 hours after the introduction of stimuli [20], additional information on spatiotemporal dynamics of inflammation can be obtained by subjecting mice to different durations of LPS while maintaining similar post-treatment imaging protocols. Such information on spatiotemporal dynamics of inflammation would be necessary to better understand the distinct yet common processes of inflammation in reticuloendothelial systems such as the liver and spleen.

This study also reveals the strength of MRI QSM in quantitatively measuring contrast agent localization into specific structures within the body. While optical imaging provides a gross view of the overall biodistribution of a fluorescent marker, the results are coarse, qualitative in nature, and prone to confounding effects due to the relatively shallow penetration depth of common fluorescent wavelengths, and the technique is not ideal for most clinical applications. Alternatively, traditional MRI techniques, such as typical T2* weighted imaging, provide significantly greater spatial resolution, but visualization is hindered by large obscuring signal voids resulting from SPIO use, and the resulting images are largely qualitative in nature, making it difficult to precisely estimate SPIO localization. In contrast, QSM technique offers a quantitative, high resolution method of tracking the biodistribution of paramagnetic contrast agents to specific organs and structures through mapping of magnetic susceptibility, a physical property of paramagnetic materials that relates linearly to its concentration, allowing for direct determination of the amount and spatial location of

contrast agent accumulation. Moreover, while SPIO-based contrast agents may result in signal voids in traditional T2* imaging and obscured underlying structure, QSM reconstruction techniques enable unimpeded analysis of the distribution of contrast agent and spatiotemporal mapping of inflammation. Given the speed and robustness by which these differences can be observed after administration of LMN, this technique offers temporal flexibility ideal for clinical applications, while granting dramatically increased spatial fidelity not offered by existing bulk measurement diagnostic techniques.

REFERENCES

- [1] Nathan C, Ding A. Nonresolving inflammation. *Cell*. 2010;140:871-82.
- [2] Nathan C. Points of control in inflammation. *Nature*. 2002;420:846-52.
- [3] Corti R, Hutter R, Badimon JJ, Fuster V. Evolving concepts in the triad of atherosclerosis, inflammation and thrombosis. *J Thromb Thrombolysis*. 2004;17:35-44.
- [4] Wellen KE, Hotamisligil GS. Obesity-induced inflammatory changes in adipose tissue. *J Clin Invest*. 2003;112:1785-8.
- [5] Coussens LM, Werb Z. Inflammation and cancer. *Nature*. 2002;420:860-7.
- [6] Aird WC. The role of the endothelium in severe sepsis and multiple organ dysfunction syndrome. *Blood*. 2003;101:3765-77.
- [7] Nathan C, Sporn M. Cytokines in context. *The Journal of cell biology*. 1991;113:981-6.
- [8] Buckley CD, Pilling D, Lord JM, Akbar AN, Scheel-Toellner D, Salmon M. Fibroblasts regulate the switch from acute resolving to chronic persistent inflammation. *Trends Immunol*. 2001;22:199-204.
- [9] Barnes PJ. Immunology of asthma and chronic obstructive pulmonary disease. *Nat Rev Immunol*. 2008;8:183-92.
- [10] Deitch EA. Multiple organ failure. Pathophysiology and potential future therapy. *Ann Surg*. 1992;216:117-34.
- [11] McAteer MA, Akhtar AM, von Zur Muhlen C, Choudhury RP. An approach to molecular imaging of atherosclerosis, thrombosis, and vascular inflammation using microparticles of iron oxide. *Atherosclerosis*. 2010;209:18-27.

- [12] Jaffer FA, Tung CH, Wykrzykowska JJ, Ho NH, Houg AK, Reed GL, et al. Molecular imaging of factor XIIIa activity in thrombosis using a novel, near-infrared fluorescent contrast agent that covalently links to thrombi. *Circulation*. 2004;110:170-6.
- [13] Wilson MS, Wynn TA. Pulmonary fibrosis: pathogenesis, etiology and regulation. *Mucosal Immunol*. 2009;2:103-21.
- [14] Lanza GM, Yu X, Winter PM, Abendschein DR, Karukstis KK, Scott MJ, et al. Targeted antiproliferative drug delivery to vascular smooth muscle cells with a magnetic resonance imaging nanoparticle contrast agent: implications for rational therapy of restenosis. *Circulation*. 2002;106:2842-7.
- [15] Massey JM, Amps J, Viapiano MS, Matthews RT, Wagoner MR, Whitaker CM, et al. Increased chondroitin sulfate proteoglycan expression in denervated brainstem targets following spinal cord injury creates a barrier to axonal regeneration overcome by chondroitinase ABC and neurotrophin-3. *Exp Neurol*. 2008;209:426-45.
- [16] Nahrendorf M, Jaffer FA, Kelly KA, Sosnovik DE, Aikawa E, Libby P, et al. Noninvasive vascular cell adhesion molecule-1 imaging identifies inflammatory activation of cells in atherosclerosis. *Circulation*. 2006;114:1504-11.
- [17] Kang S, Park T, Chen X, Dickens G, Lee B, Lu K, et al. Tunable physiologic interactions of adhesion molecules for inflamed cell-selective drug delivery. *Biomaterials*. 2011;32:3487-98.
- [18] Muro S, Gajewski C, Koval M, Muzykantov VR. ICAM-1 recycling in endothelial cells: a novel pathway for sustained intracellular delivery and prolonged effects of drugs. *Blood*. 2005;105:650-8.
- [19] Park S, Kang S, Veach AJ, Vedvyas Y, Zarnegar R, Kim JY, et al. Self-assembled nanoplatform for targeted delivery of chemotherapy agents via affinity-regulated molecular interactions. *Biomaterials*. 2010;31:7766-75.

- [20] Almenar-Queralt A, Duperray A, Miles LA, Felez J, Altieri DC. Apical topography and modulation of ICAM-1 expression on activated endothelium. *Am J Pathol.* 1995;147:1278-88.
- [21] Dustin ML, Rothlein R, Bhan AK, Dinarello CA, Springer TA. Induction by IL 1 and interferon-gamma: tissue distribution, biochemistry, and function of a natural adherence molecule (ICAM-1). *J Immunol.* 1986;137:245-54.
- [22] Essani NA, Fisher MA, Farhood A, Manning AM, Smith CW, Jaeschke H. Cytokine-induced upregulation of hepatic intercellular adhesion molecule-1 messenger RNA expression and its role in the pathophysiology of murine endotoxin shock and acute liver failure. *Hepatology.* 1995;21:1632-9.
- [23] Farhood A, McGuire GM, Manning AM, Miyasaka M, Smith CW, Jaeschke H. Intercellular adhesion molecule 1 (ICAM-1) expression and its role in neutrophil-induced ischemia-reperfusion injury in rat liver. *Journal of leukocyte biology.* 1995;57:368-74.
- [24] Olanders K, Sun Z, Borjesson A, Dib M, Andersson E, Lason A, et al. The effect of intestinal ischemia and reperfusion injury on ICAM-1 expression, endothelial barrier function, neutrophil tissue influx, and protease inhibitor levels in rats. *Shock.* 2002;18:86-92.
- [25] Volpes R, van den Oord JJ, Desmet VJ. Immunohistochemical study of adhesion molecules in liver inflammation. *Hepatology.* 1990;12:59-65.
- [26] Werner J, Z'Graggen K, Fernandez-del Castillo C, Lewandrowski KB, Compton CC, Warshaw AL. Specific therapy for local and systemic complications of acute pancreatitis with monoclonal antibodies against ICAM-1. *Ann Surg.* 1999;229:834-40; discussion 41-2.

- [27] Denis MC, Mahmood U, Benoist C, Mathis D, Weissleder R. Imaging inflammation of the pancreatic islets in type 1 diabetes. *Proc Natl Acad Sci U S A*. 2004;101:12634-9.
- [28] Jin M, Song G, Carman CV, Kim YS, Astrof NS, Shimaoka M, et al. Directed evolution to probe protein allostery and integrin I domains of 200,000-fold higher affinity. *Proc Natl Acad Sci U S A*. 2006;103:5758-63.
- [29] Marlin SD, Springer TA. Purified intercellular adhesion molecule-1 (ICAM-1) is a ligand for lymphocyte function-associated antigen 1 (LFA-1). *Cell*. 1987;51:813-9.
- [30] Angus DC, Linde-Zwirble WT, Lidicker J, Clermont G, Carcillo J, Pinsky MR. Epidemiology of severe sepsis in the United States: analysis of incidence, outcome, and associated costs of care. *Crit Care Med*. 2001;29:1303-10.
- [31] Chen X, Wong R, Khalidov I, Wang AY, Leelawattanachai J, Wang Y, et al. Inflamed leukocyte-mimetic nanoparticles for molecule imaging of inflammation. *Biomaterials*. 2011;32:7651-61.
- [32] Liu T, Spincemaille P, de Rochefort L, Kressler B, Wang Y. Calculation of susceptibility through multiple orientation sampling (COSMOS): a method for conditioning the inverse problem from measured magnetic field map to susceptibility source image in MRI. *Magn Reson Med*. 2009;61:196-204.
- [33] Eniola AO, Willcox PJ, Hammer DA. Interplay between rolling and firm adhesion elucidated with a cell-free system engineered with two distinct receptor-ligand pairs. *Biophys J*. 2003;85:2720-31.
- [34] Haun JB, Hammer DA. Quantifying nanoparticle adhesion mediated by specific molecular interactions. *Langmuir*. 2008;24:8821-32.
- [35] Eniola AO, Hammer DA. Characterization of biodegradable drug delivery vehicles with the adhesive properties of leukocytes II: effect of degradation on targeting activity. *Biomaterials*. 2005;26:661-70.

- [36] Omolola Eniola A, Hammer DA. In vitro characterization of leukocyte mimetic for targeting therapeutics to the endothelium using two receptors. *Biomaterials*. 2005;26:7136-44.
- [37] Swirski FK, Nahrendorf M, Etzrodt M, Wildgruber M, Cortez-Retamozo V, Panizzi P, et al. Identification of splenic reservoir monocytes and their deployment to inflammatory sites. *Science*. 2009;325:612-6.
- [38] Billiar TR, West MA, Hyland BJ, Simmons RL. Splenectomy alters Kupffer cell response to endotoxin. *Arch Surg*. 1988;123:327-32.
- [39] Nogueira N, Cohn ZA. *Trypanosoma cruzi*: in vitro induction of macrophage microbicidal activity. *J Exp Med*. 1978;148:288-300.
- [40] Van Snick J. Interleukin-6: an overview. *Annu Rev Immunol*. 1990;8:253-78.
- [41] Panes J, Perry MA, Anderson DC, Manning A, Leone B, Cepinskas G, et al. Regional differences in constitutive and induced ICAM-1 expression in vivo. *Am J Physiol*. 1995;269:H1955-64.
- [42] Burns AR, Takei F, Doerschuk CM. Quantitation of ICAM-1 expression in mouse lung during pneumonia. *J Immunol*. 1994;153:3189-98.
- [43] Liu T, Spincemaille P, de Rochefort L, Wong R, Prince M, Wang Y. Unambiguous identification of superparamagnetic iron oxide particles through quantitative susceptibility mapping of the nonlinear response to magnetic fields. *Magn Reson Imaging*. 2010;28:1383-9.
- [44] Hu X, Kang S, Chen X, Shoemaker CB, Jin MM. Yeast surface two-hybrid for quantitative in vivo detection of protein-protein interactions via the secretory pathway. *J Biol Chem*. 2009;284:16369-76.

CHAPTER 4

NOVEL STRATEGY FOR SELECTION OF MONOCLONAL ANTIBODIES AGAINST HIGHLY CONSERVED ANTIGENS: PHAGE LIBRARY PANNING AGAINST EPHRIN-B2 DISPLAYED ON YEAST

Published in *Plos One*³

4.1 Abstract

Ephrin-B2 is predominately expressed in endothelium of arterial origin, involved in developmental angiogenesis and neovasculature formation through its interaction with EphB4. Despite its importance in physiology and pathological conditions, it has been challenging to produce monoclonal antibodies against ephrin-B2 due to its high conservation in sequence throughout human and rodents. Using a novel approach for antibody selection by panning a phage library of human antibody against antigens displayed in yeast, we have isolated high affinity antibodies against ephrin-B2. The function of one high affinity binder (named as ‘EC8’) was manifested in its ability to inhibit ephrin-B2 interaction with EphB4, to cross-react with murine ephrin-B2, and to induce internalization into ephrin-B2 expressing cells. EC8 was also compatible with immunoprecipitation and detection of ephrin-B2 expression in the tissue after standard chemical fixation procedure. Consistent with previous reports on

³ This chapter is modified with the permission of the publisher from Gu X, Vedvyas Y, Chen X, Kaushik T, Hwang CI, Hu X, Nikitin AY, Jin MM. Novel strategy for selection of monoclonal antibodies against highly conserved antigens: phage library panning against ephrin-B2 displayed on yeast. *Plos One*. 2012. Gu X, Vedvyas Y and Chen X contribute equally. Xiaoyue Chen conducted the experiments, analyzed the data and wrote the paper with regard to the following figures: 4.1b, 4.2b, 4.7a, 4.8 & 4.9.

ephrin-B2 induction in some epithelial tumors and tumor-associated vasculatures, EC8 specifically detected ephrin-B2 in tumors as well as the vasculature within and outside of the tumors. We envision that monoclonal antibody developed in this study may be used as a reagent to probe ephrin-B2 distribution in normal as well as in pathological conditions and to antagonize ephrin-B2 interaction with EphB4 for basic science and therapeutic applications.

4.2 Introduction

The erythropoietin-producing hepatocellular (Eph) receptors and their ligands, ephrins comprise the largest subfamily of receptor tyrosine kinases (RTK), playing an important role in physiology such as embryogenesis, organ development, and angiogenesis as well as implicated in several types of cancers [1]. Among different classes of ephrins, ephrin-B2 is primarily expressed in arterial endothelial cells and neovasculature, forming a bidirectional signal with its cognate receptor EphB4, which is mainly expressed in venous endothelial cell [2-3]. The importance of such interaction in a developmental process has been demonstrated by impaired angiogenesis and ultimately embryonic lethality in mice due to homozygous mutation of ephrin-B2 or EphB4 [3-6]. The role of EphB4 and ephrin-B2 also extends to tumor growth and angiogenesis [1, 7]. Inhibition of their interaction by EphB4 antibody or extracellular fragment of EphB4 can inhibit tumor angiogenesis and tumor growth [8-10]. Ephrin-B2 is involved in vascular endothelial growth factor (VEGF) signaling, through the internalization of VEGF receptor in all endothelial cell types during physiological and pathological angiogenesis [11-13], and could be upregulated in

VEGF-treated endothelial cells [5-6]. Expression of ephrin-B2 along with EphB4 was found to be higher in many tumors including colorectal, breast, ovarian, and lung, serving as a poor prognostic marker [14-18].

Despite the importance of ephrin-B2 in physiology and pathological conditions, there are no widely available monoclonal antibodies against ephrin-B2, likely attributed to the fact that immune system in rodents prevents responses to self antigen or to highly conserved human antigens. To overcome the problem with generating antibodies against highly conserved antigens, mice with impaired immune tolerance (*e.g.* NZB/W) have been exploited [19-20]; however, concerns remain on this alternative approach due to the observations of multi-specificity and low-affinity on auto-antibodies developed from autoimmune mice [20]. In order to generate antibodies against highly conserved ephrin-B2, we used phage display of single chain human antibody and screened them against ephrin-B2 expressed in yeast. From our previous work [21], we found that phage panning against antigens displayed in yeast is highly efficient in rapid enrichment of specific phage clones, obviating the need to produce soluble antigens as well as ensuring native conformation. With newly developed monoclonal antibody, we found that tumors of colon, breast, ovary, and lung upregulated ephrin-B2 compared to respective normal tissues. Antibody staining was also observed in the neovasculature within the tumor, corresponding to new vessel sprouts. Our antibody also exhibited properties such as its ability to cross-react with murine ephrin-B2, to inhibit EphB4 binding, and to be internalized into cells after binding to ephrin-B2. We anticipate that antibodies developed in this study will be useful in probing ephrin-B2 distribution in normal and disease processes, and in

antagonizing the interaction between ephrin-B2 and EphB4 for scientific and therapeutic applications.

4.3 Materials and methods

4.3.1 Selection and expression of ephrin-B2-specific scFvs

A part of human ephrin-B2 ectodomain (Thr-22 to Gly-165) was cloned into yeast surface display vector, CAga2 (a modified version of PCTCON [30]), and transformed into yeast strain EBY100 by EZ-transformation kit (Zymo Research). Yeast culture and protein induction were performed as previously described [30]. Proteins displayed on yeast contain ephrin-B2 ectodomain, Myc tag, and Aga2 from N- to C-terminal. Surface expression of ephrin-B2 in yeast was measured by immunofluorescence flow cytometry using mouse anti-Myc antibody (9E10, Santa Cruz Biotechnology) followed by goat phycoerythrin-conjugated anti-mouse antibody (Santa Cruz Biotechnology), as well as by recombinant human EphB4-Fc chimera (Biomiga) followed by goat phycoerythrin-conjugated anti-human antibody (Santa Cruz Biotechnology). A phage library of human single chain variable fragment (scFv) antibody with 10^8 diversity (Tomlinson I + J, Source BioScience) was panned against ephrin-B2 expressing-yeast cells, following a procedure previously described [21]. Briefly, 2×10^{13} phage clones were first incubated with phosphate buffered saline (PBS) containing 2% nonfat dry milk (Carnation) for 30 min at room temperature (RT), to which 2×10^7 yeast cells expressing unrelated protein (Zif268) was added for depletion of non-specific phage binders. The mixture of phage and yeast cells were then incubated for 1 h at RT with agitation. Non-binding phage clones in the

supernatant were removed after centrifugation to pellet yeast cells, which were subsequently washed five times with PBS/0.05% Tween 20. Then phage particles were eluted from yeast cells with trypsin and used to infect *Escherichia coli* (TG1) to amplify enriched phage library for the next round of selection. After three rounds of selection, ~200 TG1 clones were picked to produce individual phage clones. The binding of phage clones to ephrin-B2 expressing yeast cells was measured by immunofluorescence flow cytometry using anti-His tag antibody (Sigma-Aldrich) followed by goat phycoerythrin-conjugated anti-mouse antibody (Santa Cruz Biotechnology).

4.3.2 Expression of scFv

Individual phage clones with high affinity binding to ephrin-B2 were sequenced, and selected scFv antibodies were solubly expressed from bacteria HB2151 (Clontech). Transformed HB2151 cells were grown at $OD_{600} = 0.4$, to which 1 mM isopropyl β -D-1-thiogalactopyranoside was added. Cells were induced to express protein at 25 °C by culturing for 16 h with shaking at 250 rpm. After induction, cells were spun down, resuspended in binding buffer (50 mM sodium phosphate, pH 8.0, 300 mM sodium chloride, and 10 mM imidazole), sonicated to break the cell wall, and were spun at 10,000 g for 15 min to remove cell debris. Proteins in the supernatant were purified with Ni-NTA column followed by gel filtration chromatography using Superdex 75 column connected to AKTA Purifier (GE Healthcare). The purity and the size of proteins were confirmed by sodium dodecyl sulfate (SDS) polyacrylamide gel electrophoresis (PAGE).

4.3.3 Cell culture

Chinese hamster ovary (CHO) cells [30] were maintained in Ham's F12 medium (Invitrogen) supplemented with 2 mM L-glutamine and 5% fetal bovine serum (FBS). Colorectal adenocarcinoma COLO205 [31] were cultured in RPMI 1640 medium supplemented with 2 mM L-glutamine, 10% FBS and 1% Penicillin-Streptomycin. HCT116 colon cancer cell line [32] was grown in McCoy's 5A Medium (Invitrogen) supplemented with 10% FBS. Human embryonic kidney (HEK) 293T cells [30] were maintained in advanced DMEM supplemented with 10% FBS, 2 mM L-glutamine, 20 µg/mL hygromycin and 1% Penicillin-Streptomycin. All cell cultures were maintained at 37 °C in a humidified 5% CO₂ atmosphere. 293T cells stably expressing ephrin-B2 were established by transfection of cells with pcDNA3.1 (Invitrogen) containing full-length ephrin-B2 with 200 µg/ml of hygromycin for selection.

4.3.4 Immunofluorescence flow cytometry

Protein expression on yeast cell surface was analyzed by flow cytometry as described [33]. Briefly, yeast cells were incubated with primary antibodies (10 µg/ml) in 200 µl of labeling buffer (PBS/0.5% bovine serum albumin) for 1 h with shaking at 30°C. Cells were then washed and incubated with secondary antibodies in 200 µl of labeling buffer for 1 h at RT. After washing, cells were resuspended in 200 µl of labeling buffer and subjected to flow cytometry. The expression of ephrin-B2 in mammalian cells was detected by incubating cells with ephrin-B2 antibody for 1 h at 4 °C, followed by Alexa Fluor 488 (AF488)-conjugated goat anti-human secondary antibody (Invitrogen). Flow cytometry was performed on a FACSCalibur (BD Biosciences) and analyzed with CellQuest software (BD Biosciences).

4.3.5 Conversion of scFv into scFv-Fc

In order to fuse scFv into immunoglobulin G (IgG) constant region (Fc) including a hinge sequence, scFv sequence followed by IgG1 Fc was cloned into pcDNA3.1. scFv-Fc fusion protein was expressed in 293T cells and purified with Protein A beads (Thermo Scientific).

4.3.6 Conformation specificity and selectivity of EC8 against ephrin-B2

Yeast cells expressing ephrin-B2 were incubated either in 50 mM Tris buffer (pH 8.0) containing 6 M guanidine hydrochloride for 20 min at room temperature, or in labeling buffer (PBS/0.5% bovine serum albumin) heated to 80 °C for 10 min, to denature ephrin-B2. EC8 or EphB4-Fc binding to yeast cells after denaturation of ephrin-B2 was then measured by flow cytometry. To examine crossreactivity of EC8 to other ephrins, human ephrin-B1 (Leu-24 to Gly-165) and ephrin-A5 (Pro-22 to Gly-169) ectodomains were cloned and displayed on yeast surface. Immunofluorescence flow cytometry was conducted with mouse anti-Myc antibody (9E10, Santa Cruz Biotechnology), recombinant human EphB2/Fc chimera (R&D Systems), and EC8 followed by respective secondary antibodies as previously described.

4.3.7 Competition assay

Yeast cells expressing ephrin-B2 were incubated with varying concentrations of mAb EC8 or affinity (protein A column, Pierce) purified human IgG for 20 min at 30 °C, to which recombinant human EphB4 containing His-tag at C-terminal (R&D Systems) was added at 100 nM and incubated for 20 min at 30 °C. The binding of EphB4 to yeast was detected by flow cytometry using anti-His tag antibody, followed

by phycoerythrin-conjugated goat anti-mouse antibody.

4.3.8 Immunoprecipitation of ephrin-B2 by mAb EC8

293T cells with stable expression of ephrin-B2 were incubated in lysis buffer (20 mM Tris-HCl, pH 8.0, 137 mM NaCl, 10% glycerol, 1% Triton X-100, 2 mM ethylenediaminetetraacetic acid (EDTA), protease inhibitor cocktail (Sigma)) for 30 min on ice. Cell debris were removed by centrifugation for 20 min at 14,000 g. Total protein lysate was precleared by Protein A beads for 1 h at 4 °C. After centrifugation, supernatants were collected and incubated with 10 µg/ml EC8 for 2 h at 4°C, followed by incubation with Protein A beads overnight at 4 °C. Immunoprecipitated proteins were run on SDS-polyacrylamide gel and transferred to polyvinyl difluoride membranes (Bio-Rad) for western blot analysis. The membrane was first blocked with 5% non-fat milk in TBS/0.05% Tween 20 for 1 h at RT, incubated with rabbit polyclonal anti-ephrin-B2 antibody (Genscript) overnight at 4 °C, and detected by horseradish peroxidase (HRP)-conjugated anti-rabbit antibody (Santa Cruz). ECL substrate (Pierce) was added to the membrane for 1 min at RT, which was exposed to X-ray film.

4.3.9 Immunofluorescence microscopy for ephrin-B2 labeling and internalization by EC8

Antibody labeling of ephrin-B2 was examined separately for cell-surface vs. internalized pool of ephrin-B2. 293T cells were grown on culture slides (BD Biosciences) to 50% confluence, to which 10 µg/ml of anti-ephrin-B2 antibody (EC8) was added. Cells were then incubated for 1 h at 37 °C to allow antibody binding and endocytosis to occur. To detect EC8 bound to cell surface ephrin-B2, cells were fixed

with 4% formaldehyde in PBS for 20 min at RT and incubated with blocking solution (PBS with 5% goat serum) for 1 h, followed by incubation with fluorescein-conjugated goat anti-human antibody (Invitrogen). Then to label internalized EC8, cells were permeabilized by 100% ice-cold methanol for 15 min on ice and incubated with blocking solution for 30 min at RT, followed by incubation with rhodamine-conjugated anti-human antibody (Invitrogen). Cell surface vs. internalized antibodies were imaged by confocal microscope (Zeiss LSM 710).

4.3.10 RT-PCR

Total RNA was isolated from cultured cells with RNAeasy kit (Qiagen, Valencia, CA) according to the manufacturer's protocol. 1 µg of total RNA was used for reverse transcription. The expression of GAPDH and ephrin-B2 was analyzed with the following primers: GAPDH: 5'-TTGAGGTCAATGAAGGGGTC/5'-GAAGGTGAAGGTCGGAGTCA; Ephrin-B2: 5'-GTGTGGAAGTACTGCTGGGGTGT/5'-GGCACAGTTGAGGAGAGGGGTATT.

4.3.11 Immunohistology of tumor xenograft

10⁶ human colon cancer cells (COLO205 and HCT116; a kind gift from Dr. Michael King, Cornell University) were mixed in 0.1 ml 50% Matrigel (BD) and xenografted into nude mice (Jackson Laboratory). 14 days after injection when xenograft tumor size reached ~80 mm³, mice were euthanized and tumors were harvested. All animal experiments were conducted in compliance with the regulations defined by the Institutional Laboratory Animal Use and Care Committee of Cornell University (Protocol number 2009-0071). Harvested tumors were fixed in 4% paraformaldehyde overnight at RT, rinsed 3 times for 10 min at RT each in 30%

ethanol and then 50% ethanol, and then kept in 70% ethanol for several hours before embedding into a paraffin block for sectioning. In order to detect ephrin-B2 in the xenograft sections, tissues sections were deparaffinized in xylene 3 times for 4 min each at RT, rehydrated with graded ethanol, and then boiled in 10 mM citrate buffer (pH 6.0) for 10 min for antigen retrieval. The tissue sections were blocked with blocking solution (25 mM Tris-HCl, pH 7.4, 150 mM NaCl, 2 mM KCl, 0.3% Triton X-100, 1% goat serum) for 1 h at RT. Sections were incubated with the primary antibodies at 1 µg/ml overnight at 4 °C, followed by incubation with secondary biotin-conjugated goat anti-human antibody (Invitrogen). Endogenous peroxidase activity was quenched with 0.3% hydrogen peroxide in methanol for 10 minutes at RT. Peroxidase-conjugated streptavidin (Vectastain Elite ABC stain, Vector Laboratories) was added to the sections. After each incubation, sections were washed 3 times with TBS buffer (25 mM Tris, pH 7.4, 150 mM NaCl, 2 mM KCl). Sections were then exposed to chromogen diaminobenzidine peroxidase substrate (Invitrogen) for 5 min, rinsed with water, and counterstained with Mayer's hematoxylin, dehydrated in graded ethanol, and cleared in xylene. Slides were sealed in mounting medium and a coverslip. Negative control slides were treated same way except for the use of primary antibody.

4.3.12 Immunohistology of human tissue array

Human tumor tissue array (TP484, US Biomax) was deparaffinized and subjected to the same procedures as used for the immunostaining of tumor xenograft with EC8. Selected tumor tissue array slides were also used for immunofluorescence. After antigen retrieval and blocking, sections were incubated with primary antibodies

(EC8, mouse anti-human CD31 antibody (Invitrogen)) at 1 μ g/ml overnight at 4 °C. After washing, tissue sections were incubated with AF488-conjugated goat anti-mouse secondary antibody, biotin-conjugated goat anti-human antibody, and were subsequently labeled with rhodamine-conjugated streptavidin. After each incubation, sections were washed 3 times with TBS buffer (25 mM Tris, pH 7.4, 150 mM NaCl, 2 mM KCl). Immunofluorescent images were acquired with a fluorescent microscope (MetaMorph, Molecular Devices).

4.3.13 Statistical analysis

Data were expressed as mean \pm standard deviation of no smaller than triplicates, and analyzed for statistical significance using GraphPad Prism 5 (Graphpad Software). Student's t-test was used to compare the binding levels and to determine statistical significance (Figure 4.7a).

4.4 Results

4.4.1 Novel strategy of selecting antibodies against ephrin-B2

We have previously shown that phage library of human antibody can be directly panned against antigens expressed in yeast (Figure 4.1a) with great efficiency in selection of high affinity monoclonal antibodies [21]. Surface expression of ectodomain of ephrin-B2 on yeast cell surface was first validated by antibody binding to Myc tag, which was placed at the C-terminal of ephrin-B2, as well as the binding of EphB4, a physiological receptor of ephrin-B2 (Figure 4.1). Subtractive panning of a phage library of human single chain fragment variable fragment (scFv), consisting of depletion against yeast expressing irrelevant antigens followed by positive selection

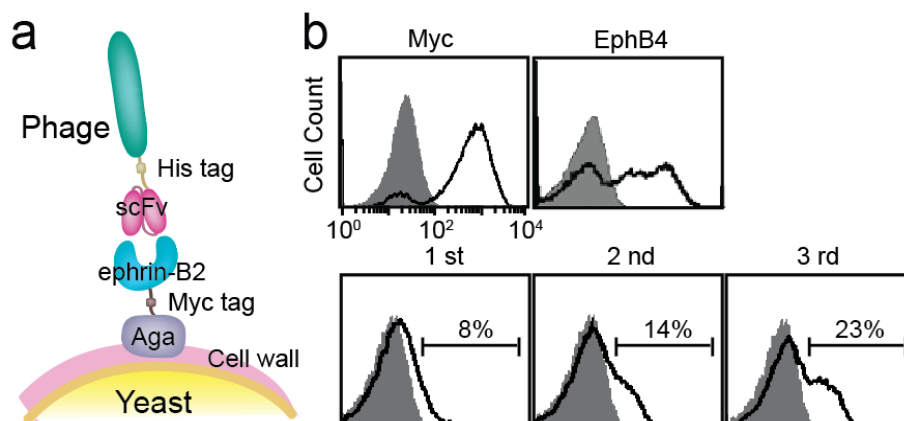


Figure 4.1: (a) A schematic diagram of phage panning against antigens expressed in yeast display system [34]. (b) Immunofluorescence flow cytometry measurements of protein and phage binding to yeast cells. Surface-displayed ephrin-B2 was detected by the binding of anti-Myc antibody ('Myc') as well as recombinant human EphB4-Fc ('EphB4') to yeast cells (top panel). Progressive enrichment of phage clones from first three rounds of panning (denoted as '1 st', '2 nd' and '3 rd') was detected by antibody against His tag (bottom panel). Histograms drawn in shaded area and solid lines indicate antibody binding to uninduced and induced yeast cells, respectively. The percentage of phage clones with positive binding is indicated.

against ephrin-B2, resulted in a progressive increase in the percentage of phage clones bound to ephrin-B2 (Figure 4.1b). A total of 96 phage clones were selected from the third round pool and tested individually for binding to ephrin-B2 using flow cytometry. This resulted in 85 clones with positive binding (data not shown). Out of these 85 clones, 10 high-affinity phage clones were then sequenced, which identified three unique clones (designated as scFv-EA6, scFv-EB1 and scFv-EC8). Two best binders, scFv-EB1 and scFv-EC8 were chosen for production in bacteria and purified by nickel-nitrilotriacetic acid (Ni-NTA) column, followed by gel filtration

chromatography, which resulted in one distinct band around 35 kDa in SDS-PAGE (Figure 4.2a). Soluble scFv-EB1 and scFv-EC8 not only retained binding to yeast but also showed specific binding to ephrin-B2 expressed in mammalian cells, judging from the detection of basal expression in 293T and enhanced binding after transient expression of full-length ephrin-B2 in 293T (Figure 4.2b). scFv-EA6, scFv-EB1 and scFv-EC8 differed mainly within the complementarity determining regions (Figure 4.3). Overall, scFv-EC8 showed highest binding affinity to ephrin-B2, and was chosen for further studies.

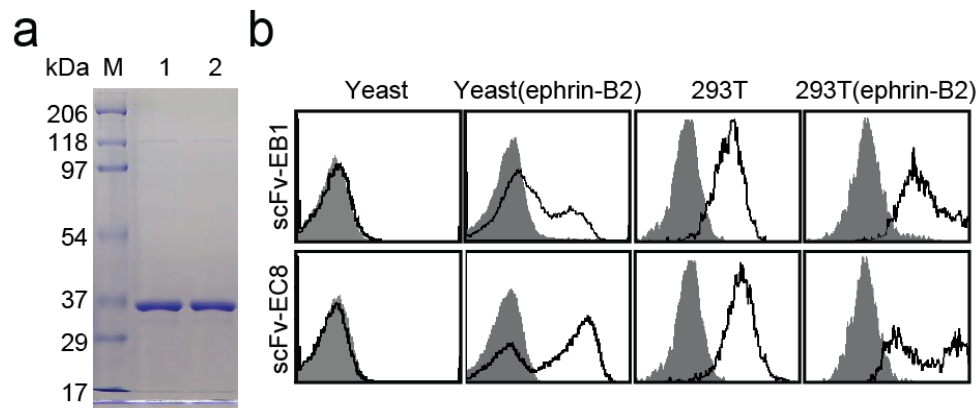


Figure 4.2: (a) SDS-PAGE of scFv-EB1 (lane '1') and scFv-EC8 (lane '2'). (b) Ephrin-B2 specific scFv binding to irrelevant yeast cells, yeast cells with expression of ephrin-B2 ectodomain, 293T cells, and 293T cells with transient expression of full-length ephrin-B2. Shown are the histograms of cells labeled with secondary antibody with (solid line) and without (shaded area) ephrin-B2 specific scFv as primary antibody.

4.4.2 Characterization of single-chain antibody fused to Fc domain

Although scFv-EC8 was fully functional in binding to ephrin-B2, for future *in vivo* applications and many standard assays relying on the presence of immunoglobulin Fc region, scFv fusion to Fc was constructed in pcDNA3.1 and produced in mammalian cells (Figure 4.4). Under the reducing condition, the Fc fusion of scFV-EC8 migrated around 64 kDa, consistent with its nominal molecular weight. scFv-EC8 fusion to Fc (designated as EC8) was fully functional, retaining specific binding to ephrin-B2 expressed in yeast and in 293T (Figure 4.5) with higher level of binding compared with the levels seen with scFv-EC8 (Figure 4.2b). EC8 also exhibited comparable binding to murine ephrin-B2 expressed in transformed murine ovarian cells [22] (Figure 4.5), an anticipated result due to the fact that murine ephrin-B2 differed by only three residues from human ephrin-B2 expressed in yeast (Thr-22 to Gly-165) for phage screening. The binding affinity (equilibrium dissociation constant, K_D) of EC8 to ephrin-B2 was around 3.2 nM, based on the fluorescence measurement using ephrin-B2-expressing 293T cells labeled in serial dilutions of EC8 (Figure 4.6). The increase in affinity of EC8 to ephrin-B2 was due to the dimerization

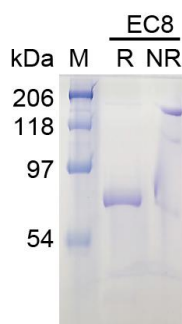


Figure 4.4: SDS-PAGE images of EC8 resolved under reducing (R) and non-reducing (NR) conditions.

effect of scFv, commonly noted as bivalency or avidity effect.

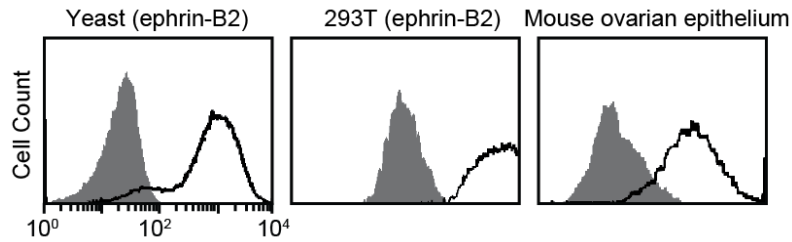


Figure 4.5: EC8 (solid line) binding to yeast cells, 293T with stable expression of ephrin-B2, and murine ovarian epithelium. The binding of isotype control is shown in shaded area.

EC8 was conformation-specific against ephrin-B2, indicated from significant loss of binding to ephrin-B2 expressing yeast cells when ephrin-B2 was partially denatured by incubating cells either in guanidine hydrochloride at 6 M or in elevated temperature (Figure 4.7a). The reduction in the level of EC8 binding to ephrin-B2 was not due to a change in surface expression as antibody binding to Myc tag was invariant. The property of EC8 to recognize conformation-specific epitope was also corroborated by its inability to stain ephrin-B2 in western blot (data not shown). We then tested if EC8 would specifically pull down ephrin-B2 from detergent-solubilized 293T cell lysates. Conformation-specificity of monoclonal antibody (mAb) EC8 was also confirmed with the detection of one distinct band of ~45 kDa in size from the lysates only after precipitation with EC8, stained by polyclonal antibody against ephrin-B2 (Figure 4.7b). Due to high sequence homology among some members of ephrin family, polyclonal antibodies against ephrin-B2 often crossreact with other ephrins like ephrin-B1 and ephrin-A5, which share sequence identity at 43% and 41%

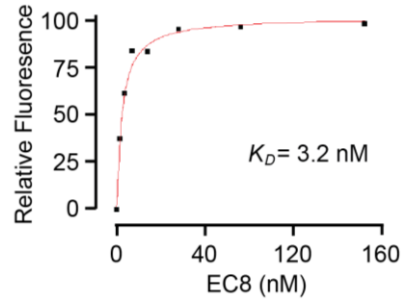


Figure 4.6: Flow cytometry measurements of EC8 binding to 293T cells are shown in filled squares. First order Langmuir adsorption model was used to fit the data to estimate equilibrium dissociation constant (K_D).

with ephrin-B2, respectively. While EphB2 showed comparable binding to all three ephrins tested, EC8 was found specific to ephrin-B2 with little binding to ephrin-B1 and ephrin-A5 (Figure 4.8).

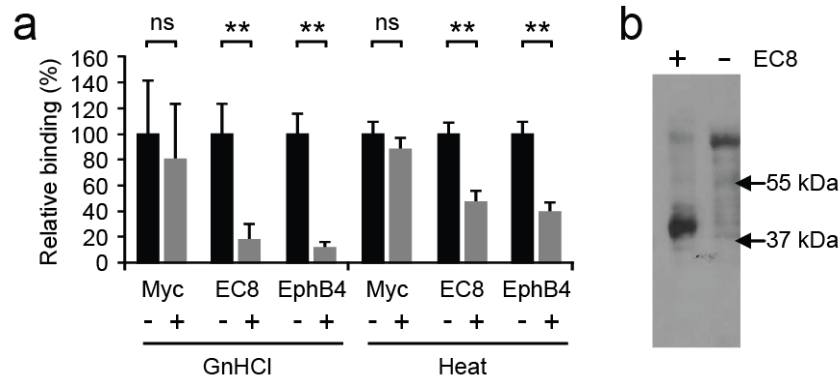


Figure 4.7: (a) Conformation specificity of EC8 against ephrin-B2 was examined by flow cytometry with (+) or without (-) incubating cells either in 6 M guanidine hydrochloride ('GnHCl') for 20 min or in elevated temperature at 80°C ('Heat') for 10 min. (b) Western blot image of immunoprecipitated ephrin-B2 from 293T cells with (+) or without (-) EC8 antibody, detected by rabbit ephrin-B2 polyclonal antibody.

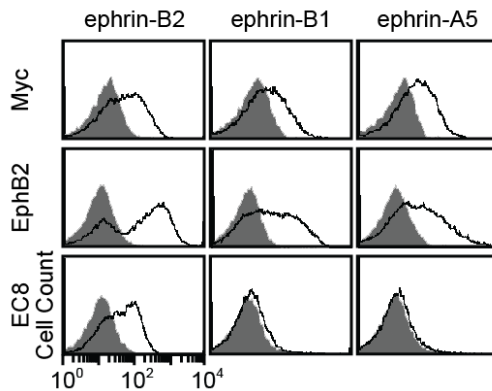


Figure 4.8: Flow cytometry measurements of EC8 binding to ephrin-B1 and ephrin-A5 displayed on yeast. Labeling of uninduced yeast cells is shown in shaded histograms.

4.4.3 mAb EC8 blocked ephrin-B2 interaction with EphB4 and was internalized by ephrin-B2 ligation

After confirming specific binding of EC8 to ephrin-B2, we examined if EC8 was able to block ephrin-B2 interaction with its cognate receptor, EphB4. This would potentially be useful in blocking bidirectional signals triggered by ephrin-B2 and EphB4 interaction, which is important for normal physiology as well as in disease progression. In comparison to human immunoglobulin G (IgG) as isotype control, increasing concentration of EC8 added to yeast cells expressing ephrin-B2 led to a gradual decrease in the binding of EphB4 (used at 100 nM) to ephrin-B2, close to complete inhibition seen at 250 nM of EC8 (Figure 4.9). We detected the distribution of EC8 in 293T after labeling under fluorescence microscope, and observed that ephrin-B2 ligation by EC8 triggered cells to internalize the antibody. In order to differentiate surface-bound vs. intracellular pool of EC8, confocal microscopy was

used to image cells prior to and after membrane permeabilization, which visualized distinct intracellular staining of EC8 (Figure 4.10).

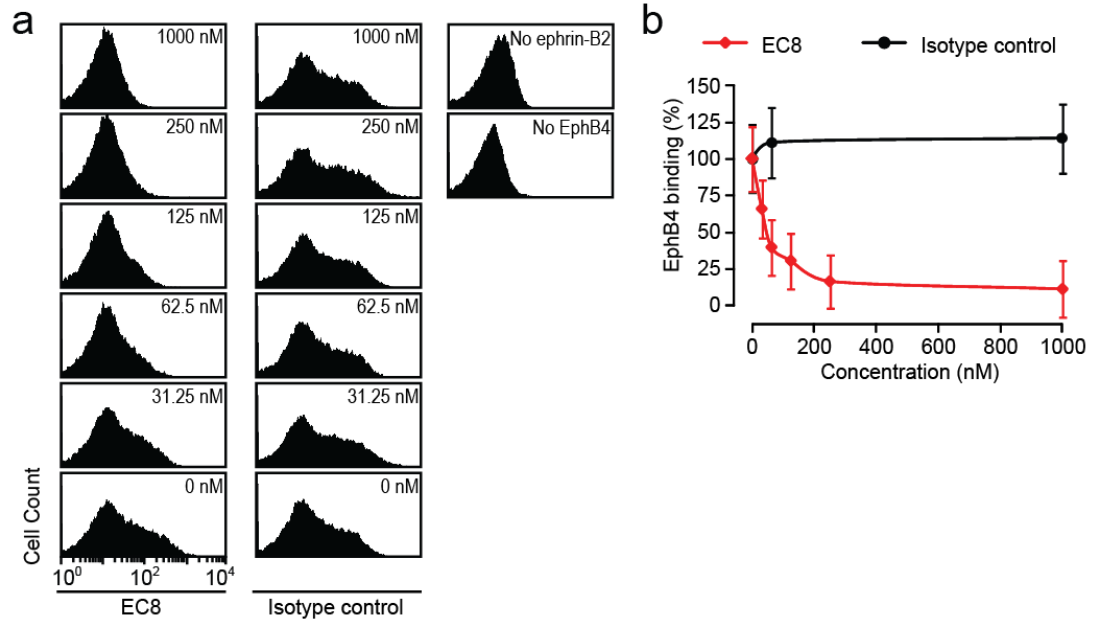


Figure 4.9: Competition assay. Relative binding of EphB4 (100 nM) to yeast cells expressing ephrin-B2, preincubated with varying concentrations of EC8, was measured by flow cytometry. Affinity purified human IgG was included as isotype control. $n = 3$ independent measurements.

4.4.4 EC8 detection of ephrin-B2 expression in tumor tissues and tumor-associated vasculature

Upregulation of ephrin-B2/EphB4 has been observed in many tumors, including ovary, colon, breast, and glioma, with a strong correlation with poor prognosis [14-18, 23-24]. With two widely used colon cancer cell lines, COLO205 and HCT116, we found upregulation of ephrin-B2 by flow cytometry using EC8 (Figure 4.11a). Chinese hamster ovarian (CHO) cells with no ephrin-B2 expression

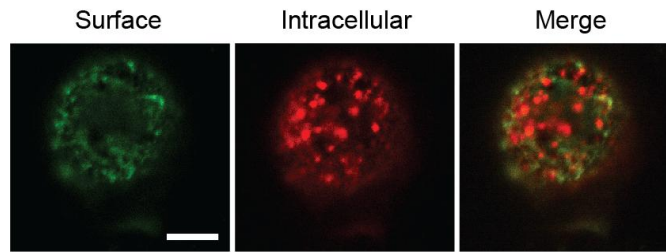


Figure 4.10: Confocal microscopic images of surface-bound EC8 and internalized ones before and after membrane permeabilization of 293T cells. Scale bar = 10 μ m.

were included as a negative control. The relative levels of ephrin-B2 between different cell lines were further confirmed by RT-PCR, with 293T cells stably expressing ephrin-B2 as a positive control (Figure 4.11b). Since not all conformation-

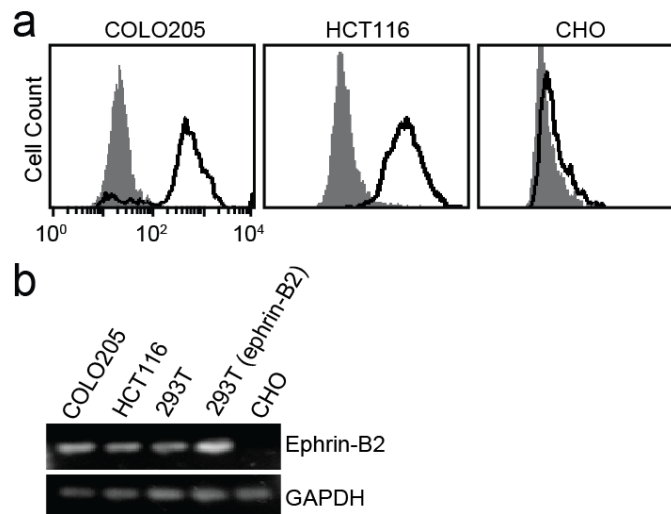


Figure 4.11: (a) Flow cytometry measurements of EC8 binding to COLO205 and HCT116 cells (solid line) in comparison to the isotype control (shaded area). CHO cells with no ephrin-B2 expression were also included for comparison. (b) RT-PCR detection of ephrin-B2 expression in different cell lines.

specific antibodies are compatible with immunohistology after a standard procedure for tissue fixation, we examined if EC8 can be used to probe ephrin-B2 expression in the tissue. When colon tumor tissues were immunostained after tumor growth in mice and harvest, EC8 not only delineated human tumor xenograft with high ephrin-B2 expression, but also identified the vasculature within the tumor due to the cross-reactivity of EC8 with both human and murine ephrin-B2 (Figure 4.12). EC8 staining of ephrin-B2 clearly differentiated tumor cells (marked with arrowhead) from the murine stroma (marked with arrow) (Figure 4.12).

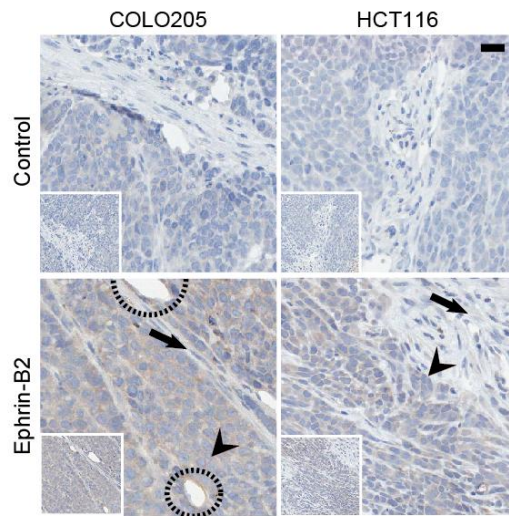


Figure 4.12: Immunostaining of ephrin-B2 on human colon cancer xenografted in mice. Control denotes immunostaining without EC8 as a primary antibody. Tumor and stromal cells were indicated with arrowhead and arrow, respectively. Circle indicates murine endothelium stained with EC8. Scale bar = 20 μ m.

4.4.5 EC8 detection of the upregulation of ephrin-B2 in diverse human tumors of epithelial origin

We further examined if EC8 could be applied to detect ephrin-B2 expression

in other types of tumor directly collected from human patients. Among several epithelium-originated cancers, ranging from ovarian, lung, prostate, breast to colon, high level expression of ephrin-B2 was all found by immunostaining (Figure 4.13a & 4.13b). In comparison to normal tissues or tumor stroma showing no or only baseline ephrin-B2 staining, malignant tumor cells characterized by their irregular cell shape (*e.g.* colon and lung) and aberrantly enlarged (*e.g.* colon, lung and prostate) or dense (*e.g.* breast) nucleoli had distinctively higher ephrin-B2 staining. Dual staining on human colon cancer sample with both anti-CD31 antibody and EC8 revealed some of the vasculatures that were co-stained, indicative of EC8 detecting tumor-associated vasculature (Figure 4.13c).

4.5 Discussion

Ephrin-B2 is preferentially expressed in arterial endothelium and smooth muscle cells, as well as neovasculature within the tumor. Expression of ephrin-B2 is modulated by VEGF, smooth muscle cell contact, and stress [25-27]. Ephrin-B2 has also shown to be upregulated in many cancers, including colon [15], uterine [16], ovarian [17] and esophageal cancers [18]. Despite the importance of the role of ephrin-B2 in physiology and disease, up until now monoclonal antibody specific to ephrin-B2 has not been widely available. This may be attributed to the fact that human ephrin-B2 is highly homologous to those of other mammals including rodents, presenting a challenge to isolating high affinity antibody from immunization and hybridoma technique. Limited *in vivo* alternatives for making antibodies against highly conserved antigens, including using mice with impaired immune response [19-

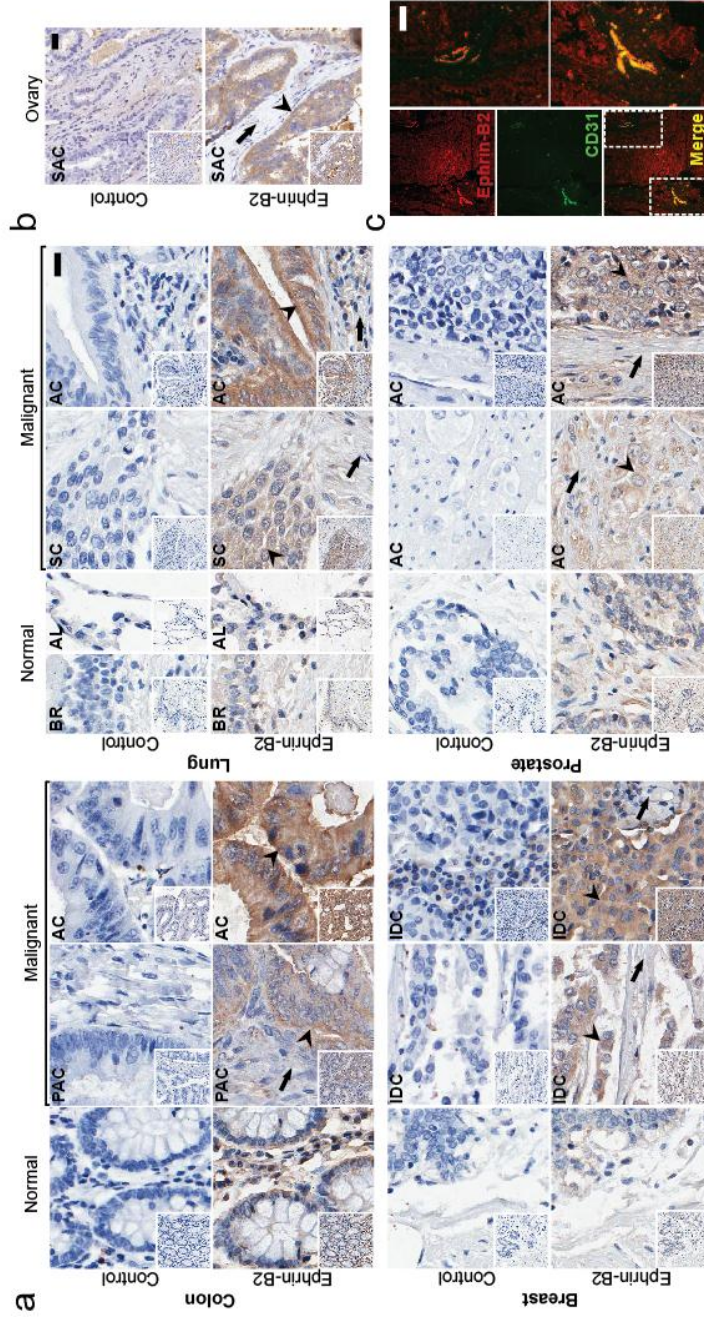


Figure 4.13: (a&b) Immunostaining of ephrin-B2 expression in human tumor tissue arrays using EC8. Control denotes immunostaining without EC8 as a primary antibody. Tumor and stromal cells were indicated with arrowhead and arrow, respectively. Scale bar = 20 μm. PAC = Papillary Adenocarcinoma; AC = Adenocarcinoma; BR = Bronchus; AL = Alveoli; SC = Squamous Cell Carcinoma; SAC = Serous Adenocarcinoma. IDC = Nonspecific Infiltrating Duct Carcinoma. (c) Immunofluorescence staining on human colon tumor tissue demonstrating that EC8 (red) detects ephrin-B2 expressions in both cancer cells and tumor-associated vasculature (green). Blow up views of the two areas indicated with dashed box are shown in the right panel. Scale bar = 100 μm.

20], have been reported, yet the concerns remain on the multi-specificity and low-affinity of auto-antibodies [20].

Here we report the isolation of monoclonal antibody against ephrin-B2, which was selected from a phage library of human single chain antibody. Rather than panning phage clones against soluble antigens, we used yeast cells expressing antigens to pull down reactive phage clones, which was found to be highly efficient in rapidly enriching specific phage library. Given the library diversity (10^8) and an enrichment factor of 10^2 - 10^3 per each round of our screening strategy [21], we were able to observe specific phage clones reactive to ephrin-B2 as early as after two rounds of sorting. As antibody selection is based on monomeric interaction between antigen-antibody, after conversion into a dimer by fusion to IgG Fc, the affinity ($K_D = 3.2$ nM) of ephrin-B2 antibody (EC8) was comparable to those of high affinity monoclonal antibodies produced from hybridoma. Compared to many polyclonal antibodies generated from peptide fragments by immunization, EC8 selected against ephrin-B2 displayed in native conformation on yeast surface was found to be conformation-specific and discriminate ephrin-B2 from other ephrins with high homology.

Antibodies against EphB4 were found to inhibit tumor growth and angiogenesis, some of which are being investigated for anti-cancer therapy in preclinical studies [9-10]. Eph receptor antibodies that were conjugated to small molecule drugs caused internalization of drugs and inhibition of tumor growth *in vivo* [28-19]. Soluble extracellular domain of EphB4 targeting ephrin-B2 has been used in inhibiting angiogenesis and tumor growth *in vivo* [8]. We have found that mAb EC8 potently antagonized ephrin-B2 binding to EphB4, which would block forward and

reverse signaling by EphB4 and ephrin-B2 interaction. Similar to the observation of EphB4 upregulation in some tumors, when human tissue array was probed with mAb EC8, ephrin-B2 was found to be also overexpressed in tumors in lung, breast, ovary, colon, and prostate over respective normal tissue. Consistent with the previous observation of ephrin-B2 expression in tumor-associated vasculature, EC8 delineated ephrin-B2 expression in newly formed vessels within the tumor. Upregulation of ephrin-B2 was also found in colorectal cancer cell lines, COLO205 and HT108 both in cell culture and as a tumor xenograft in mice. Notably, due to the cross-reactive nature of antibody with murine ephrin-B2, mAb EC8 also identified tumor-associated vasculature, simultaneously detecting ephrin-B2 in human tumor as well as ephrin-B2 in murine host.

Neovasculatures in adults sprouting from arterial vessels and capillaries, whether caused by VEGF-signaling, tissue injury, or tumor growth, were found to express ephrin-B2. It is unknown how ephrin-B2 upregulation in some of the tumors of epithelium origin would perturb the balance between ephrin-B2 and Eph4 expressed in arterial and venous vessels, respectively, and contribute to the tumor growth and metastasis. Given the observation that overexpression of ephrin-B2 in some tumors is correlated with poor prognosis [1, 16], it will be an interesting question if the role of ephrin-B2 together with EphB receptors in some tumor is associated with the promotion of the vasculature growth and the adenoma-carcinoma transition, facilitating tumor metastasis. We propose that high affinity and antagonist antibodies such as EC8 would provide a valuable tool for examining the role of ephrin-B2 expression on tumor angiogenesis and migration.

REFERENCES

- [1] Pasquale EB. Eph receptors and ephrins in cancer: bidirectional signalling and beyond. *Nat Rev Cancer*. 2010;10:165-80.
- [2] Adams RH, Wilkinson GA, Weiss C, Diella F, Gale NW, Deutsch U, et al. Roles of ephrinB ligands and EphB receptors in cardiovascular development: demarcation of arterial/venous domains, vascular morphogenesis, and sprouting angiogenesis. *Genes Dev*. 1999;13:295-306.
- [3] Wang HU, Chen ZF, Anderson DJ. Molecular distinction and angiogenic interaction between embryonic arteries and veins revealed by ephrin-B2 and its receptor Eph-B4. *Cell*. 1998;93:741-53.
- [4] Adams RH, Diella F, Hennig S, Helmbacher F, Deutsch U, Klein R. The cytoplasmic domain of the ligand ephrinB2 is required for vascular morphogenesis but not cranial neural crest migration. *Cell*. 2001;104:57-69.
- [5] Yamada S, Ebihara S, Asada M, Okazaki T, Niu K, Ebihara T, et al. Role of ephrinB2 in nonproductive angiogenesis induced by Delta-like 4 blockade. *Blood*. 2009;113:3631-9.
- [6] Gerety SS, Wang HU, Chen ZF, Anderson DJ. Symmetrical mutant phenotypes of the receptor EphB4 and its specific transmembrane ligand ephrin-B2 in cardiovascular development. *Mol Cell*. 1999;4:403-14.
- [7] Pasquale EB. Eph-ephrin bidirectional signaling in physiology and disease. *Cell*. 2008;133:38-52.
- [8] Kertesz N, Krasnoperov V, Reddy R, Leshanski L, Kumar SR, Zozulya S, et al. The soluble extracellular domain of EphB4 (sEphB4) antagonizes EphB4-EphrinB2 interaction, modulates angiogenesis, and inhibits tumor growth. *Blood*. 2006;107:2330-8.

- [9] Krasnoperov V, Kumar SR, Ley E, Li X, Scehnet J, Liu R, et al. Novel EphB4 monoclonal antibodies modulate angiogenesis and inhibit tumor growth. *Am J Pathol.* 2010;176:2029-38.
- [10] Xu Z, Jin H, Qian Q. Humanized anti-EphB4 antibodies for the treatment of carcinomas and vasculogenesis-related diseases. *Expert Opin Ther Pat.* 2009;19:1035-7.
- [11] Sawamiphak S, Seidel S, Essmann CL, Wilkinson GA, Pitulescu ME, Acker T, et al. Ephrin-B2 regulates VEGFR2 function in developmental and tumour angiogenesis. *Nature.* 2010;465:487-91.
- [12] Wang Y, Nakayama M, Pitulescu ME, Schmidt TS, Bochenek ML, Sakakibara A, et al. Ephrin-B2 controls VEGF-induced angiogenesis and lymphangiogenesis. *Nature.* 2010;465:483-6.
- [13] Germain S, Eichmann A. VEGF and ephrin-B2: a bloody duo. *Nat Med.* 2010;16:752-4.
- [14] Liu W, Ahmad SA, Jung YD, Reinmuth N, Fan F, Bucana CD, et al. Coexpression of ephrin-Bs and their receptors in colon carcinoma. *Cancer.* 2002;94:934-9.
- [15] Liu W, Jung YD, Ahmad SA, McCarty MF, Stoeltzing O, Reinmuth N, et al. Effects of overexpression of ephrin-B2 on tumour growth in human colorectal cancer. *Br J Cancer.* 2004;90:1620-6.
- [16] Alam SM, Fujimoto J, Jahan I, Sato E, Tamaya T. Overexpression of ephrinB2 and EphB4 in tumor advancement of uterine endometrial cancers. *Ann Oncol.* 2007;18:485-90.
- [17] Alam SM, Fujimoto J, Jahan I, Sato E, Tamaya T. Coexpression of EphB4 and ephrinB2 in tumour advancement of ovarian cancers. *Br J Cancer.* 2008;98:845-51.

- [18] Tachibana M, Tonomoto Y, Hyakudomi R, Hyakudomi M, Hattori S, Ueda S, et al. Expression and prognostic significance of EFNB2 and EphB4 genes in patients with oesophageal squamous cell carcinoma. *Dig Liver Dis.* 2007;39:725-32.
- [19] Andrievskaia O, McRae H, Elmgren C, Huang H, Balachandran A, Nielsen K. Generation of antibodies against bovine recombinant prion protein in various strains of mice. *Clin Vaccine Immunol.* 2006;13:98-105.
- [20] Zhou H, Wang Y, Wang W, Jia J, Li Y, Wang Q, et al. Generation of monoclonal antibodies against highly conserved antigens. *PLoS One.* 2009;4:e6087.
- [21] Hu X, Kang S, Lefort C, Kim M, Jin MM. Combinatorial libraries against libraries for selecting neoepitope activation-specific antibodies. *Proc Natl Acad Sci U S A.* 2010;107:6252-7.
- [22] Flesken-Nikitin A, Choi KC, Eng JP, Shmidt EN, Nikitin AY. Induction of carcinogenesis by concurrent inactivation of p53 and Rb1 in the mouse ovarian surface epithelium. *Cancer Res.* 2003;63:3459-63.
- [23] Nakada M, Anderson EM, Demuth T, Nakada S, Reavie LB, Drake KL, et al. The phosphorylation of ephrin-B2 ligand promotes glioma cell migration and invasion. *Int J Cancer.* 2010;126:1155-65.
- [24] Varelias A, Koblar SA, Cowled PA, Carter CD, Clayer M. Human osteosarcoma expresses specific ephrin profiles: implications for tumorigenicity and prognosis. *Cancer.* 2002;95:862-9.
- [25] Hainaud P, Contreres JO, Villemain A, Liu LX, Plouet J, Tobelem G, et al. The role of the vascular endothelial growth factor-Delta-like 4 ligand/Notch4-ephrin B2 cascade in tumor vessel remodeling and endothelial cell functions. *Cancer Res.* 2006;66:8501-10.

- [26] Korff T, Dandekar G, Pfaff D, Fuller T, Goettsch W, Morawietz H, et al. Endothelial ephrinB2 is controlled by microenvironmental determinants and associates context-dependently with CD31. *Arterioscler Thromb Vasc Biol.* 2006;26:468-74.
- [27] Goettsch W, Augustin HG, Morawietz H. Down-regulation of endothelial ephrinB2 expression by laminar shear stress. *Endothelium.* 2004;11:259-65.
- [28] Mao W, Luis E, Ross S, Silva J, Tan C, Crowley C, et al. EphB2 as a therapeutic antibody drug target for the treatment of colorectal cancer. *Cancer Res.* 2004;64:781-8.
- [29] Jackson D, Gooya J, Mao S, Kinneer K, Xu L, Camara M, et al. A human antibody-drug conjugate targeting EphA2 inhibits tumor growth in vivo. *Cancer Res.* 2008;68:9367-74.
- [30] Owens RM, Gu X, Shin M, Springer TA, Jin MM. Engineering of single Ig superfamily domain of intercellular adhesion molecule 1 (ICAM-1) for native fold and function. *J Biol Chem.* 2010;285:15906-15.
- [31] Semple TU, Quinn LA, Woods LK, Moore GE. Tumor and lymphoid cell lines from a patient with carcinoma of the colon for a cytotoxicity model. *Cancer Res.* 1978;38:1345-55.
- [32] Brattain MG, Fine WD, Khaled FM, Thompson J, Brattain DE. Heterogeneity of malignant cells from a human colonic carcinoma. *Cancer Res.* 1981;41:1751-6.
- [33] Jin M, Song G, Carman CV, Kim YS, Astrof NS, Shimaoka M, et al. Directed evolution to probe protein allostery and integrin I domains of 200,000-fold higher affinity. *Proc Natl Acad Sci U S A.* 2006;103:5758-63.
- [34] Boder ET, Wittrup KD. Yeast surface display for screening combinatorial polypeptide libraries. *Nat Biotechnol.* 1997;15:553-7.

CHAPTER 5

CONCLUSIONS AND FUTURE DIRECTIONS

5.1 Summary

In this study, we first present a physiology-inspired design of magnetite nanoparticles compatible with molecular detection by both optical imaging and MRI. Generally, nanoparticles will experience a hydrodynamic force induced by the blood flow *in vivo*, requiring simultaneous molecular interactions with sufficient adhesion strength with the cells for nanoparticles to remain on the cell surface. Therein the design of nanoparticles with tunable affinity and avidity of physiological interactions would be critical to their selectivity and efficiency of targeting. Through a surface coating of activating mutant of LFA-1 integrin, our SPIO nanomicelle mimics an inflamed leukocyte in its ability to recognize inflamed endothelium expressing a high level of ICAM-1. Despite the fact that ICAM-1 is basally expressed in many different types of cells including endothelium and immune cells, we observed specific accumulation of systemically-delivered nanoparticles into several inflammatory microenvironments, such as vasculature within the tumor and the invasive tumor front where tumor growth and angiogenesis were active, as well as the subcutaneous space where acute inflammation was induced by LPS, while their localization elsewhere was much lower as indicated by optical imaging.

With developments in quantitative MRI techniques, this study also explores a clinically adaptable method for organ-level mapping of inflammation by quantifying

the susceptibility of leukocyte-mimetic nanoparticles (LMN). We examined quantitative susceptibility mapping (QSM) in the context of sepsis diagnosis and demonstrated the potential use of LMN as a bimodal diagnostic agent for the early detection of sepsis or systemic inflammatory response. In treating mice with LMN, we were able to readily differentiate between mice, either pre-treated with systemic LPS or left untreated, by quantitatively measuring nanoparticle localization in various abdominal organs in each of the subjects. This differential effect is most apparent when measuring nanoparticle localization in the liver; a temporal mapping of nanoparticle distribution through MRI QSM demonstrated twice the amount of LMN localized into the livers of sepsis-induced mice compared to that of non-septic subjects, or of those treated with ICAM-1 independent nanoparticles. The observed differences by QSM were corroborated qualitatively by near-IR optometry and quantitatively by radioactivity measurement. Histological staining of the tissue sections of liver also revealed a larger degree of nanoparticle accumulation in LPS-treated LMN cases, with specific iron staining observed in both endothelial cells and Kupffer cells, while greater amount of LMN localized into Kupffer cells.

5.2 LMN as a biomimetic: potential caveats and improvements

Biocompatibility is the priority concern of engineering nanoparticles, which determines the risk of exposure during animal studies and clinical trials. In the case of LMN, we chose magnetite, phospholipid/fatty acid, and engineered human protein as the main building blocks. Magnetite is the major component of Feridex, an intravenously injectable colloidal superparamagnetic iron oxide (SPIO) associated

with dextran and FDA approved contrast agent for MRI [1]. Known to be taken up by the reticuloendothelial system (RES), iron oxide enters the usual iron metabolism cycle after administration. Lipid complexes composed of phospholipids and fatty acids have also been widely applied in drug delivery. For example, Doxil is the chemotherapy drug doxorubicin (DOX) encapsulated in a closed lipid sphere, and is used primarily for the treatment of ovarian cancer or AIDS-related Kaposi's sarcoma [2]. Even though no obvious cytotoxicity is currently associated with the materials of LMN, including iron oxide, lipid and protein; potential immunogenicity of nanoparticles could exist when a large density of proteins are laid out in a regular manner on the particle surface, which are highly similar to other naturally occurring immunogens such as viruses. Consistent with present documentation on the RES uptake of iron oxide nanoparticles, we have observed distinguishable retention of SPIO in normal mouse liver, probably due to the phagocytic activity of resident immune cells (Figure 3.7 & 3.8). Is this part of the normal excretion pathway of magnetite nanoparticles or a sign of immunogenicity? To scrutinize these possibilities, we examined the mRNA level of two inflammation markers (ICAM-1 and VCAM-1), after exposing HMEC-1 cells (human microvascular endothelial cell) to nanoparticles with or without surface protein coating. As one important sentinel for immune system, if the endothelial cell senses nanoparticles as 'alien' and sets off the alarm of inflammation, subsequent immune response to nanoparticles will subsequently follow. Quantitative PCR showed no noticeable upregulation of ICAM-1 and VCAM-1 in HMEC-1 cells after incubation with nanoparticles, unlike LPS treatments that trigger significant inflammatory signals (Figure 5.1). This observation indicates that

nonspecific interaction between nanoparticles and endothelial cells, or baseline binding of LMN to quiescent endothelium, will not cause the activation of immune system. Therefore the overall design of LMN is largely benign to biological systems based on our current knowledge.

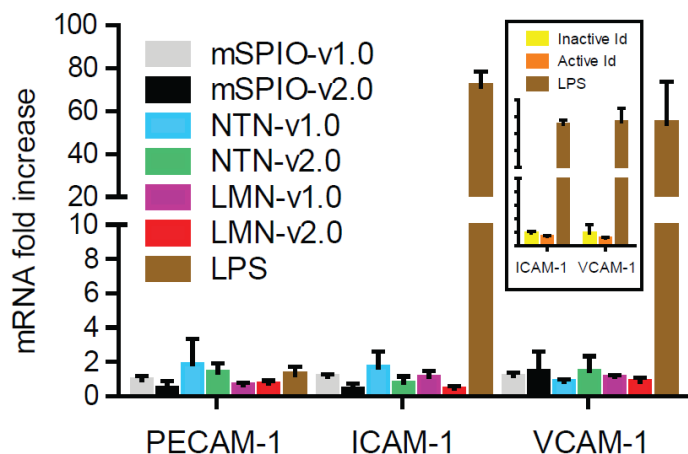
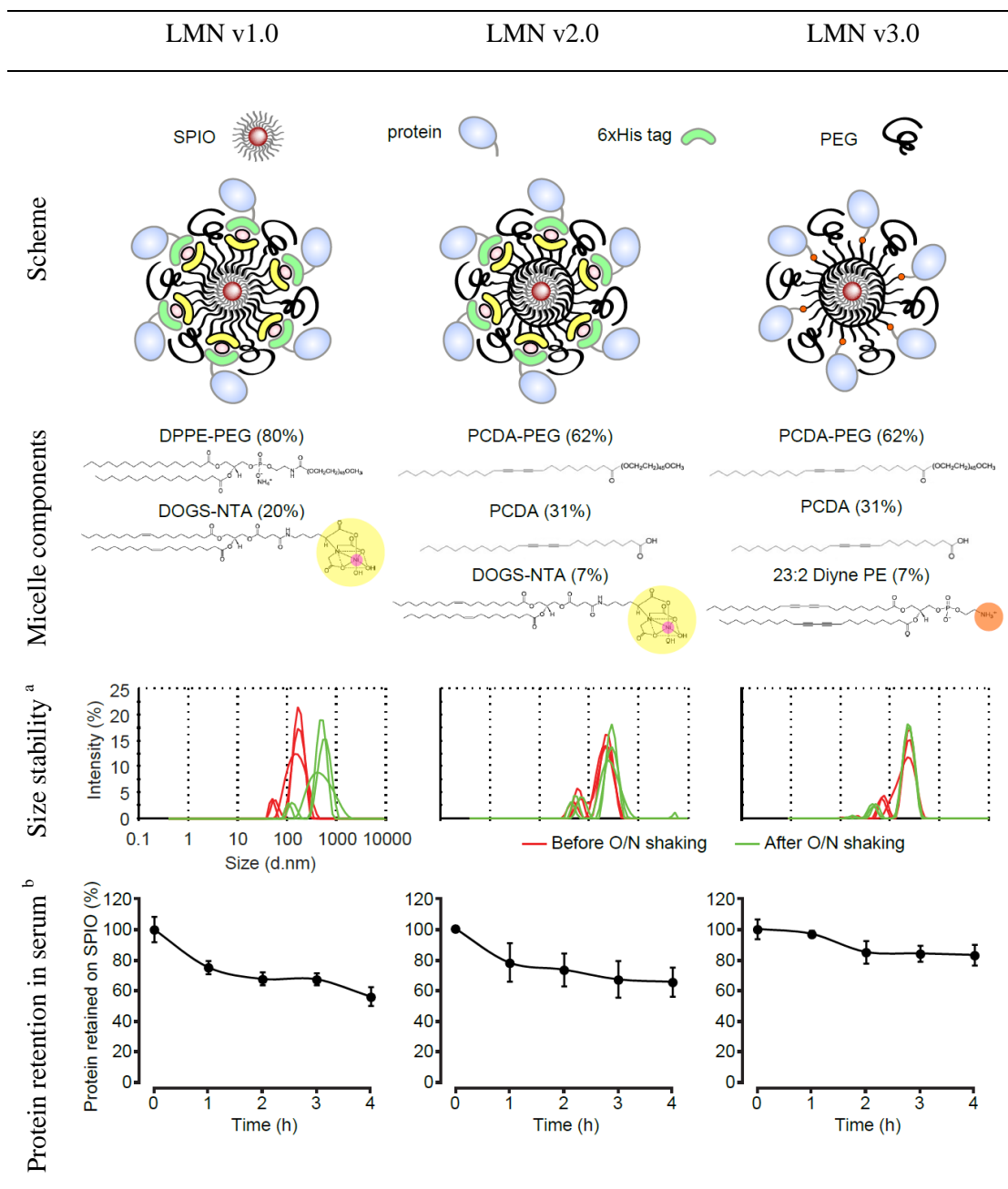


Figure 5.1: Quantitative PCR of HMEC-1 cells on the mRNA level of inflammatory markers (ICAM-1 & VCAM-1), in comparison to housekeeping gene PECAM-1. Cells were treated with 50 µg/mL nanoparticles (coated with no protein: mSPIO; coated with inactive I domain mutant D137A: NTN; coated with active I domain mutant F265S/F292G: LMN.) or 10 µg/mL LPS at 37 °C for 3 h. Inset shows the result when cells were incubated with 20 µg/mL of I domain. Refer to Table 5.1 for specific versions of nanoparticles.

In addition to biocompatibility, *in vivo* stability is also an important factor that should be taken into account for nanomicelle-based biomimetics. Natural biomembranes are primarily composed of lipids, proteins and a relatively small amount (less than 10%) of carbohydrates which are covalently bound to either lipids or proteins [3]. A variety of molecular motions exist within the membrane matrix.

Lipids undergo rotation and segmental motions, kink formation, and traverse from one interface to the other (flip-flop). Because of this, phospholipid membranes are mechanically weak and unstable by nature. In most artificially prepared phospholipid complexes, fewer types of phospholipids and non-covalent interactions are present, making it even more difficult to maintain their stability for practical applications *in vivo* [4]. In one of our studies, subjecting LMN to vigorous shaking at 37 °C overnight resulted in significant increase of its hydrodynamic size, indicating our current design nanomicelle is prone to aggregation under shear force (Table 5.1). It is not a surprising discovery, as great amount of effort has been previously put into obtaining a stable biomembrane model for artificial cells. These attempts include synthesizing phospholipid analogues, particularly polymerizable ones [5]. Among all polymerizable lipids, lipid diacetylene [6] caught our particular attention because it can easily initiate polymerization under the exposure to ultraviolet light (254 nm), and this reaction can be visually monitored by a highly colored product [7] (Figure 5.2a). Replacing DPPE-PEG with an amphiphilic diacetylene 10,12-pentacosadiynoic acid (PCDA) and PCDA-PEG, we obtained a polymerized version of LMN, which we termed as LMN v2.0, in order to differentiate it from the original design, which we termed as LMN v1.0 (Table 5.1). Due to the covalent crosslink between fatty acid molecules, the micelle structure of LMN v2.0 can be well maintained in the presence of chloroform, a strong organic solvent, unlike LMN v1.0, which released its iron content into chloroform soon after incubation, leaving lipids on the interface of water and chloroform (Figure 5.2b). Polymerizing the micelle layer also improved the stability of v2.0 against shear stress as its size did not alter after overnight shaking (Table 5.1).

Table 5.1: Summary of LMN evolution of their property changes



^a Nanoparticle sizes were measured by DLS before and after overnight shaking in PBS at 37 °C.

^b Nanoparticles coating with fluorescent proteins were dialyzed in 50% normal goat serum using 50 kDa MWCO dialysis tubing at RT. Percentage of proteins retained on nanoparticles was quantified by fluorescence. MFI \pm SD was calculated over three independent measurements and displayed here. O/N: overnight.

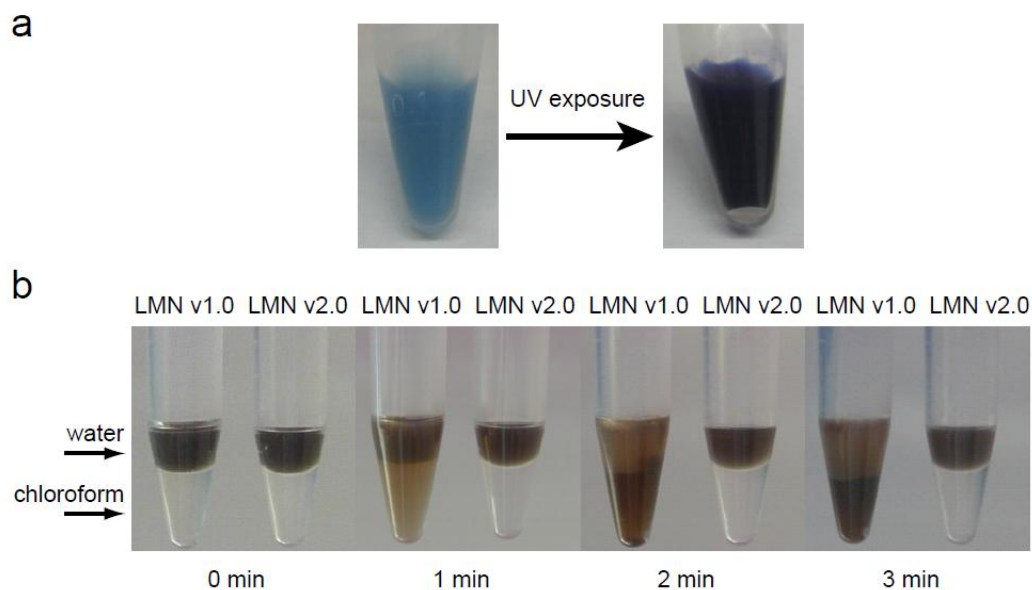


Figure 5.2: (a) Exposure of PCDA vesicle to a UV lamp resulted in the relaxation of photoproduct which was initially blue to a purple polymer. (b) Exposure of LMN v1.0 and v2.0 to chloroform over time resulted in the disruption of v1.0, but not v2.0.

Another caveat of our nanoparticle may be the circulation half-life of His-tagged protein coupled with NTA lipid *in vivo*. Though Ni-NTA-6×His complex offers outstanding convenience in terms of ligand conjugation, Ni-NTA also interacts with some plasma proteins, such as histidine-rich ones [8], resulting in the fast dissociation of ligand proteins off nanoparticles in serum environment (Table 5.1). This is consistent with our previous observation of a high fluorescence signal appearing in the bladder at very early time points (less than 1 h) post nanoparticle injection (Figure 2.16a). Intact LMN has a hydrodynamic diameter of 60 nm, much bigger than the threshold of renal excretion (5.5 nm). However free integrin I domain

is about 5 nm in diameter, and can be rapidly excreted into urine once dissociated. In order to ameliorate this situation, we further replaced DOGS-NTA in LMN v2.0 with 23:2 Diyne-PE, to whose primary amine group I domain can be covalently linked through N terminal cysteine. We termed this new version LMN v3.0, and found it indeed retains more proteins on the surface in the presence of serum (Table 5.1).

5.3 Application of LMN in cancer diagnosis: implications and challenges

It is now well accepted that inflammation actively participates in cancer development [9-11]. As a matter of fact, tumor-promoting inflammation within neoplasia is one critical characteristic enabling the acquisition of canonical cancer hallmarks [12]. There is a plethora of signs showing endothelial cells directly regulate tumor growth through a proinflammatory network consisting of immune cells [11], ‘angiocrine factors’ (FGF2 [13], PDGF β [14], TGF β [15], VEGFA [16], LAMA4 [17], G-CSF [18], NO [19], etc), adhesion molecules (ICAM-1 [20], VCAM-1 [20], E-selectin [20], P-selectin [21], etc), cytokines (TNF [13], IL-1 [14], IL-6 [14], IL-17 [22], etc) and chemokines (IL-8 [14], MCP-1 [23], SDF1 [24], etc). For example, it has been postulated that the binding between ICAM-1 on endothelial cells with apical MUC-1 on circulating tumor cells may represent the first crucial step in metastasis [25]. This binding is known to induce intracellular calcium signaling that instigates two important effects: the release of chemoattractant cytokines for leukocytes, and upregulation of tumor expression of ICAM-1 by the adherent tumor cells [26]. Macrophages then aggregate around the now-adherent tumor cells via formation of tight bonds with the tumor-expressed ICAM-1 and this specific binding elicits the

release of macrophage-derived cytokines and chemokines that attract polymorphonuclear leukocytes (PMNs) [27]. Further, PMN-binding to ICAM-1 on the surface of the tumor cells causes degranulation of the PMNs, [28] releasing proteases that breakdown the endothelial barrier to promote extraluminal migration of tumor cells, subsequent binding of tumor cells to matrix proteins (including ICAM-1), and establishment of metastases [29]. Consistent with such scenarios, several examples of neoplasms expressing high levels of ICAM-1 and their potential for invasion/metastasis have been recognized [20, 30-32]. In this study, we also observed ICAM-1 induction in tumor-associated vasculature, where tumor growth and angiogenesis are active (Figure 2.9). All of this knowledge suggests neoplastic vascular microenvironments undergoing active inflammatory remodeling could be an alternative strategy for tumor targeting [33].

In accordance with current literature on the inflammatory niche of the tumor microenvironment, our preliminary data demonstrated that intravenously injected LMN specifically localized into the vasculature associated with the tumor progression, independent of tumor surface antigen (Figure 2.15). Even though the tumor is known to have the enhanced permeability and retention (EPR) effect [34] in terms of the accumulation of macromolecules, due to a combination of the increased permeability of tumor blood vessels caused by their abnormal structure and the decreased rate of clearance caused by the lack of functional lymphatic vessels in the tumor; a number of implications woven into the architecture of tumor may have perplexed effective penetration of LMN as well as its similars throughout the overall mass of the tumor, as the majority of LMN is distributed at the peripheral region of the tumor xenografts

(Figure 2.15). Three-dimensional penetration studies in solid tumor have shown that increasing the molecular weight of the macromolecule significantly reduces its tumor vascular permeability [35]. With passive distribution, 2-MDa dextrans could only penetrate 5 μm into tumor tissue from the vessel wall (molecular weight of LMN is about 5 MDa) [35]. On the other hand, the vascular hyperpermeability and the lack of functional lymphatic vessels inside tumors also cause interstitial hypertension [36]. While this uniformly elevated interstitial fluid pressure (iFP) reduces convective transport, the dense extracellular matrix hinders the diffusion of nanoparticles [37]. In the case of tumor xenografts, permeable vasculature is more abundant at the invasive front and scarcer in the necrotic core where high iFP builds up (Figure 2.10), leading to heterogeneous accumulation of nanoparticles as seen in our studies (Figure 2.15). In order to overcome these barriers and render LMN an effective targeting agent for tumors, pertinent considerations need to be combined into our future design of the targeting strategy.

While it could be difficult to further decrease the size of LMN for higher vascular permeability due to the minimal amount of payload (SPIO) required for sensitive detection, nanoparticles with positive surface charge exhibit higher permeability and preferentially target tumor vessels compared with their negative or neutral counterparts [38-41]. However cautions should be paid to cationic nanoparticles at the same time, because it has been shown that hemolytic tendency increases in proportion to the positive surface charge [42] and cationic particles are more attractive to phagocytes than neutral particles of the same size [43].

Regarding the characteristic of iFP that greatly hinders the transport of nanoparticles across vessel walls and compromises the benefits of the EPR effect, auxiliary stratagems should be taken to normalize the tumor vasculature and tumor interstitial matrix, so that the efficiency of the vascular network increases, allowing nanoparticles to penetrate faster and deeper inside the tumor [44]. The balance between proangiogenic and antiangiogenic factors is crucial for maintaining the normal architecture of the vascular network in tissue. In tumors, proangiogenic molecules (for example, VEGF, FGF and PDGF) are usually overexpressed, which tips the balance towards the proangiogenic side and causes the formation of chaotic blood vessels. Therefore, judicious application of antiangiogenic agents can restore the balance and revert the vasculature to a more ‘normal’ phenotype [45-46]. To improve particle penetration through the tumor interstitial matrix, there have been some attempts (for example, collagenase [47] and matrix metalloproteinase (MMP) [48]) to degrade these components and thus increase the accessible volume of tissue. Besides that, the hormone relaxin [49-50], which modifies the structure of collagen fibers, as well as tumor penetrating peptide [51] also showed potential to improve the interstitial transport of particles inside tumor. Coadministration of such agents with LMN may help ameliorate tumor structure and accessibility, and thereby increase the targeting efficiency.

5.4 Application of LMN in assessing cerebral inflammation and ischemic reperfusion injury post stroke

As the number one cause for mortality worldwide, cardiovascular disease leads to a fatal outcome mainly through stroke. Thrombolysis can be an effective treatment for acute ischemic stroke, but the resulting reperfusion of the ischemic brain comes with a price - destruction of the microvasculature and extension of infarct volume often occur thereafter [52].

Much evidence suggests that inflammation plays an important role in the pathobiology of ischemic stroke [53-54]. An inflammatory response following the restoration of circulation largely contributes to the ischemic reperfusion injury [55]: the recruitment of leukocytes to the ischemic area leads to the reocclusion of blood vessels, posing a “no-reflow” phenomenon [56] after clot lysis; the same leukocytes also produce proteolytic enzymes, oxygen free radicals and other inflammatory effectors which directly cause endothelial injury in addition to neuronal damage [57-58]. Animal data supporting this contention comes from three lines: notable correlation exists between the time course of leukocyte accumulation and the expansion of brain damage [59-61]; neutropenia ameliorates reperfusion injury [62]; treatments preventing leukocyte adhesion, including neutralization and knockout of ICAM-1, have a cerebral protective effect [63-69]. Even though the combined use of anti-ICAM-1 antibodies with tissue plasminogen activator (tPA) has been shown in many rodent experiments to improve the neurological outcome (suggesting anti-inflammation therapy can extend the therapeutic window for thrombolysis) [70], most biologics for adhesion blockade have been designated as negative in clinical trials [71]. One essential reason for this is that the current regime for applying thrombolysis is within 3 hours of symptom onset [72], while interindividual variability of

hospitalization time and the upregulation of adhesion molecules can be large among stroke patients, compared to experiment animals with guaranteed early reperfusion and close genetic background; however at this time there are no useful implications for measuring these molecules in clinical practice and the limited knowledge we have comes sparsely from postmortem examination. Therefore *in vivo* platforms allowing quantitative examination of the cerebral pattern of ICAM-1, one of the most NF- κ B responsive adhesion molecules, would be significant for post-stroke treatment.

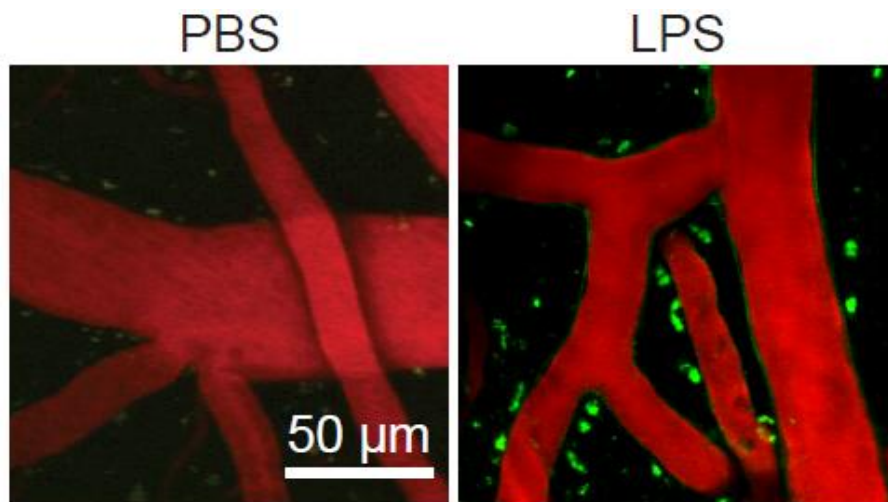


Figure 5.3: Two-photon laser scanning microscopy (TPLSM) imaging of ICAM-1 (FITC-labeled mAb) upregulation in mouse cortical vessels (Texas-red dextran) under systemic LPS-treatment (right panel), which mimics artificially induced acute neuroinflammation. Animal treated with the same volume of PBS (left) was shown as a negative control.

As one crucial ligand for leukocyte adhesion to damaged endothelial tissue, ICAM-1 is upregulated soon after the onset of ischemic stroke [73] (Figure 5.3). LMN

is designed to mimic the behavior of leukocytes in their ability to interact with the high density of ICAM-1 on the inflamed endothelium and macrophages, and is potentially a good imaging contrast agent for both fluorescence imaging and MRI. With our recently developed MRI technique, QSM, the amount of LMN distribution can be measured with sufficient accuracy to allow comprehensive evaluation of inflammation progression and/or regression, thereby enabling real-time assessment of neuroinflammation post stroke. Based on our current observation of LMN in sensing local and systemic acute inflammation, we anticipate a future application of LMN in providing a spatial-temporal map of post-ictus neuroinflammation with the assistance of molecular imaging methodologies, which has not been possible in almost all other imaging studies to date.

5.5 Developing theranostic LMN

Theranostic nanomedicine [74] is emerging as a promising paradigm for therapeutics. One convenience in constructing such function-integrated agents is that many nanoplateforms are already themselves imaging agents. Besides, their well-developed surface chemistry makes it easy to load pharmaceuticals. In such scenario, magnetite nanoparticles, an MRI contrast agent and hyperthermia agent, becomes also an intriguing drug carrier. Furthermore, the combined therapy of high temperature and pharmaceuticals facilitated by theranostic iron oxide nanoparticles can give rise to a synergistic therapeutic effect. In some recent studies, Jain *et al.* [75] loaded doxorubicin (DOX) and paclitaxel (PTX), along with oleic acid coated magnetite nanoparticles, into pluronic-stabilized nanoparticles. Similarly, Yu *et al.* [76] loaded

DOX into anti-biofouling polymer coated iron oxide nanoparticles. When applied in a Lewis lung carcinoma xenograft model, such DOX loaded nanoconjugates showed better pharmacokinetics and therapeutic effects than DOX alone, presumably due to the anti-biofouling feature of the particles.

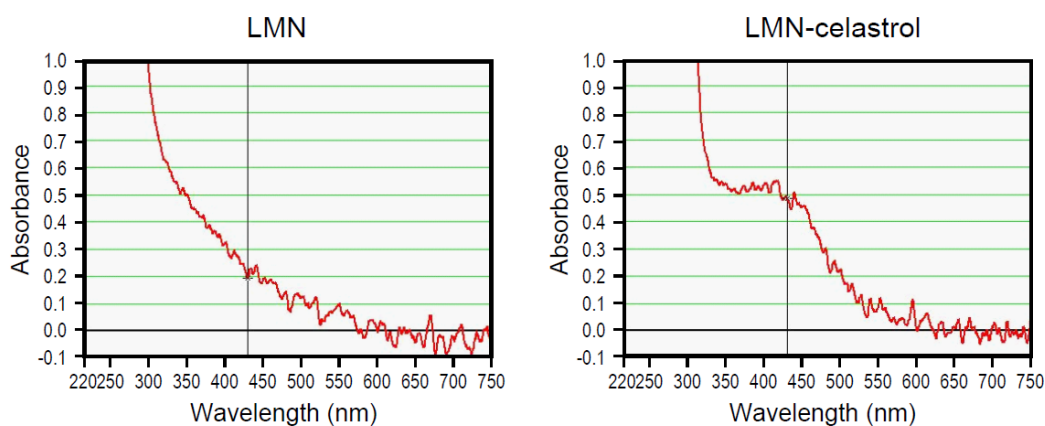


Figure 5.4: Absorbance spectrum of LMN loaded with (right) and without (left) celastrol. Wavelength where celastrol has maximal absorption is marked in black.

In the case of LMN, small molecule anti-inflammation drugs (*e.g.*, celastrol) can be co-loaded with SPIO into the matrix of the nanomicelle during fabrication, rendering it a theranostic agent for inflammatory diseases. As a potent antioxidant and anti-inflammatory drug [77-78], celastrol is poorly water-soluble by itself, and thus exists as aggregates in aqueous solutions. After mixing it with SPIO and lipids in organic solvent, desiccation and rehydration, celastrol will disperse into the hydrophobic space between lipid tails which then protects it from aggregation. Our preliminary data showed that purified LMN loaded with celastrol produced a distinctive absorbance peak at 430 nm, the same wavelength celastrol has maximal

absorption (Figure 5.4). Following the validation of successful drug encapsulation, we estimated the drug loading capacity of LMN to be about 1 μg celastrol per 100 μg SPIO. Using HeLa cell culture, we further confirmed the dose-dependent cytotoxicity of LMN-celastrol (Figure 5.5), supporting our future plan in applying for inflammation-guided cancer therapy.

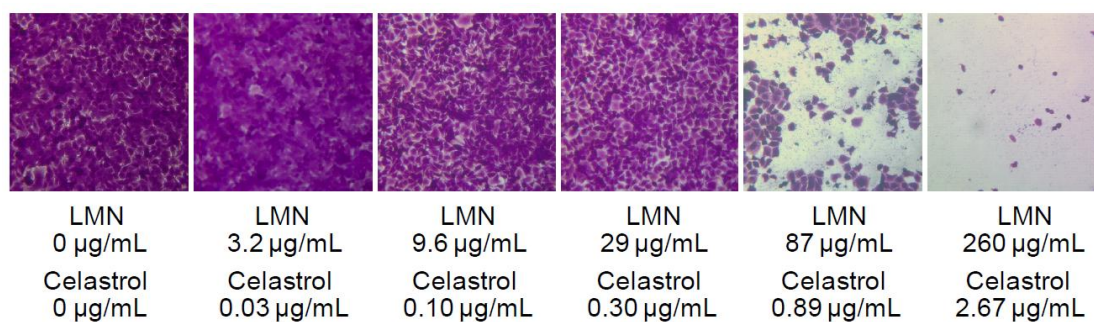


Figure 5.5: Crystal violet staining of HeLa cells after incubation with different amounts of LMN-celastrol for 24 h at 37°C. Dead cells would no longer attach to the surface of flask, thus not appear in the field of view. The concentration of LMN and the corresponding concentration of celastrol are labeled.

REFERENCES

- [1] Clement O, Siauve N, Cuenod CA, Frija G. Liver imaging with ferumoxides (Feridex): fundamentals, controversies, and practical aspects. *Top Magn Reson Imaging*. 1998;9:167-82.
- [2] James ND, Coker RJ, Tomlinson D, Harris JR, Gompels M, Pinching AJ, et al. Liposomal doxorubicin (Doxil): an effective new treatment for Kaposi's sarcoma in AIDS. *Clin Oncol (R Coll Radiol)*. 1994;6:294-6.
- [3] Singer SJ, Nicolson GL. The fluid mosaic model of the structure of cell membranes. *Science*. 1972;175:720-31.
- [4] Fendler JH. Surfactant Vesicles as Membrane Mimetic Agents - Characterization and Utilization. *Accounts Chem Res*. 1980;13:7-13.
- [5] Nakaya T, Li YJ. Phospholipid polymers. *Prog Polym Sci*. 1999;24:143-81.
- [6] Lopez E, O'Brien DF, Whitesides TH. Effects of membrane composition and lipid structure on the photopolymerization of lipid diacetylenes in bilayer membranes. *Biochim Biophys Acta*. 1982;693:437-43.
- [7] O'Brien DF, Klingbiel RT, Specht DP, Tyminski PN. Preparation and Characterization of Polymerized Liposomes. *Ann Ny Acad Sci*. 1985;446:282-95.
- [8] Platt V, Huang ZH, Cao LM, Tiffany M, Riviere K, Szoka FC. Influence of Multivalent Nitrilotriacetic Acid Lipid-Ligand Affinity on the Circulation Half-Life in Mice of a Liposome-Attached His(6)-Protein. *Bioconjugate Chem*. 2010;21:892-902.
- [9] Coussens LM, Werb Z. Inflammation and cancer. *Nature*. 2002;420:860-7.
- [10] Mantovani A, Allavena P, Sica A, Balkwill F. Cancer-related inflammation. *Nature*. 2008;454:436-44.

- [11] Grivennikov SI, Greten FR, Karin M. Immunity, inflammation, and cancer. *Cell*. 2010;140:883-99.
- [12] Hanahan D, Weinberg RA. Hallmarks of cancer: the next generation. *Cell*. 2011;144:646-74.
- [13] Carmeliet P, Jain RK. Angiogenesis in cancer and other diseases. *Nature*. 2000;407:249-57.
- [14] Pirtskhalaishvili G, Nelson JB. Endothelium-derived factors as paracrine mediators of prostate cancer progression. *Prostate*. 2000;44:77-87.
- [15] Massague J. TGFbeta in Cancer. *Cell*. 2008;134:215-30.
- [16] Lee S, Chen TT, Barber CL, Jordan MC, Murdock J, Desai S, et al. Autocrine VEGF signaling is required for vascular homeostasis. *Cell*. 2007;130:691-703.
- [17] Lammert E, Cleaver O, Melton D. Role of endothelial cells in early pancreas and liver development. *Mech Dev*. 2003;120:59-64.
- [18] Natori T, Sata M, Washida M, Hirata Y, Nagai R, Makuuchi M. G-CSF stimulates angiogenesis and promotes tumor growth: potential contribution of bone marrow-derived endothelial progenitor cells. *Biochem Bioph Res Co*. 2002;297:1058-61.
- [19] Koistinen P, Siitonen T, Mantymaa P, Saily M, Kinnula V, Savolainen ER, et al. Regulation of the acute myeloid leukemia cell line OCI/AML-2 by endothelial nitric oxide synthase under the control of a vascular endothelial growth factor signaling system. *Leukemia*. 2001;15:1433-41.
- [20] Maurer CA, Friess H, Kretschmann B, Wildi S, Muller C, Graber H, et al. Over-expression of ICAM-1, VCAM-1 and ELAM-1 might influence tumor progression in colorectal cancer. *Int J Cancer*. 1998;79:76-81.

- [21] Geng JG, Chen M, Chou KC. P-selectin cell adhesion molecule in inflammation, thrombosis, cancer growth and metastasis. *Curr Med Chem*. 2004;11:2153-60.
- [22] Numasaki M, Watanabe M, Suzuki T, Takahashi H, Nakamura A, McAllister F, et al. IL-17 enhances the net angiogenic activity and in vivo growth of human non-small cell lung cancer in SCID mice through promoting CXCR-2-dependent angiogenesis. *J Immunol*. 2005;175:6177-89.
- [23] Salcedo R, Ponce ML, Young HA, Wasserman K, Ward JM, Kleinman HK, et al. Human endothelial cells express CCR2 and respond to MCP-1: direct role of MCP-1 in angiogenesis and tumor progression. *Blood*. 2000;96:34-40.
- [24] Taichman RS, Cooper C, Keller ET, Pienta KJ, Taichman NS, McCauley LK. Use of the stromal cell-derived factor-1/CXCR4 pathway in prostate cancer metastasis to bone. *Cancer Research*. 2002;62:1832-7.
- [25] Roland CL, Harken AH, Sarr MG, Barnett CC, Jr. ICAM-1 expression determines malignant potential of cancer. *Surgery*. 2007;141:705-7.
- [26] Rahn JJ, Shen Q, Mah BK, Hugh JC. MUC1 initiates a calcium signal after ligation by intercellular adhesion molecule-1. *J Biol Chem*. 2004;279:29386-90.
- [27] Pollard JW. Tumour-educated macrophages promote tumour progression and metastasis. *Nat Rev Cancer*. 2004;4:71-8.
- [28] Barnett CC, Moore EE, Mierau GW, Partrick DA, Biffl WL, Elzi DJ, et al. ICAM-1-CD18 interaction mediates neutrophil cytotoxicity through protease release. *Am J Physiol-Cell Ph*. 1998;274:C1634-C44.
- [29] Wu QD, Wang JH, Condrón C, Bouchier-Hayes D, Redmond HP. Human neutrophils facilitate tumor cell transendothelial migration. *Am J Physiol Cell Physiol*. 2001;280:C814-22.

- [30] Kelly CP, O'Keane JC, Orellana J, Schroy PC, 3rd, Yang S, LaMont JT, et al. Human colon cancer cells express ICAM-1 in vivo and support LFA-1-dependent lymphocyte adhesion in vitro. *Am J Physiol*. 1992;263:G864-70.
- [31] Maruo Y, Gochi A, Kaihara A, Shimamura H, Yamada T, Tanaka N, et al. ICAM-1 expression and the soluble ICAM-1 level for evaluating the metastatic potential of gastric cancer. *Int J Cancer*. 2002;100:486-90.
- [32] Hayes SH, Seigel GM. Immunoreactivity of ICAM-1 in human tumors, metastases and normal tissues. *Int J Clin Exp Pathol*. 2009;2:553-60.
- [33] Butler JM, Kobayashi H, Rafii S. Instructive role of the vascular niche in promoting tumour growth and tissue repair by angiocrine factors. *Nat Rev Cancer*. 2010;10:138-46.
- [34] Seymour LW. Passive tumor targeting of soluble macromolecules and drug conjugates. *Crit Rev Ther Drug Carrier Syst*. 1992;9:135-87.
- [35] Dreher MR, Liu W, Michelich CR, Dewhirst MW, Yuan F, Chilkoti A. Tumor vascular permeability, accumulation, and penetration of macromolecular drug carriers. *J Natl Cancer Inst*. 2006;98:335-44.
- [36] Boucher Y, Baxter LT, Jain RK. Interstitial pressure gradients in tissue-isolated and subcutaneous tumors: implications for therapy. *Cancer Res*. 1990;50:4478-84.
- [37] Jain RK. Transport of molecules in the tumor interstitium: a review. *Cancer Res*. 1987;47:3039-51.
- [38] Thurston G, McLean JW, Rizen M, Baluk P, Haskell A, Murphy TJ, et al. Cationic liposomes target angiogenic endothelial cells in tumors and chronic inflammation in mice. *J Clin Invest*. 1998;101:1401-13.

- [39] Campbell RB, Fukumura D, Brown EB, Mazzola LM, Izumi Y, Jain RK, et al. Cationic charge determines the distribution of liposomes between the vascular and extravascular compartments of tumors. *Cancer Res.* 2002;62:6831-6.
- [40] Krasnici S, Werner A, Eichhorn ME, Schmitt-Sody M, Pahernik SA, Sauer B, et al. Effect of the surface charge of liposomes on their uptake by angiogenic tumor vessels. *Int J Cancer.* 2003;105:561-7.
- [41] Schmitt-Sody M, Strieth S, Krasnici S, Sauer B, Schulze B, Teifel M, et al. Neovascular targeting therapy: paclitaxel encapsulated in cationic liposomes improves antitumoral efficacy. *Clin Cancer Res.* 2003;9:2335-41.
- [42] Dobrovolskaia MA, Aggarwal P, Hall JB, McNeil SE. Preclinical studies to understand nanoparticle interaction with the immune system and its potential effects on nanoparticle biodistribution. *Mol Pharm.* 2008;5:487-95.
- [43] Zahr AS, Davis CA, Pishko MV. Macrophage uptake of core-shell nanoparticles surface modified with poly(ethylene glycol). *Langmuir.* 2006;22:8178-85.
- [44] Jain RK, Stylianopoulos T. Delivering nanomedicine to solid tumors. *Nat Rev Clin Oncol.* 2010;7:653-64.
- [45] Jain RK. Normalizing tumor vasculature with anti-angiogenic therapy: a new paradigm for combination therapy. *Nat Med.* 2001;7:987-9.
- [46] Jain RK. Normalization of tumor vasculature: an emerging concept in antiangiogenic therapy. *Science.* 2005;307:58-62.
- [47] Netti PA, Berk DA, Swartz MA, Grodzinsky AJ, Jain RK. Role of extracellular matrix assembly in interstitial transport in solid tumors. *Cancer Res.* 2000;60:2497-503.
- [48] Mok W, Boucher Y, Jain RK. Matrix metalloproteinases-1 and -8 improve the distribution and efficacy of an oncolytic virus. *Cancer Res.* 2007;67:10664-8.

- [49] Brown E, McKee T, diTomaso E, Pluen A, Seed B, Boucher Y, et al. Dynamic imaging of collagen and its modulation in tumors in vivo using second-harmonic generation. *Nat Med.* 2003;9:796-800.
- [50] Perentes JY, McKee TD, Ley CD, Mathiew H, Dawson M, Padera TP, et al. In vivo imaging of extracellular matrix remodeling by tumor-associated fibroblasts. *Nat Methods.* 2009;6:143-5.
- [51] Sugahara KN, Teesalu T, Karmali PP, Kotamraju VR, Agemy L, Greenwald DR, et al. Coadministration of a tumor-penetrating peptide enhances the efficacy of cancer drugs. *Science.* 2010;328:1031-5.
- [52] Jean WC, Spellman SR, Nussbaum ES, Low WC. Reperfusion injury after focal cerebral ischemia: the role of inflammation and the therapeutic horizon. *Neurosurgery.* 1998;43:1382-96; discussion 96-7.
- [53] Lo EH, Dalkara T, Moskowitz MA. Mechanisms, challenges and opportunities in stroke. *Nat Rev Neurosci.* 2003;4:399-415.
- [54] Rossi B, Angiari S, Zenaro E, Budui SL, Constantin G. Vascular inflammation in central nervous system diseases: adhesion receptors controlling leukocyte-endothelial interactions. *J Leukoc Biol.* 2011;89:539-56.
- [55] Dirnagl U, Iadecola C, Moskowitz MA. Pathobiology of ischaemic stroke: an integrated view. *Trends Neurosci.* 1999;22:391-7.
- [56] Ames A, 3rd, Wright RL, Kowada M, Thurston JM, Majno G. Cerebral ischemia. II. The no-reflow phenomenon. *Am J Pathol.* 1968;52:437-53.
- [57] Wang Q, Tang XN, Yenari MA. The inflammatory response in stroke. *J Neuroimmunol.* 2007;184:53-68.

- [58] Wong CH, Crack PJ. Modulation of neuro-inflammation and vascular response by oxidative stress following cerebral ischemia-reperfusion injury. *Curr Med Chem.* 2008;15:1-14.
- [59] del Zoppo GJ, Schmid-Schonbein GW, Mori E, Copeland BR, Chang CM. Polymorphonuclear leukocytes occlude capillaries following middle cerebral artery occlusion and reperfusion in baboons. *Stroke.* 1991;22:1276-83.
- [60] Clark RK, Lee EV, White RF, Jonak ZL, Feuerstein GZ, Barone FC. Reperfusion following focal stroke hastens inflammation and resolution of ischemic injured tissue. *Brain Res Bull.* 1994;35:387-92.
- [61] Zhang RL, Chopp M, Chen H, Garcia JH. Temporal profile of ischemic tissue damage, neutrophil response, and vascular plugging following permanent and transient (2H) middle cerebral artery occlusion in the rat. *J Neurol Sci.* 1994;125:3-10.
- [62] Litt MR, Jeremy RW, Weisman HF, Winkelstein JA, Becker LC. Neutrophil depletion limited to reperfusion reduces myocardial infarct size after 90 minutes of ischemia. Evidence for neutrophil-mediated reperfusion injury. *Circulation.* 1989;80:1816-27.
- [63] Clark WM, Madden KP, Rothlein R, Zivin JA. Reduction of central nervous system ischemic injury by monoclonal antibody to intercellular adhesion molecule. *J Neurosurg.* 1991;75:623-7.
- [64] Bowes MP, Zivin JA, Rothlein R. Monoclonal antibody to the ICAM-1 adhesion site reduces neurological damage in a rabbit cerebral embolism stroke model. *Exp Neurol.* 1993;119:215-9.
- [65] Chopp M, Li Y, Jiang N, Zhang RL, Probstak J. Antibodies against adhesion molecules reduce apoptosis after transient middle cerebral artery occlusion in rat brain. *J Cereb Blood Flow Metab.* 1996;16:578-84.

- [66] Connolly ES, Jr., Winfree CJ, Springer TA, Naka Y, Liao H, Yan SD, et al. Cerebral protection in homozygous null ICAM-1 mice after middle cerebral artery occlusion. Role of neutrophil adhesion in the pathogenesis of stroke. *J Clin Invest.* 1996;97:209-16.
- [67] Soriano SG, Lipton SA, Wang YF, Xiao M, Springer TA, Gutierrez-Ramos JC, et al. Intercellular adhesion molecule-1-deficient mice are less susceptible to cerebral ischemia-reperfusion injury. *Ann Neurol.* 1996;39:618-24.
- [68] Kitagawa K, Matsumoto M, Mabuchi T, Yagita Y, Ohtsuki T, Hori M, et al. Deficiency of intercellular adhesion molecule 1 attenuates microcirculatory disturbance and infarction size in focal cerebral ischemia. *J Cereb Blood Flow Metab.* 1998;18:1336-45.
- [69] Kanemoto Y, Nakase H, Akita N, Sakaki T. Effects of anti-intercellular adhesion molecule-1 antibody on reperfusion injury induced by late reperfusion in the rat middle cerebral artery occlusion model. *Neurosurgery.* 2002;51:1034-41; discussion 41-2.
- [70] Zhang RL, Zhang ZG, Chopp M, Zivin JA. Thrombolysis with tissue plasminogen activator alters adhesion molecule expression in the ischemic rat brain. *Stroke.* 1999;30:624-9.
- [71] Harlan JM, Winn RK. Leukocyte-endothelial interactions: clinical trials of anti-adhesion therapy. *Crit Care Med.* 2002;30:S214-9.
- [72] Khaja AM, Grotta JC. Established treatments for acute ischaemic stroke. *Lancet.* 2007;369:319-30.
- [73] Yilmaz G, Granger DN. Cell adhesion molecules and ischemic stroke. *Neurol Res.* 2008;30:783-93.
- [74] Xie J, Lee S, Chen X. Nanoparticle-based theranostic agents. *Adv Drug Deliv Rev.* 2010;62:1064-79.

[75] Jain TK, Richey J, Strand M, Leslie-Pelecky DL, Flask CA, Labhasetwar V. Magnetic nanoparticles with dual functional properties: drug delivery and magnetic resonance imaging. *Biomaterials*. 2008;29:4012-21.

[76] Yu MK, Jeong YY, Park J, Park S, Kim JW, Min JJ, et al. Drug-loaded superparamagnetic iron oxide nanoparticles for combined cancer imaging and therapy in vivo. *Angew Chem Int Ed Engl*. 2008;47:5362-5.

[77] Allison AC, Cacabelos R, Lombardi VRM, Alvarez XA, Vigo C. Celastrol, a potent antioxidant and anti-inflammatory drug, as a possible treatment for Alzheimer's disease. *Prog Neuro-Psychoph*. 2001;25:1341-57.

[78] Yang HJ, Chen D, Cui QZC, Yuan X, Dou QP. Celastrol, a triterpene extracted from the Chinese "Thunder of God Vine," is a potent proteasome inhibitor and suppresses human prostate cancer growth in nude mice. *Cancer Research*. 2006;66:4758-65.

APPENDIX A

YEAST SURFACE TWO-HYBRID FOR QUANTITATIVE IN VIVO DETECTION OF PROTEIN-PROTEIN INTERACTIONS VIA THE SECRETORY PATHWAY

Published in *Journal of Biological Chemistry*⁴

A.1 Abstract

A quantitative in vivo method for detecting protein-protein interactions will enhance our understanding of protein interaction networks and facilitate affinity maturation as well as designing new interaction pairs. We have developed a novel platform, dubbed "yeast surface two-hybrid (YS2H)," to enable a quantitative measurement of pairwise protein interactions via the secretory pathway by expressing one protein (bait) anchored to the cell wall and the other (prey) in soluble form. In YS2H, the prey is released either outside of the cells or remains on the cell surface by virtue of its binding to the bait. The strength of their interaction is measured by antibody binding to the epitope tag appended to the prey or direct readout of split green fluorescence protein (GFP) complementation. When two alpha-helices forming coiled coils were expressed as a pair of prey and bait, the amount of the prey in complex with the bait progressively decreased as the affinity changes from 100 pM to 10 microM. With GFP complementation assay, we were able to discriminate a 6-log

⁴ This part is modified with the permission of the publisher from Hu X, Kang S, Chen X, Shoemaker CB, Jin MM. Yeast surface two-hybrid for quantitative in vivo detection of protein-protein interactions via the secretory pathway. *Journal of Biological Chemistry*. 2009; 284(24):16369-76. Xiaoyue Chen conducted the experiments with regard to the following figures: A.2a, A.3c & A.4b.

difference in binding affinities in the range of 100 pM to 100 microM. The affinity estimated from the level of antibody binding to fusion tags was in good agreement with that measured in solution using a surface plasmon resonance technique. In contrast, the level of GFP complementation linearly increased with the on-rate of coiled coil interactions, likely because of the irreversible nature of GFP reconstitution. Furthermore, we demonstrate the use of YS2H in exploring the nature of antigen recognition by antibodies and activation allostery in integrins and in isolating heavy chain-only antibodies against botulinum neurotoxin.

A.2 Introduction

A quantitative *in vivo* method for detecting protein-protein interactions will enhance our understanding of protein interaction networks and facilitate affinity maturation as well as designing new interaction pairs. We have developed a novel platform, dubbed “yeast surface two-hybrid (YS2H),” to enable a quantitative measurement of pairwise protein interactions via the secretory pathway by expressing one protein (bait) anchored to the cell wall and the other (prey) in soluble form. In YS2H, the prey is released either outside of the cells or remains on the cell surface by virtue of its binding to the bait. The strength of their interaction is measured by antibody binding to the epitope tag appended to the prey or direct readout of split green fluorescence protein (GFP) complementation. When two α -helices forming coiled coils were expressed as a pair of prey and bait, the amount of the prey in complex with the bait progressively decreased as the affinity changes from 100 pM to 10 μ M. With GFP complementation assay, we were able to discriminate a 6-log

difference in binding affinities in the range of 100 pM to 100 μ M. The affinity estimated from the level of antibody binding to fusion tags was in good agreement with that measured in solution using a surface plasmon resonance technique. In contrast, the level of GFP complementation linearly increased with the on-rate of coiled coil interactions, likely because of the irreversible nature of GFP reconstitution. Furthermore, we demonstrate the use of YS2H in exploring the nature of antigen recognition by antibodies and activation allostery in integrins and in isolating heavy chain-only antibodies against botulinum neurotoxin.

Protein-protein interactions are essential to virtually every cellular process, and their understanding is of great interest in basic science as well as in the development of effective therapeutics. Existing techniques to detect and screen pairs of interacting proteins *in vivo* include the yeast two-hybrid system [1] and protein-fragment complementation assay (PCA) [2-6], where the association of two interacting proteins either turns on a target gene that is necessary for cell survival or leads to the reconstitution of enzymes or green fluorescence protein (GFP) or its variants. The application of protein-protein interactions that are probed with yeast two-hybrid and PCA has been focused mainly on the interactions occurring in the nucleus or cytosol. To study interactions among secretory proteins and membrane-associated proteins, a variant of yeast two-hybrid has been developed for detecting protein-protein interactions occurring in the secretory pathway [7-8]. However, most existing methods are designed to map connectivity information for pairwise interactions and are not suitable for measuring the affinity between two interacting proteins, comparing

interaction strength of different pairs, or ranking multiple binders to the interaction “hub” according to their binding affinity.

Quantitative estimation of protein-protein interactions *in vivo* will require the amount of the complex to be directly measured or the level of reconstituted reporters to be directly proportional to the strength of the interactions. To achieve quantitative analysis of protein interactions in eukaryotic expression system, we have designed a yeast surface two-hybrid (YS2H) system that can express a pair of proteins, one protein as a fusion to a yeast cell wall protein, agglutinin, and the other in a secretory form. When two proteins interact in this system, they associate in the secretory pathway, and the prey that would otherwise be released into the media is captured on the surface by the bait. We have devised two different schemes to quantitatively estimate the affinity of two interacting molecules: flow cytometric detection of antibody binding to the epitope tags fused to the prey and the bait, and the GFP readout from the complementation of split GFP fragments fused to the prey and the bait. They are induced under a bi-directional promoter to promote a synchronized and comparable level of expression.

Herein we demonstrate the quantitative nature of YS2H in predicting the affinity between two interacting proteins, particularly in the range of 100 pM to 10 μ M. This feature allowed us to examine specific interactions between antigen and antibody, to identify hot spots of allosteric activation in integrins, and to isolate camelid heavy chain-only antibodies against botulinum neurotoxin as components of therapeutic agents to treat botulism [9]. With the incorporation of PCA technique into the YS2H, our system may be developed into an *in vivo* tool to measure the kinetics of

protein-protein interactions. Potential applications of YS2H include affinity maturation of antibodies, differentiation of weak to high affinity binders to the hub protein in interaction networks, and confirmation of hypothetical interacting pairs of proteins in a high throughput manner.

A.3 Experimental procedures

A.3.1 YS2H vector design

Plasmid pCTCON was used as a backbone for constructing the YS2H vector (Figure A.1). A PCR fragment containing GAL10 promoter, AGA2, eGFP gene, FLAG tag, and terminator was inserted into the pCTCON by AgeI/KpnI sites. To express prey proteins as secretory forms, AGA2 sequence under the GAL1 promoter was removed by replacing an EcoRI/BamHI fragment with the fragment consisting of a signal sequence, either that of Aga2 or α -1 mating factor, and prey. The cDNA coding for the variable domains of AL-57 was obtained from the expression plasmid (a kind gift from Dr. Shimaoka at Harvard Medical School). The variable domains of TS1/22 were cloned from the hybridoma (ATCC). VH and VL cDNAs were connected with four repeats of a Gly-Gly-Gly-Gly-Ser linker sequence to produce scFv.

A.3.2 Yeast transformation, magnetic affinity cell sorting, and library construction

The plasmid encoding a specific pair of prey and bait proteins was introduced into yeast cells using a commercial reagent (Frozen-EZ Yeast Transformation II Kit, Zymo Research). Transformed yeast cells were grown in a solid medium plate for 48 h. A mutagenesis library of LFA-1 I domain was constructed by electroporation of a

mixture of a MluI/NcoI linearized vector and error-prone PCR products of the I domain (Asn-129-Thr-318) into yeast, as described previously [10]. After transformation, the yeast libraries were grown in selective dextrose liquid medium at 30 °C with shaking for 24 h and induced in selective galactose media for 24–48 h at room temperature with shaking. To construct the variable domain of heavy chain from heavy chain-only antibody (VHH) yeast library, cDNA encoding VHH library was amplified by PCR using primers designed based on the primers used by Maass *et al.* [11]. VHH cDNA PCR product was first ligated into the YS2H vector using NheI/BamHI sites and then was transformed into XL1-Blue (Stratagene) by electroporation. The plasmids extracted from $\sim 5 \times 10^6$ colonies were transformed into EBY100 by a lithium acetate method [12]. A single colony of EBY100 from fresh plate was inoculated into 10 ml of YPDA medium and cultured at 30 °C with shaking at 225 rpm for 16 h. The cells were then inoculated into 100 ml of YPDA at 0.5 OD₆₀₀ and cultured for another 4 h until A₆₀₀ reaches 2. The cells were washed twice in water and resuspended in 10.8 ml of transformation mix buffer (7.2 ml of 50% polyethylene glycol, 1.1 ml of 1 M LiAc, 1.5 ml of 2 mg/ml single strand carrier DNA, and 150 µg of library plasmid in 1.0 ml water). The mixture was then incubated at 42 °C for 50 min. After incubation, the cells were cultured into 100 ml of selective dextrose liquid medium for 24 h and induced in selective galactose medium for 24–48 h. Library construction by homologous recombination or the lithium acetate method produced a library size of 10^6 – 10^7 . The libraries of LFA-1 I domain and VHH were sorted with anti-Myc antibody using magnetic affinity cell sorting as described previously [10].

A.3.3 Immunofluorescence flow cytometry

Antibodies used in this study were the anti-c-Myc antibody 9E10 (ATCC), anti-FLAG, and phycoerythrin-labeled goat polyclonal anti-murine antibodies (Santa Cruz Biotechnology, Santa Cruz, CA). To measure the surface expression of specific prey and bait proteins using flow cytometry, one to five colonies from solid medium plate were inoculated together to obtain averaged values. After induction, the cells were harvested, washed in 100 μ l of the labeling buffer (phosphate-buffered saline with 0.5% bovine serum albumin), and then incubated with ligands at 10 μ g/ml in 50 μ l of the labeling buffer for 20 min with shaking at 30°C. The cells were then washed and incubated with secondary antibodies at 5 μ g/ml in 50 μ l of the labeling buffer for 20 min at 4°C. Finally, the cells were washed once in 100 μ l and suspended in 100 μ l of the labeling buffer for flow cytometry (FACScan, BD Biosciences). For detecting TS1/22 binding (Figure A.5b), goat polyclonal anti-murine antibody was used as a primary antibody.

A.3.4 Protein expression

The I domains were expressed in *Escherichia coli* BL21 DE3 (Invitrogen) as inclusion bodies and refolded and purified by an S75 size exclusion column connected to fast protein liquid chromatography (GE Healthcare) [10]. AL-57 as a single-chain format (scFv AL-57) was expressed using the protocol for I domain production, except that 3 mM cystamine and 6 mM cysteamine were added to the refolding buffer. Full-length BoNT/A and BoNT/B-LC encoding DNA (amino acids 1–448 of A-LC and 1–440 of B-LC) were synthesized employing codons optimal for expression in *E. coli*. A-LC and B-LC containing hexahistidine tags at both termini were produced using a pET14b vector. To express VHHs in soluble forms, we inserted VHH cDNA into the

pET20b expression vector (Novagen). Soluble VHH was expressed in *E. coli* BL21 DE3, extracted by sonication, and purified using a nickel nitrilotriacetic acid column. Eluted VHHs were then injected into an S75 size exclusion column for further purification.

A.3.5 SPR analysis

A protein-coupled or a control mock-coupled CM5 sensor chip was prepared using an amine coupling kit (BIAcore, Piscataway, NJ), as described previously [10]. SPR was measured using a Biacore (BIA2000). I domains were injected over the chip in 20 mM Tris-HCl, pH 8.0, 150 mM NaCl, 10 mM MgCl₂ at a flow rate of 10 µl/min at room temperature. VHHs were injected over the chip in 20 mM Tris-HCl, pH 8.0, 150 mM NaCl at a flow rate of 10 µl/min at room temperature. The chip surface was regenerated by flowing 20 µl of 10 mM Tris-glycine, pH 1.5 buffer.

A.4 Results

A.4.1 The design of the YS2H

YS2H is built on a yeast display system [13-14], which expresses, under the control of the GAL1 promoter, a protein of interest as a fusion to Aga2. Aga2 connects to the β-glucan linked Aga1 to form a cell wall protein called agglutinin. To extend this methodology to the expression of a pair of proteins, we have inserted into the yeast display vector, pCTCON [13], an additional expression cassette under the GAL10 promoter [15]. We observed comparable expression of eGFP by GAL1 and GAL10 promoters using two different plasmids that were constructed to express eGFP under either GAL1 or GAL10 promoters (data not shown). The final YS2H vector

(Figure A.1a) was designed to express the bait protein under the GAL10 promoter as a fusion to Aga2 and the prey protein under the GAL1 promoter without Aga2 fusion.

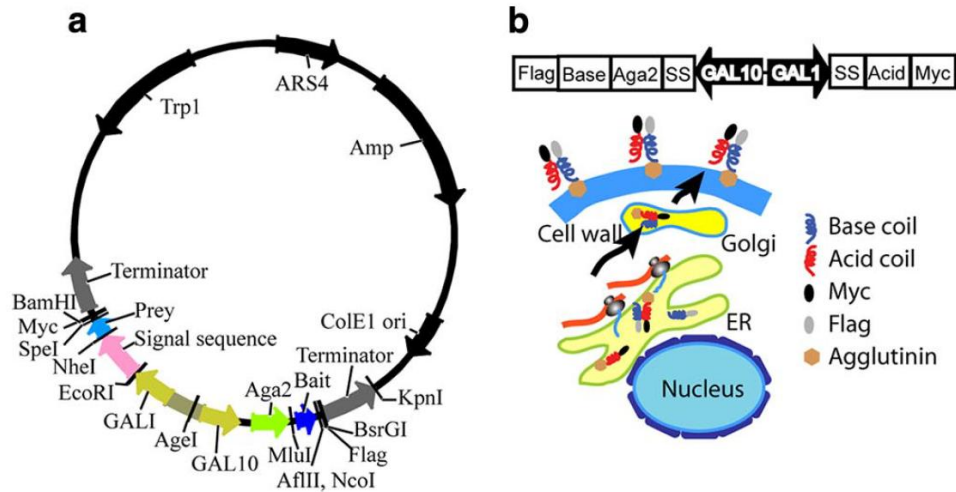


Figure A.1: (a) A map of the YS2H vector is drawn with restriction enzyme sites and genes labeled. The bait protein is expressed as a fusion to Aga2 on cell surface, whereas the prey protein is expressed as a secretory form. (b) Schematic diagram of the expression cassette and protein-protein interactions (acid base coiled coils) via the secretory pathway is depicted. The prey bound to the bait is detected by antibody binding to the Myc tag. FLAG (DYKDDDDK) and Myc (EQKLISEEDL) epitope tags are fused to the C-terminal of the bait and prey proteins, respectively, and are used to measure the surface expression of the bait and the amount of the prey that is bound to the bait.

The signal sequence used is either that of Aga2 or the α -1 mating factor [16]. The expression level of prey proteins with α -1 mating factor was comparable with those containing Aga2 signal sequence (data not shown). FLAG and Myc tags are fused to the C-terminal of the bait and prey proteins, respectively, and are used to examine the surface expression of the bait and the amount of the prey that is bound to the bait

(Figure A.1b). To incorporate the PCA technique into the YS2H system, we inserted the sequence encoding enhanced eGFP fragments [3] downstream of the bait (NeGFP contains residues Val-2 to Ala-155) and the prey (CeGFP with Asp-156 to Lys-239) to monitor their interaction by GFP readout (Figure A.2a). The deletion of the secretory signal sequence of the prey and bait proteins causes this pair to express in the cytosol (Figure A.2b), which can be used to compare protein-protein interactions occurring in the secretory pathway *versus* cytosol.

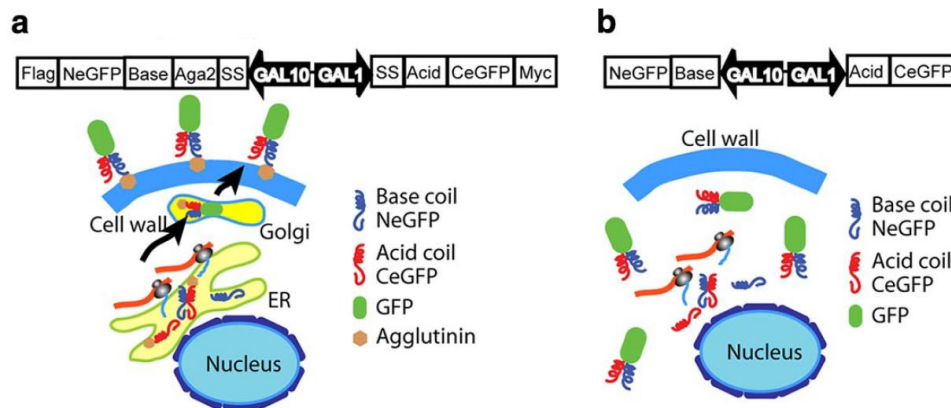


Figure A.2: (a) Schematic diagram of the expression cassette and protein-protein interactions (acid base coiled coils) via the secretory pathway is depicted. The prey bound to the bait is detected by direct GFP readout from split GFP complementation. (b) The deletion of signal sequence for the prey and bait proteins leads to their expression in the cytosol.

A.4.2 The validation of the yeast surface two-hybrid system using coiled coil interaction

To validate that antibody binding to the Myc tag or GFP readout correlates with the strength of molecular interactions in YS2H, we expressed five pairs of acid (En) and base (Kn) α -helices of varying heptad repeats (n) that associate into coiled

coils (Figure A.3). These coiled coils have been designed *de novo* to have affinities (K_D) in the range of 100 pM (E5/K5) to 100 μ M (E3/K3) with higher affinity for longer helices through hydrophobic interactions at the interface and electrostatic attraction between the oppositely charged residues from each helix [17]. Myc expression (mean fluorescence intensity (MFI), measured by antibody binding to Myc tag) exhibited a strong correlation with the interaction affinity within the range of 100 pM to 10 μ M K_D for E5-K5 to E5-K3 (Figure A.3b & A.4a). With GFP complementation, this correlation extended beyond 10 μ M K_D , and the difference between E5-K3 and E3-K3, corresponding to the affinity range of 10 μ M to 100 μ M, was clearly discernible (Figure A.3c & A.4b). The Myc expression and GFP complementation were close to the level of background when the acid coil (K3 in Figure A.3b & A.3c) was deleted, indicating a lack of spontaneous complementation of the two split GFP. The level of surface expression of the bait protein measured by antibody binding to the FLAG tag was relatively invariant (Figure A.3b & A.3c), supporting the idea that the difference in the amount of the prey protein is solely due to the difference in its affinity to the bait. In contrast to a quantitative correlation between the strength of protein-protein interactions and GFP complementation, the acid and base coil interactions occurring in the cytosol (expression of the coils without secretory signal sequence) led to the complementation of split GFP that lacks correlation with the strength of coiled coil interactions (Figure A.3d & A.4c). However, GFP complementation for these pairs was still due to specific interaction between acid and base coils, evidenced by the absence of fluorescence when the base coil was deleted from NeGFP (Figure A.4d).

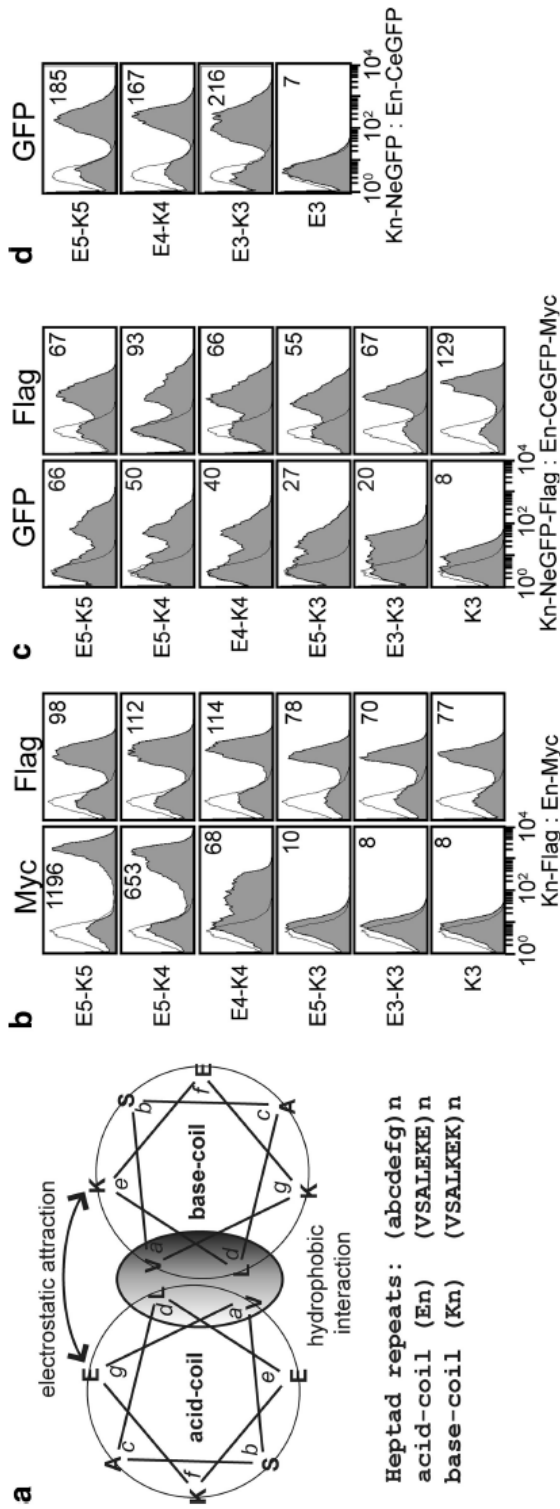


Figure A.3: Detection of coiled coil interactions by epitope expression and GFP complementation. (a) A schematic diagram (adapted from De Crescenzo *et al.* [17]) of the acid (En)-base (Kn) coiled coils with n indicating the number of heptad repeats. (b-c) The detection of coiled coil interactions by antibody binding to Myc tag (b) or direct GFP readout (c) using flow cytometry. Antibody binding to the FLAG tag measures the level of the base coil expression on cell surface. (d) Shown are the plots of GFP complementation caused by the coiled coil interactions occurring inside the cells. The numbers in each plot (b-d) indicate the MFI of an entire population shown in filled histogram. The thin lines represent the histograms of uninduced clones. The pairs of bait and prey are denoted for each column as bait:prey. The labels K3 and E3 indicate that the other coil is deleted from the expression vector.

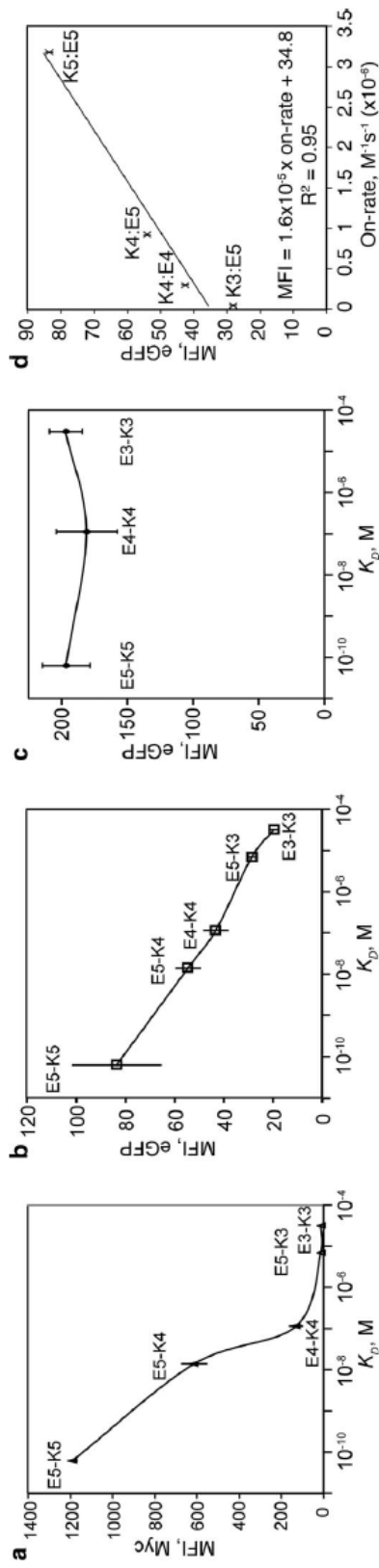


Figure A.4: The correlation of the affinity measured by SPR [17] with the detection by epitope tag or direct readout of GFP complementation caused by coiled coil interactions occurring in the secretory pathway (a, b, & d) or in the cytosol (c). The data are from three independent experiments involving different clones (means \pm SE). The smooth solid lines are drawn by connecting data points. (d) The MFI of eGFP complementation from the coiled coil interactions is plotted as a function of their on-rate, measured by SPR [17]. The solid line represents a least square fit to the data points.

A.4.3 YS2H detects specific interactions of antibodies and antigens

To investigate a potential use of YS2H for antibody discovery, we first examined whether YS2H can detect specific interactions of known pairs of antigen and antibody. As a model system, we chose a ligand-binding domain of the integrin LFA-1, known as the Inserted or I domain, and monoclonal antibodies specific to LFA-1 I domain (Figure A.5). The I domain exists in two distinct conformations that correspond to low and high affinity states to its ligand, intercellular adhesion molecule-1 (ICAM-1) (Figure A.6). Although the I domain in isolation is predominantly in an inactive, low affinity conformation, the mutations that would

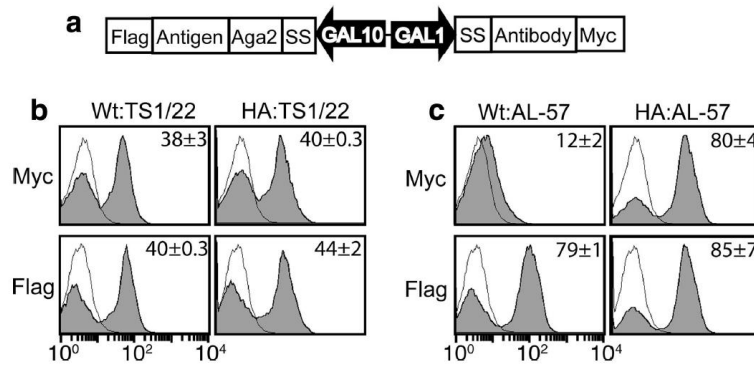


Figure A.5: Detection of specific interactions between antibodies and antigens in YS2H. (a) Schematic diagram of the expression cassette used to study antigen (bait) and antibody (prey) interactions. (b-c) Shown are the histograms of the interactions of the wild-type and the high affinity (HA) I domains as baits and activation-insensitive antibody, TS1/22 (b) activation-specific antibody, AL-57 (c) as preys. Filled histograms are of antibody binding to Myc and FLAG tags to the induced clones. Thin black lines represent antibody binding to uninduced clones as controls. The numbers in each plot indicate the means \pm SE of the MFI of the filled histograms from three independent measurements.

favor the active conformation were found to induce high affinity binding of the I domain to the ICAM-1. For example, the mutations of K287C and K294C (high affinity or HA I domain) designed to stabilize by disulfide bond the position of the $\alpha 7$ -helix into active conformation led to an increase in the affinity to ICAM-1 by 10,000-fold over the wild-type I domain [18].

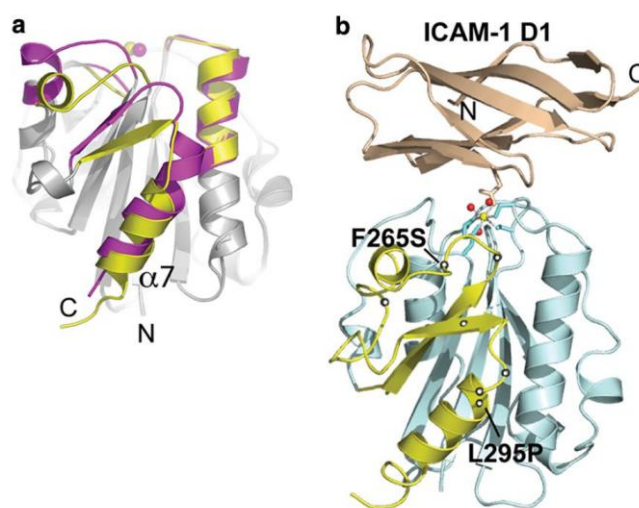


Figure A.6: (a) Cartoon diagrams of low (inactive) and high affinity (active) conformations of the LFA-1 I domains. The regions that are structurally conserved between two states are colored gray. The regions that differ structurally are colored in magenta and yellow for the inactive and the active conformations, respectively. The metal ions in the metal ion-dependent adhesion site are shown as spheres. The N and C termini and $\alpha 7$ -helix are labeled. (b) The structure of the I domain is shown in complex with the first domain of ICAM-1 (D1). Gray spheres with a white center display the positions for the hot spots for allosteric activation found in our previous study [10]. The metal ion and three oxygen atoms of water molecules are depicted as spheres. The residues that coordinate to the metal ion are shown in stick models. The structures of the I domains and the complex of I domain with the ICAM-1 were modeled based on the crystal structures, as described previously [31].

The antibodies that were expressed as scFv formats include the activation-insensitive antibody (TS1/22) [19], binding to both inactive and active I domains, and the activation-dependent antibody (AL-57) [10, 20], which binds only to the active I domain. The interaction between antigen and antibody was measured by the detection of Myc tag fused to the antibody at the C terminus (Figure A.5). A tag-based assay was chosen instead of GFP complementation because it was found that the I domain fused to NeGFP did not express (no antibody binding to FLAG tag), presumably because of the quality control machinery in protein secretion [21] that prohibits misfolded proteins to be secreted (data not shown). This is in contrast to the expression of split GFP with a fusion of short coils, *e.g.* K3-NeGFP in Figure A.3c. Therefore, it appears that when NeGFP is fused to the I domain that by itself requires proper folding for secretion, the I domain fusion to NeGFP becomes completely misfolded and does not pass the quality control for secretion.

Myc tag expression in YS2H was in agreement with the specificities of monoclonal antibody AL-57 and TS1/22 against the LFA I domain; although the clones expressing TS1/22 displayed Myc expression either with the wild-type or with the HA I domains as antigens (Figure A.5b), the AL-57 clones exhibited Myc expression only with the HA I domain (Figure A.5c).

A.4.4 Discovery of activating mutations in the LFA-1 I domain

Next, we examined the ability of our system in isolating activating mutations in antigens that exhibit two different activation states. With the expression of AL-57 scFv and the error-prone PCR products of the wild-type I domain in YS2H, yeast library was constructed and sorted with anti-Myc antibody using a magnetic affinity

cell sorter. With successive sorting, there was a gradual increase in the percentage of the population of cells that showed Myc expression above the background level (Figure A.7a). After two rounds of sorting, the cells were plated to yield individual clones, from which four clones were sequenced and tested for Myc expression. Of the four, three contained a mutation of F265S, and one contained L295P (Figure A.7b). These two mutations belonged to a long list of activation hot spots that were identified in our previous study [10], where a large number of yeast cells were sorted and

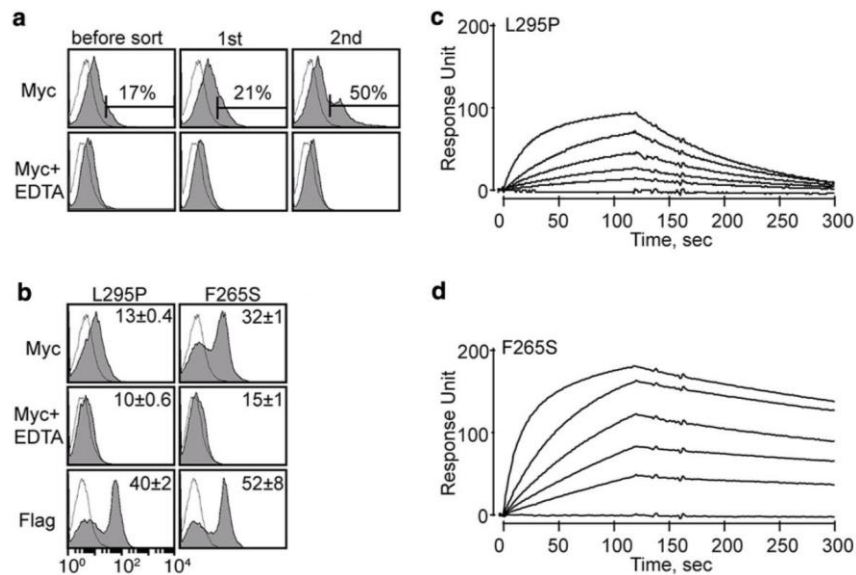


Figure A.7: (a) Myc expression of the I domain library before sort and after first and second sort are shown. The numbers indicate the percentage of the clones within the gated region. Antibody binding was measured with 10 mM MgCl₂ or no metal ions with 10 mM EDTA. (b) Two activating mutations from the second sort were of F265S and L295P. The numbers in each plot indicate means \pm SE of the MFI of the filled histograms from three independent measurements. (c-d) SPR measurements of L295P (c) and F265S (d) binding to scFv AL-57. I domains were injected over the scFv AL-57-coated chip as a series of 2-fold dilutions beginning at 500 nM.

analyzed for their binding to exogenous AL-57 or ICAM-1-Fc γ .

The mutations of L295P and F265S were previously found to contribute to an increase in the binding of the I domain to ICAM-1 at 6 and 152%, respectively, of the HA I domain binding to ICAM-1 [10]. To directly measure the affinity of scFv AL-57 to I domain variants, we used a SPR technique (Figure A.7c & A.7d). A first order Langmuir adsorption equation was fitted to the sensograms to obtain the kinetic and equilibrium binding constants. The equilibrium dissociation constants (K_D) of L295P and F265S to scFv AL-57 were 243 and 15.7 nM, respectively, in agreement with higher Myc expression with F265S in our system. AL-57 binding to the LFA-1 I domain depends on the presence of metal ions at the top of the I domain, known as the metal ion-dependent adhesion site (Figure A.6b) [22]. This was also confirmed by the decrease in the Myc tag expression when EDTA was added at 10 mM to the cells during labeling (Figure A.7a & Figure A.7b).

A.4.5 Antibody discovery: VHH against Botulinum neurotoxin protease

Approximately half of the IgGs in camelid sera are heavy chain-only antibodies devoid of light chains [11, 23]. Because of the lack of light chains, antigenic specificity of the heavy chain-only antibodies is limited to a variable domain of the heavy chain. We are seeking VHH agents that bind and inhibit the LC protease domains of Botulinum neurotoxins (BoNTs) as components in therapeutic agents for the treatment of botulism. In prior work (Maass *et al.* [11], we immunized alpacas with BoNT LCs of serotype A (A-LC) followed by serotype B (B-LC). We then used phage display techniques to identify VHHs from these alpacas with affinity for the BoNT LC proteases. We selected two A-LC binding VHHs (B8 and G6) and two B-

LC binding VHHs (B10 and C3) for testing with the YS2H system (Figure A.8a). Myc tag expression was found to be highest in the clone expressing VHH-B8 and BoNT/A-LC, whereas the binding level of the other VHHs was lower with MFI ranges from 14 to 29.

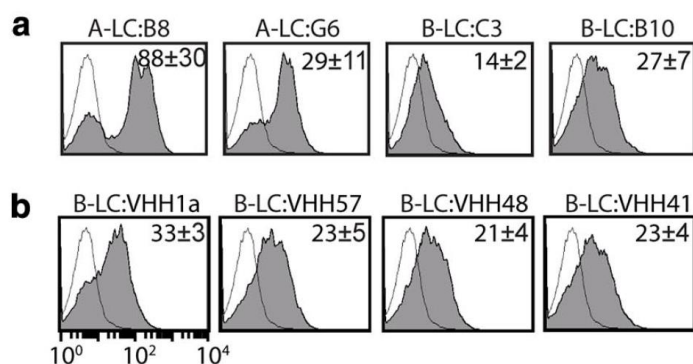


Figure A.8: (a) Specific binding of the VHHs against A-LC and B-LC was confirmed in YS2H by Myc expression. (b) New VHHs against B-LC protease were isolated by YS2H. The numbers in each plot indicate means \pm SE of the MFI of the filled histograms from three independent measurements.

To confirm that the level of Myc expression correlates with the solution affinity of VHH to LC, we used a SPR technique (Figure A.9). A series of 2-fold dilutions of A-LC was injected into a chip coated with B8 and G6. The K_D values of B8 and G6 to BoNT/A-LC were estimated to be 2.3 and 230 nM, respectively. The 100-fold difference in the affinity was mainly due to the 34-fold difference in the dissociation rate ($k_{\text{off}} = 5.18 \times 10^{-4} \text{ s}^{-1}$ for B8 *versus* $1.82 \times 10^{-2} \text{ s}^{-1}$ for G6), with the association rate differing by only 3-fold ($k_{\text{on}} = 2.26 \times 10^5 \text{ M}^{-1} \text{ s}^{-1}$ for B8 *versus* $7.61 \times 10^4 \text{ M}^{-1} \text{ s}^{-1}$ for G6).

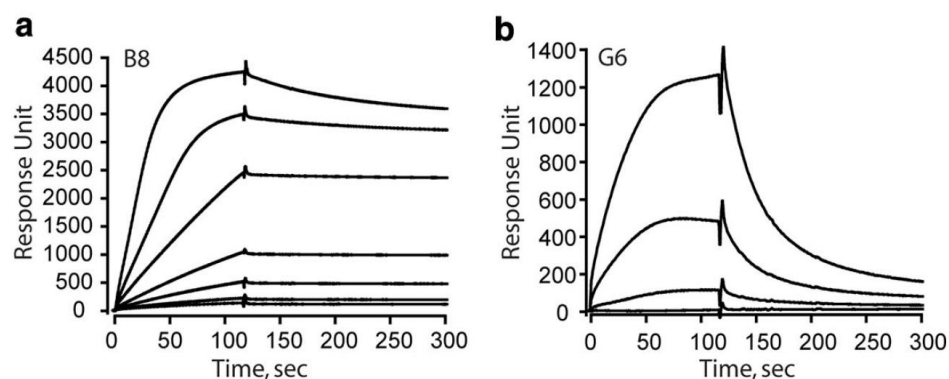


Figure A.9: SPR measurements of B8 (a) and G6 (b) binding to BoNT/A-LC. A-LC was injected at a series of 2-fold dilutions beginning at 160 nM to the B8-coated and 400 nM to the G6-coated chip.

To validate the use of YS2H for antibody discovery, a yeast antibody library was constructed by transforming cells with the alpaca immune cDNA library as prey and the BoNT/B-LC gene as bait. Yeast cells enriched after two rounds of magnetic affinity cell sorting with anti-Myc antibody began to show an increase in Myc tag expression (data not shown). Of 30 clones that were tested individually, 14 clones displayed positive expression of Myc tag. Eleven of these 14 clones were found to be unique clones, including B10 and C3, which were originally isolated by phage display. Anti-Myc antibody binding of the newly isolated nine clones was in the range of 21–33 MFI units, which is lower than that of B8 binding to A-LC (Myc expression of four selected clones are shown in Figure A.8b). Overall, anti-B-LC VHHs isolated by both the phage display and YS2H were low affinity binders ($K_D = 100$ nM to 1 μ M), suggesting a lack of the high affinity binders to B-LC protease in alpaca immune library.

Sequence analysis of the VHHs identified by phage or YS2H revealed that VHHs contain two, four, or six cysteines, which would result in up to two extra disulfide bonds in addition to the one that is conserved in all immunoglobulin fold domains (Figure A.10). We found that of the nine VHHs newly isolated by our YS2H system, three VHHs contain six cysteines, and the other six VHHs contain four cysteines. In contrast, either two or four cysteines were dominant in VHHs that were isolated by phage display. The VHHs identified by a phage display system may be limited to those that fold properly in a bacterial expression system. VHHs containing extra disulfides may fold improperly in bacteria, whereas the formation of correct disulfide bonds is much less problematic in yeast.

	FR1	CDR1	FR2	CDR2	FR3				
1	QTEVQLVESGGALVQPGGSLTLS	CVSSGSSLD	YAIGWFRQAPGKDRIGAP	CIGSDGSATNYVGDASYRFTISRE					
1	QAEQLVLES	GGGSVHPGESLRLS	CAGSGSLFGY	YAIGWFRQAPGKE	CEGVSLSPNGDETRYASSVKDRFIISRD				
1	QAEVQLVESGGGLVPEPGGSLSL	SC	TASEFFLDFYAVAWFRQAPGKEREGIS	CISGTDASADYKDSVKGRFTISRD					
1	QTQVQLVESGGGLVQPGGSLNLS	CSASGGTF	-YYAIGWFRQAPGKEREEVS	CISSSGGSPDYSDSVKGRFTTISR					
1	QAHVQLQQSGGGLVQPGGSLRLS	CAASGFTLDY	YAIGWFRQAPGKEREGV	CISSSGGSTYYADSVKGRFTISR					
1	QAHVQLQQSGGGLVQPGGSLRLS	CAASGSIF	SYAMGWYRQAPGKQRELVA	AISSYG-STNYADSVKGRFTISR					
1	--QLQLVESGGGMVQPGGSLRLS	CAASGFTF	STYDMSWVRQAPGKPEWVSI	INAGGGSTYYAASVKGRFAISR					
1	--QVQLVESGGGLVQPGDSLTL	SCAVSGFS	FSSYKMSWVRQTPGKGLEWVSS	INSGGGTNYADSVKGRFTISR					
	FR3	CDR3	FR4						
76	--KNTVYLQMDSLKTD	D	TAVYSCAAYS	---	TGWGPN	CESLDGTVAWGKGPVTVTS	VHH1a		
76	NAKNTVYLQMN	SLKPEDTGVYY	CADD	----	PCSSGIW	GPLKCY	SAGQGTETVTVSS	VHH48	
76	DAKGTVYLQMN	NLKPEDTAVYY	CAAP	-ADCG	CSGYM	CDN	----	RYWGQGTQVNVSS	VHH57
75	VAKKTVYLQMN	SLRPEDTALY	QC	ATVRP	GPQC	SGYVC	QDT	CAFGSWGQGTQVTVSS	VHH41
76	NAKNTVYLQMN	SLKPEDTAVYY	CA	-----	VAQSC	LRGGV	-RGGYWGQGTQVTVSS	G6	
75	NAKNTVYLQMN	SLKPEDTAVYY	CN	-----	ADIAT	MTAVG	-GFDYWGQGTQVTVSS	B8	
74	NAKNTLYLQMN	NLKPEDTALY	CARV	-ASY	CRGYV	CSPP	-EFDYWGQGTQVTVSS	B10	
74	NAKNMLYLQMN	NLKPEDTAVYY	CA	-----	H	-RVVTG	QLD-LYDYWGQGTQVTVSS	C3	

Figure A.10: Sequence analysis of VHHs. Cysteines are highlighted in yellow for the pair that forms a conserved disulfide bond or in orange that forms extra disulfide bonds. The framework region (FR) and complementarity determining regions (CDR) are noted.

A.5 Discussion

Here we demonstrate that our novel system, YS2H, is highly efficient in the detection and discovery of protein-protein interactions. The quantitative nature of YS2H is from the fact that protein-protein interactions occur via a secretory pathway, and the amount of the prey protein in complex with the bait is determined by the equilibrium affinity between the two. With the use of a PCA technique, our system may be designed to discriminate different pairs of protein-protein interactions according to their kinetics of binding.

The utility of *in vivo* methods for quantitative estimation of binding affinity extends to the cases where one aims to increase the affinity of weak interactions between antigen and antibody and to engineer high affinity ligands and receptors that can potentially serve as agonists or antagonists. As an example, a prokaryotic system capable of co-expression of antigens anchored on the inner membrane of bacteria and single chain variable fragments (scFv) as soluble form was efficient in affinity screening and maturation [24]. Therefore, co-expression of antigen and antibody through eukaryotic secretory system will further enable screening of antibody libraries against the proteins that require eukaryotic folding machinery or that undergo post-translational modifications.

The amount of the prey bound to the bait in our system follows the Langmuir binding isotherm model. With the expression system used in this study, the concentration of prey proteins released into the media is far larger than that of the bait proteins, which is fused to Aga2. Under the mating conditions, the number of agglutinin goes up to 10,000 copies/cell [25], which approximates the concentration of

the bait proteins to be 1.7 nM at 10^8 cells/1 ml of culture medium. The Langmuir equation is then given by $[\text{bait:prey}]/[\text{bait}] = [\text{prey}]/([\text{prey}] + K_D)$ where $[\text{bait:prey}]$, $[\text{bait}]$, and $[\text{prey}]$ denote the concentrations of the bait in complex with the prey, the bait, and the prey, respectively. By replacing $[\text{bait:prey}]$ and $[\text{bait}]$ with antibody binding to Myc (MFI_Myc) and FLAG tag (MFI_FLAG), respectively, and taking into consideration of the MFI ratio (α) of anti-Myc to anti-FLAG antibody binding to equal copies of Myc and FLAG tags, the Langmuir equation rearranges into $1/\text{MFI_Myc} = \alpha^{-1}(1+K_D/[\text{prey}])/\text{MFI_FLAG}$. From this equation (with measured values of $\alpha = 15$ and $[\text{prey}] = 10$ nM), the K_D values predicted for coiled coil interactions (E5-K5, E5-K4, E4-K4, and E5-K3) closely approximated the K_D values measured by SPR [17] (Table A.1). The quantitative nature of YS2H in measuring protein-protein interactions extends to antigen and antibody interactions. The binding affinity of scFv TS1/22 to the wild-type and HA I domain, scFv AL-57 to the HA I domain, and the F265S ranged between 148 and 237 nM K_D , whereas it was 440 nM for the binding of L295P to scFv AL-57. SPR measurement of the binding of I domain variants to scFv AL-57 estimated that although F265S and HA I domains have comparable affinity to scFv AL-57, L295P showed much lower affinity (Figure A.7c & A.7d, Table A.1). The predicted affinity for VHH-B8 and VHH-G6 binding to A-LC is 38 and 143 nM, compared with the measured K_D of 2.3 and 230 nM, respectively. Overall, the affinity predicted by the level of antibody binding to Myc and FLAG tag in our system agreed well with the measured affinity in the range of 1 nM to 1 μM K_D (Table A.1).

Although antibody binding to the Myc tag for protein-protein interactions

Table A.1: Comparison of equilibrium dissociation constants (K_D) predicted from YS2H *versus* directly measured using surface plasmon resonance

Interaction pairs	Predicted from YS2H (means \pm SE)	SPR measurements
	nM	nM
E3-K3	1269.5 \pm 53	32000 \pm 3000 ^a
E5-K3	1292.8 \pm 37	7000 \pm 800 ^a
E4-K4	150.7 \pm 48	116 \pm 8 ^a
E5-K4	18.3 \pm 3	14 \pm 1 ^a
E5-K5	0.49 \pm 0.2	0.063 \pm 0.005 ^a
HA-AL57	150.9 \pm 8	32.6 \pm 0.28 ^b
F265S-AL57	237.4 \pm 11.6	15.7 \pm 0.03 ^b
L295P-AL57	439.7 \pm 13.6	243 \pm 3.9 ^b
VHH-B8-A-LC	38.2 \pm 13.3	2.3 \pm 0.08 ^b
VHH-G6-A-LC	143.0 \pm 41.9	230 \pm 1.3 ^b

^a The values are from the paper by De Crescenzo *et al.* [17]. Shown are the means \pm 95% confidence interval.

^b The values are measured from this study. Shown are the means \pm SE, estimated from BIAevaluation software from Biacore.

higher than 10 μ M K_D reduced to the level of background (Figure A.4a), the detection by GFP complementation spanned a larger range of affinities, exhibiting a linear decrease in the fluorescence with an increase in K_D in log scale (Figure A.4b). This is attributed to the fact that reconstituted GFP does not dissociate (or complementation is irreversible), such that the complemented GFP is functional whether or not the prey and the bait exist as a complex on the cell surface. Therefore, the dominant factor that determines GFP reconstitution will be the rate at which two coils associate (on-rate) to initiate split GFP assembly. Notably, when the MFI of reconstituted GFP was plotted

against the measured on-rates [17] for E5-K5, E5-K4, E4-K4, and E5-K3 (on-rate is unavailable for E3-K3), a linear trend was obtained with a R^2 value of 0.95 (Figure A.4d). However, the use of GFP complementation was limited to the study of coiled coil interactions, because the I domain fused to the split GFP did not express on the surface. Therefore, to apply a PCA technique to detect diverse protein-protein interactions through the secretory pathway, split GFP needs to be optimized not to interfere with the folding of the bait and prey proteins. The additional parameter to be optimized is the length of the linker connecting split GFP to the proteins to enable GFP complementation for a wide range of size variation in proteins and topological variation between the binding interface and the GFP fusion site [6].

The fact that GFP complementation occurs by protein-protein interaction through the secretion process explains its quantitative correlation with the strength of protein-protein interactions. This is in contrast to a previous finding [4] that GFP complementation from protein interactions occurring in the cytosol only indicates the presence of the interaction, and fluorescence intensity is relatively invariant with the affinity of two proteins. Indeed, when the two coils were expressed in the cytosol with the deletion of the secretory signal sequence, we found that overall fluorescent intensity was higher, and the complementation of split GFP lacked correlation with the strength of coiled coil association (Figure A.3d & A.4c). Because of the irreversible complementation of split GFP, after 24–48 h of induction, it is the concentration of two interacting proteins in the cytosol that determines the GFP complementation rather than their interaction strength.

Systems such as ribosomal [26], phage [27], and yeast [14] displays provide efficient means to couple genotype and phenotype and to screen library for protein engineering and antibody discovery. A typical screening process of antibody libraries requires exogenous antigens in their soluble form. Co-expression of two proteins within the same display system, *e.g.* the fusion of antigen and antibody into split phage coat protein [28] and the expression of antigen and antibody in bacterial periplasm as bait and prey proteins [24], can be particularly useful if target antigens are hard to express or unstable in solution. Our new system will offer a method to select antibodies against antigens that need to be expressed in eukaryotes. Other applications of YS2H may include expression of heterodimeric proteins, as demonstrated by similar platforms for expression of heterodimeric mammalian proteins such as major histocompatibility complex II α and β subunits [29] and antibodies in Fab format [30]. The use of our system to quantify and discover protein-protein interactions is not necessarily limited to the study of secretory proteins, because many proteins in nonsecretory cellular compartments or cytosol will maintain native conformations and interactions.

An *in vivo* tool to map protein interactions has generated a large set of protein interactions, particularly among yeast proteins [6]. The readouts from the assays such as yeast two-hybrid and PCA are of cell growth caused by the expression of auxotrophic markers or reconstitution of enzymes and fluorescent proteins and are suitable for determining the presence or absence of protein interactions. In the case of protein network “hubs” in the binary protein interactome, *i.e.* the proteins interacting with a large number protein partners, the information on the strength of pairwise

interactions may provide an important insight into the flow of biological signals orchestrated by the protein hubs. Our newly developed YS2H system is well poised to implement such tasks. For example, in YS2H the hub proteins and known interacting partners are expressed as a pair of the bait and the prey, respectively, and the strength of pairwise interactions can be quantitatively estimated by antibody binding to fusion tags. Additionally, one can discover unknown interaction partners by expressing a library of hypothetical interacting partners in YS2H.

REFERENCES

- [1] Fields S, Song O. A novel genetic system to detect protein-protein interactions Nature. 1989;340:245-6.
- [2] Ghosh I, Hamilton AD, Regan L. Antiparallel leucine zipper-directed protein reassembly: application to the green fluorescent protein. J Am Chem Soc. 2000;122:5658-9.
- [3] Hu CD, Chinenov Y, Kerppola TK. Visualization of interactions among bZIP and Rel family proteins in living cells using bimolecular fluorescence complementation. Mol Cell. 2002;9:789-98.
- [4] Magliery TJ, Wilson CG, Pan W, Mishler D, Ghosh I, Hamilton, AD, Regan L. Detecting protein-protein interactions with a green fluorescent protein fragment reassembly trap: scope and mechanism. J Am Chem Soc. 2005;127:146-57.
- [5] Remy I, Michnick SW. Mapping biochemical networks with protein-fragment complementation assays. Methods Mol Biol. 2004;261:411-26.
- [6] Tarassov K, Messier V, Landry CR, Radinovic S, Molina MMS, Shames I, Malitskaya Y, Vogel J, Bussey H, Michnick SW. An in vivo map of the yeast protein interactome. Science. 2008;320:1465-70.
- [7] Stagljar I, Fields S. Trends Biochem Sci. Analysis of membrane protein interactions using yeast-based technologies. 2002;27:559-63.
- [8] Nyfeler B, Michnick SW, Hauri HP. Capturing protein interactions in the secretory pathway of living cells. Proc Natl Acad Sci USA. 2005;102:6350-5.
- [9] Arnon SS, Schechter R, Inglesby TV, Henderson DA, Bartlett JG, Ascher MS, et al. Botulinum Toxin as a Biological Weapon. J Am Med Assoc. 2001;285:1059-70.

- [10] Jin M, Song G, Carman CV, Kim YS, Astrof NS, Shimaoka M, Wittrup DK, Springer TA. Directed evolution to probe protein allostery and integrin I domains of 200,000-fold higher affinity. *Proc Natl Acad Sci USA*. 2006;103:5758-63.
- [11] Maass DR, Sepulveda J, Pernthaner A, Shoemaker CB. Alpaca (*Lama pacos*) as a convenient source of recombinant camelid heavy chain antibodies (VHHs). *J Immunol Methods*. 2007;324:13-25.
- [12] Gietz RD, Schiestl RH. Large-scale high-efficiency yeast transformation using the LiAc/SS carrier DNA/PEG method. *Nat Protoc*. 2007;2:38-41.
- [13] Colby DW, Kellogg BA, Graff CP, Yeung YA, Swers JS, Wittrup KD. Engineering antibody affinity by yeast surface display. *Methods Enzymol*. 2004;388:348-58.
- [14] Boder ET, Wittrup KD. Yeast surface display for screening combinatorial polypeptide libraries. *Nat Biotechnol*. 1997;15:553-7.
- [15] Johnston M, Davis RW. Sequences that regulate the divergent GAL1-GAL10 promoter in *Saccharomyces cerevisiae*. *Mol Cell Biol*. 1984;4:1440-8.
- [16] Egel-Mitani M, Hansen MT, Norris K, Snel L, Fiil NP. Competitive expression of two heterologous genes inserted into one plasmid in *Saccharomyces cerevisiae*. *Gene*. 1988;73:113-20.
- [17] De Crescenzo G, Litowski JR, Hodges RS, O'Connor-McCourt, MD. Real-time monitoring of the interactions of two-stranded de novo designed coiled-coils: effect of chain length on the kinetic and thermodynamic constants of binding. *Biochemistry*. 2003;42:1754-63.
- [18] Shimaoka M, Xiao T, Liu JH, Yang Y, Dong Y, Jun CD, et al. Structures of the alpha L I domain and its complex with ICAM-1 reveal a shape-shifting pathway for integrin regulation. *Cell*. 2003;112:99-111.

- [19] Sanchez-Madrid F, Krensky AM, Ware CF, Robbins E, Strominger JL, Burakoff SJ, Springer TA. Three distinct antigens associated with human T-lymphocyte-mediated cytotoxicity: LFA-1, LFA-2, and LFA-3. *Proc Natl Acad Sci USA*. 1982;79:7489-93.
- [20] Huang L, Shimaoka M, Rondon IJ, Roy I, Chang Q, Po M, et al. Identification and characterization of a human monoclonal antagonistic antibody AL-57 that preferentially binds the high-affinity form of lymphocyte function-associated antigen-1. *J Leukocyte Biol*. 2006;80:905-14.
- [21] Hagihara Y, Kim PS. Toward development of a screen to identify randomly encoded, foldable sequences. *Proc Natl Acad Sci USA*. 2002;99:6619-24.
- [22] Shimaoka M, Kim M, Cohen EH, Yang W, Astrof N, Peer D, Salas A, Ferrand A, Springer TA. AL-57, a ligand-mimetic antibody to integrin LFA-1, reveals chemokine-induced affinity up-regulation in lymphocytes. *Proc Natl Acad Sci USA*. 2006;103:13991-6.
- [23] Hamers-Casterman C, Atarhouch T, Muyldermans S, Robinson G, Hamers C, Songa EB, Bendahman N, Hamers R. Naturally occurring antibodies devoid of light chains. *Nature*. 1993;363:446-8.
- [24] Jeong KJ, Seo MJ, Iverson BL, Georgiou G. APEX 2-hybrid, a quantitative protein-protein interaction assay for antibody discovery and engineering. *Proc Natl Acad Sci USA*. 2007; 104:8247-52.
- [25] Dranginis AM, Rauceo JM, Coronado JE, Lipke PN. A biochemical guide to yeast Adhesins: glycoproteins for social and antisocial occasions. *Microbiol Mol Biol Rev*. 2007;71:282-94.
- [26] Hanes J, Plückthun A. In vitro selection and evolution of functional proteins by using ribosome display. *Proc Natl Acad Sci USA*. 1997;94:4937-42.

- [27] Smith GP. Filamentous fusion phage: novel expression vectors that display cloned antigens on the virion surface. *Science*. 1985;228:1315-7.
- [28] Krebber C, Spada S, Desplancq D, Krebber A, Ge L, Pluckthun A. Selectively-infective phage (SIP): a mechanistic dissection of a novel in vivo selection for protein-ligand interactions. *J Mol Biol*. 1997;268:607-18.
- [29] Boder ET, Bill JR, Nields AW, Marrack PC, Kappler JW. Yeast surface display of a noncovalent MHC class II heterodimer complexed with antigenic peptide. *Biotechnol Bioeng*. 2005;92:485-91.
- [30] van den Beucken T, Pieters H, Steukers M, van der Vaart M, Ladner RC, Hoogenboom, HR, Hufton, SE. Affinity maturation of Fab antibody fragments by fluorescent-activated cell sorting of yeast-displayed libraries. *FEBS Lett*. 2003;546:288-94.
- [31] Jin M, Andricioaei I, Springer TA. Conversion between three conformational states of integrin I domains with a C-terminal pull spring studied with molecular dynamics. *Structure*. 2004;12:2137-47.

APPENDIX B

CELL SURFACE ASSEMBLY OF HIV GP41 SIX HELIX BUNDLES FOR FACILE, QUANTITATIVE MEASUREMENTS OF HETERO-OLIGOMERIC INTERACTIONS

Submitted to *Journal of the American Chemical Society*⁵

B.1 Abstract

Helix-helix interactions are fundamental to many biological signals and systems, found in homo- or hetero-multimerization of signaling molecules as well as in the process of virus entry into the host. In HIV, virus-host membrane fusion during infection is mediated by the formation of six helix bundle (6HB) from homotrimers of gp41, from which a number of synthetic peptides have been derived as antagonists of virus entry. Using yeast surface two-hybrid (YS2H) system, a platform designed to detect protein-protein interactions occurring through a secretory pathway, we reconstituted 6HB complex on yeast surface, quantitatively measuring equilibrium and kinetic constants of soluble 6HB and delineating the residues influencing homo-oligomeric and hetero-oligomeric coiled-coil interactions. Hence, we present YS2H as a platform for facile characterization and design of antagonistic peptides for inhibition of HIV and many other enveloped viruses relying on membrane fusion for infection, as well as cellular signaling events triggered by hetero-oligomeric coiled coils.

⁵ This part is modified from the following paper in submission: Hu X, Saha P, Chen X, Kim D, Devarasetty M, Varadarajan R, Jin MM. Cell surface assembly of HIV gp41 six helix bundles for facile, quantitative measurements of hetero-oligomeric interactions. Xiaoyue Chen analyzed the data and wrote the paper with regard to Figure B.2 & B.3, Table B.1.

B.2 Research summary

Many proteins naturally fold into varying degrees of helix bundles, indispensable to normal physiology and the onset of diseased states [1]. Of the well-known examples are viral membrane fusion proteins like influenza virus hemagglutinin (HA) and HIV-1 envelope glycoprotein gp41. HIV infection critically depends on the attachment and fusion to host cells through gp120/gp41 complex. The extracellular domain of gp41 consists of a fusion peptide, an N-terminal heptad repeat (NHR), a loop region, a C-terminal heptad repeat (CHR), and a membrane-proximal external region (MPER) (Figure B.1a). Binding of gp120 to CD4 and subsequent interaction with co-receptors (CCR5 or CXCR4) leads to dissociation of gp120 from gp41 and insertion of the viral gp41 fusion peptide into the target cell membrane, which then forms a prehairpin intermediate. Fusion of viral and cellular membrane is provided by the formation of a gp41 six helix bundle (6HB), a conformation described by three CHR packing in an antiparallel manner to a central three-stranded NHR coiled coil [2-3] (Figure B.1b-c). gp41 prehairpin intermediate is transiently accessible to viral fusion inhibitors derived from NHR or CHR, named as N or C peptide accordingly [2, 4-8] (Figure B.1c-d). T20 is one of the early C peptides developed for HIV fusion inhibition [9-10]. CP32M, a rationally designed C peptide, extends to the upstream region of CHR compared to T20, and contains mutations to enhance affinity to NHR. These resulted in higher thermostability and greater inhibition of viral infection against diverse HIV strains [11]. Compared with the inhibitors derived from the C peptides, there are fewer based on the N peptides due to their low solubility. 5-

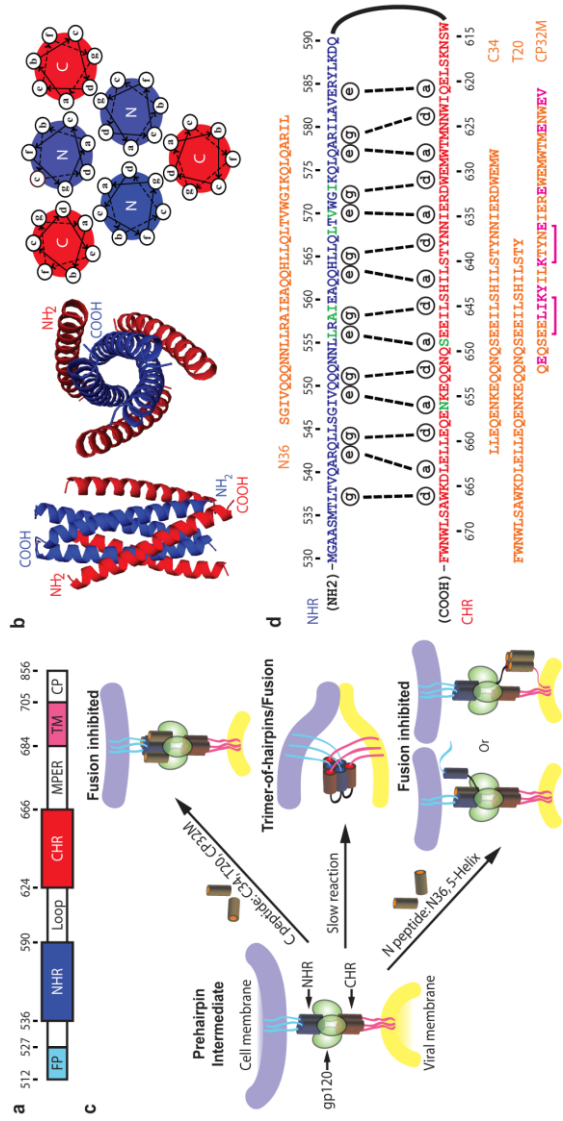


Figure B.1: (a) Schematic view of gp41 elements. Residue numbers at boundaries of each element are shown. (b) Ribbon drawings of side and top views of 6HB are shown (PDB ID: 1AIK [3]). N- and C-termini of helices are labeled. Helical wheel diagram is shown on the right, viewed from C-terminal end of NHR. (c) Depicted are the events of HIV-1 membrane fusion and the mechanism of fusion inhibition by soluble N- or C- peptides. (d) Segments of NHR and CHR of gp41 are shown. ‘a’-peptides (orange) as well as single point mutations (green) used in this study are indicated. CP32M contains rationally designed mutations, shown in pink, some of which were made to introduce intramolecular salt bridges, shown in pink square brackets. FP = fusion peptide; NHR = N-terminal heptad repeat; CHR = C-terminal heptad repeat; MPER = membrane-proximal external region; TM = transmembrane domain; CP = cytoplasmic domain.

Helix (5H) peptide generated by linking 6HB peptides in tandem without the last C peptides is used to mimic N peptide, and is shown to be highly stable and potent in viral inhibition [12]. Other N-peptide derivatives have been based on fusion to synthetic trimerization sequences [13]. While much of the interest has been on developing synthetic inhibition peptides, natural peptides circulating in the blood have been reported to possess a capacity to inhibit virus fusion [14].

Developing biochemical assays to examine the potency of inhibitors of 6HB formation have been hampered by low solubility of N- and C-peptides and their tendency to aggregation [15]. As a facile and quantitative platform to study 6HB formation and to aid in the design of antagonistic peptides, we used yeast surface two hybrid (YS2H) system and expressed gp41 N- and C-peptides on yeast cell surface. In YS2H, a system designed to express a pair of proteins for measuring protein-protein interactions [16-17], one protein is fused to yeast agglutinin, thereby displayed on yeast surface as the 'bait', while the other protein is expressed as a soluble form, serving as the 'prey' (Figure B.2a-b). In the presence of interaction, two proteins associate with each other within a secretory pathway, and the prey is captured on cell surface by the bait. The affinity of the interaction between the prey and the bait can be quantitatively estimated from the relative abundance of short tags fused to bait and prey, typically measured by flow cytometry [17]. This system has previously been used to study heterodimeric interactions; however, its applicability to study higher order, complex oligomerizations has not been demonstrated.

In order to reconstitute gp41 6HB complex on yeast surface, we expressed N36 and C34 [18], a peptide derived from a region in NHR and CHR, respectively (Figure

B.1d & Figure B.2a-c). Surface expression of N36, fused to Aga2 (a subunit of agglutinin) as the ‘bait’, was confirmed by antibody binding to Flag tag appended to the C-terminal of N36. With C34 co-expressed as the ‘prey’, antibody binding to Myc tag indicated that C34 was captured by N36 (denoted as N36/C34 to refer to a pair of Aga2-fused bait and soluble prey; Figure B.2b-c). N36/C34 association was further recognized by 6HB-specific monoclonal antibodies (mAb) NC-1 [19] and D50 [20] (Figure B.2c). Although the major epitope for D50 is at the C-terminal of CHR (Ile642-Lys665) [20], fully included in C34, yeast cells expressing C34 alone (C34/-) were not recognized by D50, indicating that C34 without N36 did not adopt a conformation existing in the context of 6HB. With N36 and C34 swapped for the role of bait and prey (*i.e.*, C34/N36), 6HB was also achieved indicated by the binding of tag-specific antibodies, and mAbs NC-1 and D50 (Figure B.2c). We have chosen to use N peptide as a fusion to Aga2 and C peptide as a soluble form, a configuration more suitable for evaluating the potency of C peptide-based antagonists.

To show that N- and C-peptides were assembled into 6HB conformation previously seen in crystals [3, 21], and to examine if YS2H would provide a quantitative readout to a change in hetero-oligomeric interactions, we have introduced point mutations at various positions and measured the binding of antibodies against reporter tags and 6HB (Figure B.2d). Physical forces contributing to 6HB or coiled-coil conformation in general are from the combination of van der Waals (vdW) or hydrophobic contacts at the helix-helix interface and electrostatic attraction among the residues positioned outside of the interface. In a homotrimeric coil of NHR, amino acids in the position of ‘a’ and ‘d’ in a helical wheel or heptad repeat form a helix-

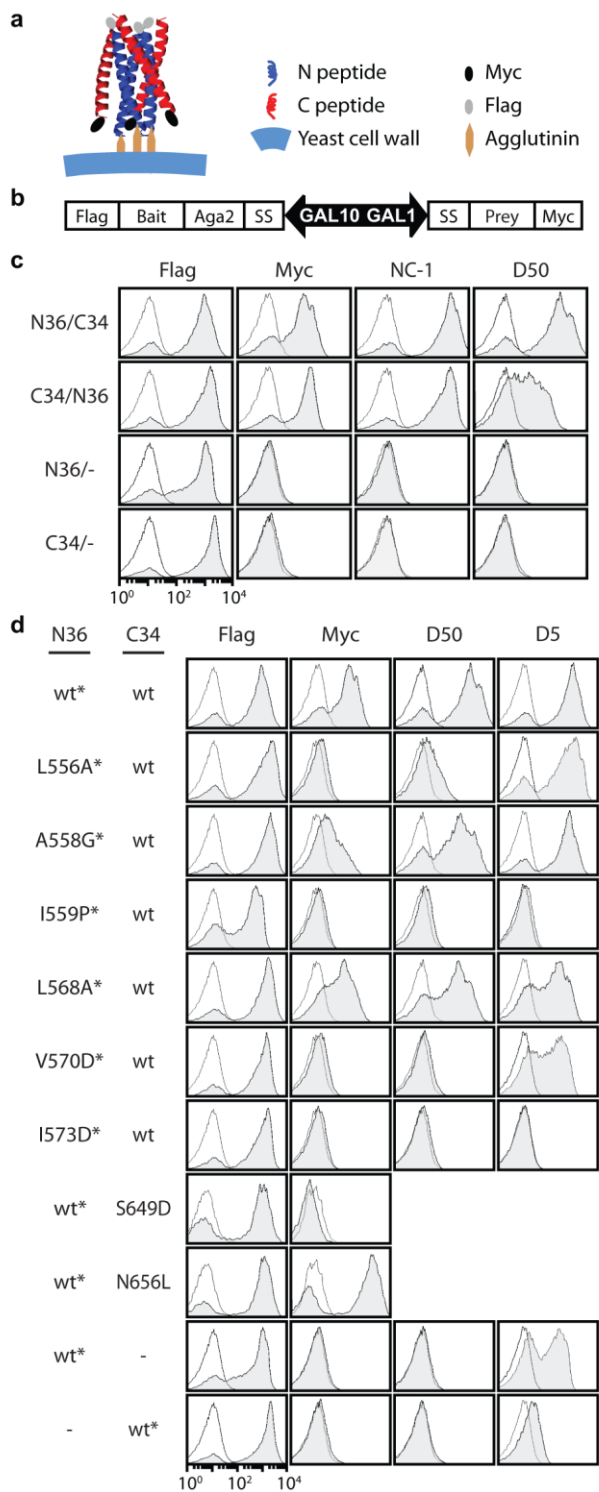


Figure B.2: Assembly of 6HB on yeast surface. (a) A schematic view of 6HB displayed on yeast surface by YS2H is depicted. (b) In YS2H, bidirectional promoter Gal1/Gal10 drives the expression of surface-anchored ‘bait’ as a fusion to Aga2 and secretory ‘prey’, the level of which is measured by antibody binding to short epitope tag, Flag and Myc, fused to bait and prey, respectively. SS = signal sequence. (c&d) Immunofluorescence flow cytometry histograms of antibody binding to Flag and Myc tags and 6HB-specific antibodies (D50, D5). White and grey filled curves are histograms of uninduced and induced yeast cells, respectively. ‘*’ denotes Aga2-fused bait; ‘-’ denotes no peptide; wt: wild type.

helix interface at the core (Figure B.1b). The residues at 'e' and 'g' of NHR would normally be those that promote electrostatic interaction, but instead they are mainly hydrophobic so that CHR packs onto NHR to form 6HB. The mutations that disrupt hydrophobic or electrostatic forces would completely or partially disrupt coiled-coil interactions. Mutations at the interface between NHR and CHR (*e.g.*, L556A (at position 'e'), A558G ('g'), and V570D ('e')) of NHR and S649D ('a') of CHR led to a modest (A558G) to almost complete (L556A, V570D, S649D) loss of C34 association with N36 (Figure B.2d). 5HB-specific mAb D5 [22], which largely recognizes the hydrophobic pocket present at the C-terminal end of NHR, displayed binding to 6HB mutants different from anti-Myc and 6HB-specific antibodies. To cells expressing only N36 (N36/-), D5 showed strong binding (Figure B.2d), revealing that N36 without an assembly with C34 have adopted a conformation seen in the context of 6HB. This is an important result that underscores the utility of yeast display, which circumvents the difficulty with studying isolated N-peptide derivatives in solution because of their hydrophobic, aggregation prone nature. The mutations that disrupted a homotrimeric N peptide conformation (*e.g.*, I559P and I573D at position of 'a' of NHR), therefore, led to a complete loss of both anti-Myc and D5 antibodies (Figure B.2d). L568A, a mutation introduced at position 'c' of NHR, least compromised 6HB formation. In contrast to various mutations that led to partial to complete perturbation of 6HB formation, N656L led to an increase in the level of Myc expression (Figure 2d), attributed to the introduction of hydrophobic residue that would form vdW contact with Ile548 and Val549 (Figure B.1d).

Table B.1: Quantification of the binding kinetics of C peptides to N peptides

N peptide	C peptide	Flag (a.u.)	Myc (a.u.)	D50 (a.u.)	K_D (nM)	A_1	k_{off1} ($10^{-6} s^{-1}$)	A_2	k_{off2} ($10^{-6} s^{-1}$)	k_{on} ($10^3 s^{-1} M^{-1}$)*
N36	T20	100 \pm 3	1 \pm 0	2 \pm 0	433.3 \pm 81.2	NA	NA	NA	NA	NA
N36	C34	111 \pm 15	14 \pm 3	111 \pm 1	10.8 \pm 2.8	13	6 $\times 10^4$	87	56.7 \pm 5.0	5.8 \pm 2.0
N36	CP32M	141 \pm 13	22 \pm 1	0 \pm 0	6.1 \pm 0.6	21	9 $\times 10^4$	79	242.7 \pm 19	40.5 \pm 7.1
NHR	T20	125 \pm 2	13 \pm 1	150 \pm 5	16.6 \pm 1.9	22	8 $\times 10^4$	78	62.7 \pm 9.2	3.9 \pm 1.0
NHR	C34	150 \pm 3	22 \pm 2	134 \pm 4	7.2 \pm 1.1	12	6 $\times 10^4$	88	16.2 \pm 2.2	2.4 \pm 0.7
NHR	CP32M	141 \pm 19	28 \pm 4	0 \pm 0	2.8 \pm 2	16	1 $\times 10^4$	84	20.7 \pm 3.2	16.8 \pm 13.1

Numbers in a.u. are mean fluorescence intensity \pm SE of anti-Flag, anti-Myc, and D50 binding ($n = 3$). N peptide is fused to Aga2 as a bait. a.u.: arbitrary unit; NA: not analyzed; *Computed from k_{off2}/K_D .

After validating the assembly and perturbation of gp41 6HB, we examined the pairing of N36 or full-length NHR (Met530-Gln590) with the variants of C34, such as T20 and CP32M as antagonistic C peptides developed for inhibiting HIV entry (Table B.1). N36/T20 helix-helix interface is formed with three heptad repeats of α helix (Figure B.1d), too short to produce a strong interaction, and this resulted in marginal binding of anti-Myc antibody and D50. In contrast, NHR/T20, spanning longer than four heptad repeats of α helix at the interface, resulted in the level of Myc expression comparable to or less than the levels seen in NHR/C34 and N36/C34. The observation that NHR/T20 led to maximum binding with mAb D50 is consistent with the fact that D50 epitope is at C-terminal end of CHR (Ile642-Lys665), fully included in T20 but is only partially present in C34 [20]. When paired with either N36 or NHR, CP32M, a peptide spanning Gln621 to Gln652 of CHR and containing mutations to enhance electrostatic and hydrophobic interactions with NHR, exhibited elevated levels of Myc expression. The lack of mAb D50 binding to N36/CP32M and NHR/CP32M is due to the epitope for D50 being almost absent in CP32M. In YS2H, the ratio of the levels of reporter tags (Myc & Flag) is directly related by Langmuir equation to equilibrium dissociation constant (K_D) for the interaction between bait and prey, given as $\text{Flag/Myc} = \alpha(1+K_D/[\text{prey}])$, where α is the ratio of Flag/Myc for $K_D \sim 0$. With the estimated values of $\alpha = 4$ and $[\text{prey}] = 10 \text{ nM}$ in YS2H [17], the values of K_D were obtained for NHR or N34 binding to C34, T20, or CP32M (Table B.1). Although direct measurements of solution affinity for these pairs are not available, the difference in affinity is consistent with reported potency of C-peptide based inhibitors in the order of CP32M > C34 > T20 [17]. The ability to quantitatively measure equilibrium

binding constants highlights YS2H as a facile platform for the prediction of the potency of antagonistic peptides.

In addition, YS2H can be adapted for a platform for measuring dissociation kinetics for hetero-oligomeric interactions. To minimize rebinding of dissociated C peptides to N peptides, yeast cells were washed and resuspended in a much larger volume of binding buffer (333-fold dilution of yeast culture) and antibody binding to reporter tags was measured at different time points (Figure B.3). Notably, the decrease in antibody binding to Myc followed a biphasic behavior, characterized by a rapid reduction of Myc within the first 10 min, followed by a slower decrease. An initial rapid dissociation of C peptide may be due to a loss of small percentage (~15%) of C peptides that were associated with the N peptides through non-ideal 6HB conformation. When a two phase dissociation model ($Y = A_1 \times \exp(-t/T_1) + A_2 \times \exp(-t/T_2)$) was used to fit the data, in agreement with the overall trend of dissociation, the slower kinetics were dominant ($A_1 \approx 15$ and $A_2 \approx 85$) for all interaction pairs measured (Table B.1). Following a similar trend with equilibrium affinities, a dissociation rate of C34 from NHR (NHR/C34; $16.2 \times 10^{-6} \text{s}^{-1}$) was 3.5-fold slower than that from N36 (N36/C34; $56.7 \times 10^{-6} \text{s}^{-1}$), and a dissociation rate of NHR/C34 was 3.9-fold slower than that of NHR/T20 ($62.7 \times 10^{-6} \text{s}^{-1}$). Notably, although CP32M exhibited equilibrium affinity to N36 higher than C34 or T20, a dissociation rate of CP32M from N36 ($242.7 \times 10^{-6} \text{s}^{-1}$) was 4.3-fold faster than that of C34 ($56.7 \times 10^{-6} \text{s}^{-1}$) (Table B.1), indicating that CP32M binding to N36 is comparatively dominated by its on-rate. However, the on-rate of CP32M was less apparent with NHR, presumably due to the fact that the mutations introduced in CP32M were those to enhance electrostatic

attraction with the residues belonging to N36, which may be counteracted by the residues outside of N36.

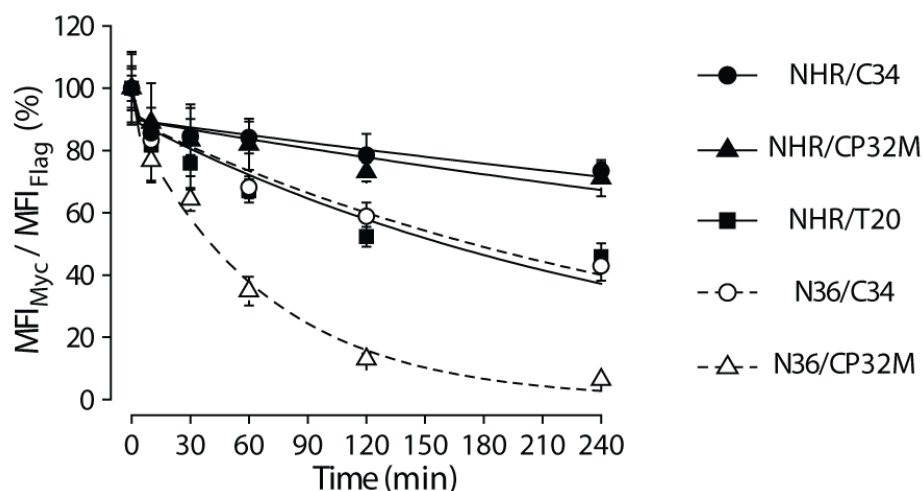


Figure B.3: Dissociation kinetics of C peptide inhibitors measured in YS2H. The loss of antibody binding to Myc (MFI_{Myc}) is plotted as a percentage after normalization to the level of antibody binding to Flag (MFI_{Flag}) ($n = 5$). A two phase kinetic model was used to fit the data, shown in solid or dotted lines.

In summary, we demonstrated a construction of a pair of α helices into YS2H system, and the assembly of viral 6HB structure on yeast cell surface. The equilibrium binding strength between coiled coils within the bundle as well as the kinetics of soluble peptides could be directly and quantitatively characterized. Subtle alterations that resulted from single point mutations perturbing homo-trimeric as well as hetero-oligomeric coiled coils could also be detected in YS2H, which would greatly contribute as a platform to design, optimization, and evaluation of antagonistic peptides as drug candidates. Besides HIV, many enveloped viruses including influenza, respiratory syncytial virus, and Ebola virus require helix bundles for

membrane fusion during virus entry into the host [23]. In the past, great effort has been made on de novo synthesis of various types of helix bundles [24-28]. The assembly of helix bundles or hetero-oligomeric peptides on yeast surface would allow rapid screening and design of candidate inhibitors, without the impediment from often unreliable in vitro protein refolding and costly chemical synthesis.

B.3 Materials and methods

B.3.1 Generation of YS2H constructs

DNA encoding HIV-1 gp41 wild type N and C peptides were chemically synthesized. They were PCR amplified for adding the sequences homologous (~90 bp) to pCTCON at both ends. pCTCON vector was linearized by restriction digestion using NcoI/SalI for introduction of ‘bait’ and BamHI/SpeI for introduction of ‘prey’. Wild type N- and C-peptide cDNAs were then successively introduced into pCTCON through homologous recombination [29], achieved by co-transformation of *E.coli* HME68 [29] with cDNA fragments and linearized pCTCON vector. Plasmids were purified from *E.coli* and sequence-verified. The 6HB destabilizing mutants were introduced by amplifying the ‘bait’ and ‘prey’ fragments along with ~90bp homology to the pCTCON vector using overlap PCR [30], followed by homologous recombination with linearized pCTCON vector.

B.3.2 Growth of yeast cells with protein displayed on surface

YS2H plasmids were transformed into EBY100 yeast cells by Frozen E-Z transformation kit (Zymoresearch, CA). Transformed colonies were inoculated into SDCAA media (20 g/l dextrose, 6.7 g/l Difco yeast nitrogen base, 5 g/l Bacto

casamino acids, 5.4 g/l Na₂HPO₄ and 8.56 g/l NaH₂PO₄ H₂O) and cultured at 30 °C with shaking. After 24 hours of culture in SDCAA, EBY100 cells were transferred to SGCAA media (20 g/l galactose, 6.7 g/l Difco yeast nitrogen base, 5 g/l Bacto casamino acids, 5.4 g/l Na₂HPO₄, 8.56 g/l NaH₂PO₄ H₂O) and cultured for another 24 hours at 30 °C with shaking to induce protein expression.

B.3.3 Immunofluorescence flow cytometry

Monoclonal antibodies used in this study include anti-Myc antibody 9E10 (ATCC), anti-Flag antibody (Genscript, NJ), and phycoerythrin-labeled goat polyclonal anti-murine antibody (Santa Cruz Biotechnology, CA). HIV-1 antibodies NC-1 and D50 were obtained from NIH AIDS Research & Reference Reagent Program. Antibody D5 was a kind gift from Merck Research Laboratories. After induction, yeast cells were harvested, washed in 100 µl of labeling buffer (PBS containing 0.5% BSA with 1 mM MgCl₂), and then incubated with primary antibodies in 50 µl of the labeling buffer for 20 min while shaking at 30 °C. Cells were washed and incubated with secondary antibodies at 5 µg/ml in 50 µl of the labeling buffer for 20 min at 4°C. At the final step, cells were washed once in 100 µl, suspended in 100 µl of the labeling buffer, and subjected to flow cytometry (Epics XL flow cytometer, Beckman Coulter, CA).

B.3.4 Measurement of 6HB kinetics on yeast surface

To measure the dissociation rate of C peptides, each of 3 µl induced yeast cells was briefly washed, incubated in 1 ml washing buffer (PBS containing 0.5% BSA with 1 mM MgCl₂) and rotated at room temperature. Samples were spun down at different time points and the cell pellets were stored on ice until all samples were harvested. For

samples incubated over 1 hour, washing buffer was changed once at 1 hour time point. All the cells were labeled using anti-Myc antibody and then phycoerythrin-labeled goat anti mouse antibody at the same time after all samples were collected. In order to calculate k_{off} , dissociation curves were fitted using OriginPro 7.5 (OriginLab) by two-phase exponential decay.

REFERENCES

- [1] Apostolovic B, Danial M, Klok HA. Coiled coils: attractive protein folding motifs for the fabrication of self-assembled, responsive and bioactive materials. *Chem Soc Rev.* 2010;39:3541-75.
- [2] Weissenhorn W, Dessen A, Harrison SC, Skehel JJ, Wiley DC. Atomic structure of the ectodomain from HIV-1 gp41. *Nature.* 1997;387:426-30.
- [3] Chan DC, Fass D, Berger JM, Kim PS. Core structure of gp41 from the HIV envelope glycoprotein. *Cell.* 1997;89:263-73.
- [4] Chan DC, Kim PS. HIV entry and its inhibition. *Cell.* 1998;93:681-4.
- [5] Jiang S, Lin K, Strick N, Neurath AR. HIV-1 inhibition by a peptide. *Nature.* 1993;365:113.
- [6] Lu M, Blacklow SC, Kim PS. A trimeric structural domain of the HIV-1 transmembrane glycoprotein. *Nat Struct Biol.* 1995;2:1075-82.
- [7] Pan C, Liu S, Jiang S. HIV-1 gp41 fusion intermediate: a target for HIV therapeutics. *J Formos Med Assoc.* 2010;109:94-105.
- [8] Root MJ, Hamer DH. Targeting therapeutics to an exposed and conserved binding element of the HIV-1 fusion protein. *Proc Natl Acad Sci U S A.* 2003;100:5016-21.
- [9] Lalezari JP, Eron JJ, Carlson M, Cohen C, DeJesus E, Arduino RC, et al. A phase II clinical study of the long-term safety and antiviral activity of enfuvirtide-based antiretroviral therapy. *AIDS.* 2003;17:691-8.
- [10] Greenberg ML, Cammack N. Resistance to enfuvirtide, the first HIV fusion inhibitor. *J Antimicrob Chemother.* 2004;54:333-40.
- [11] He Y, Cheng J, Lu H, Li J, Hu J, Qi Z, et al. Potent HIV fusion inhibitors against Enfuvirtide-resistant HIV-1 strains. *Proc Natl Acad Sci U S A.* 2008;105:16332-7.

- [12] Root MJ, Kay MS, Kim PS. Protein design of an HIV-1 entry inhibitor. *Science*. 2001;291:884-8.
- [13] Bianchi E, Finotto M, Ingallinella P, Hrin R, Carella AV, Hou XS, et al. Covalent stabilization of coiled coils of the HIV gp41 N region yields extremely potent and broad inhibitors of viral infection. *Proc Natl Acad Sci U S A*. 2005;102:12903-8.
- [14] Munch J, Standker L, Adermann K, Schulz A, Schindler M, Chinnadurai R, et al. Discovery and optimization of a natural HIV-1 entry inhibitor targeting the gp41 fusion peptide. *Cell*. 2007;129:263-75.
- [15] Gordon LM, Waring AJ, Curtain CC, Kirkpatrick A, Leung C, Faull K, et al. Antivirals that target the amino-terminal domain of HIV type 1 glycoprotein 41. *AIDS Res Hum Retroviruses*. 1995;11:677-86.
- [16] Hu X, Kang S, Lefort C, Kim M, Jin MM. Combinatorial libraries against libraries for selecting neoepitope activation-specific antibodies. *Proc Natl Acad Sci U S A*. 2010;107:6252-7.
- [17] Hu X, Kang S, Chen X, Shoemaker CB, Jin MM. Yeast surface two-hybrid for quantitative in vivo detection of protein-protein interactions via the secretory pathway. *J Biol Chem*. 2009;284:16369-76.
- [18] Lu M, Kim PS. A trimeric structural subdomain of the HIV-1 transmembrane glycoprotein. *J Biomol Struct Dyn*. 1997;15:465-71.
- [19] Jiang S, Lin K, Lu M. A conformation-specific monoclonal antibody reacting with fusion-active gp41 from the human immunodeficiency virus type 1 envelope glycoprotein. *J Virol*. 1998;72:10213-7.
- [20] Earl PL, Broder CC, Doms RW, Moss B. Epitope map of human immunodeficiency virus type 1 gp41 derived from 47 monoclonal antibodies produced by immunization with oligomeric envelope protein. *J Virol*. 1997;71:2674-84.

- [21] Chan DC, Chutkowski CT, Kim PS. Evidence that a prominent cavity in the coiled coil of HIV type 1 gp41 is an attractive drug target. *Proc Natl Acad Sci U S A*. 1998;95:15613-7.
- [22] Luftig MA, Mattu M, Di Giovine P, Geleziunas R, Hrin R, Barbato G, et al. Structural basis for HIV-1 neutralization by a gp41 fusion intermediate-directed antibody. *Nat Struct Mol Biol*. 2006;13:740-7.
- [23] Teissier E, Penin F, Pêcheur EI. Targeting Cell Entry of Enveloped Viruses as an Antiviral Strategy. *Molecules*. 2011;16:221-50.
- [24] Ulrich LE, Zhulin IB. Four-helix bundle: a ubiquitous sensory module in prokaryotic signal transduction. *Bioinformatics*. 2005;21 Suppl 3:iii45-8.
- [25] Dolphin GT. A designed branched three-helix bundle protein dimer. *J Am Chem Soc*. 2006;128:7287-90.
- [26] Seo ES, Sherman JC. Analysis of peptide design in four-, five-, and six-helix bundle template assembled synthetic protein molecules. *Biopolymers*. 2007;88:774-9.
- [27] Rosenzweig BA, Hamilton AD. Self-assembly of a four-helix bundle on a DNA quadruplex. *Angew Chem Int Ed Engl*. 2009;48:2749-51.
- [28] Chakraborty S, Kravitz JY, Thulstrup PW, Hemmingsen L, DeGrado WF, Pecoraro VL. Design of a three-helix bundle capable of binding heavy metals in a triscysteine environment. *Angew Chem Int Ed Engl*. 2011;50:2049-53.
- [29] Sawitzke JA, Thomason LC, Costantino N, Bubunenko M, Datta S, Court DL. Recombineering: in vivo genetic engineering in *E. coli*, *S. enterica*, and beyond. *Methods Enzymol*. 2007;421:171-99.
- [30] Ho SN, Hunt HD, Horton RM, Pullen JK, Pease LR. Site-directed mutagenesis by overlap extension using the polymerase chain reaction. *Gene*. 1989;77:51-9.